VIABILITY AND PERFORMANCE OF A MULTI-MEDIUM UNMANNED AERIAL VEHICLE DESIGNED FOR HYDRO DATA ACQUISITION

by

JOAO C. SERAFINI, JR

A thesis submitted to the

School of Graduate Studies

Rutgers, The State University of New Jersey

In partial fulfillment of the requirements

For the degree of

Master of Science

Graduate Program in Mechanical and Aerospace Engineering

Written under the direction of

Professor Franscisco Javier Diez-Garias

And approved by

_____

_____

_____

_____

New Brunswick, New Jersey

May, 2020

ABSTRACT OF THE THESIS

Viability and Performance of a Multi-Medium Unmanned Aerial Vehicle Designed for Hydro Data Acquisition

By JOAO C. SERAFINI, JR

Dissertation Director:
Professor Franscisco Javier Diez-Garias

With the development and rising popularity of unmanned aerial vehicles (UAVs), numerous applications continue to be devised. In a little touched niche, the project at hand sought to address the challenges with present day water quality monitoring procedures by replacing human involvement with the implementation of a remote platform. Specifically, the proposed solution was the use of a multi-medium octo-rotor capable of performing aerial and aquatic missions while retrieving salient hydro data. With said goal, the project offered a comprehensive discussion on the development of the proposed vehicle; its performance and viability. Tests conducted in both controlled pool water and rugged outdoor environments demonstrated key performance characteristics. While fresh water experiments required little concern, high salinity environments required durable waterproofing methods. With revisions, testing proved all electronics and enclosures watertight up to at least 17ft. With regard to vehicle performance, tests showed the vehicle capable of conducting repeatable seamless transitions in as little as 2 seconds. Finally, experiments were conducted evaluating the abilities of the platform to retrieve turbidity, dissolved oxygen, and conductivity data. Turbidity vehicle experiments showed an average measurement difference of only 0.0759 NTU when compared to hand held sensor readings. Dissolved oxygen data retrieved remotely and manually closely corroborated producing measurements by varying only as much as 4.79%

air saturation. Combining multi-plane experiments, three dimensional water constructs were developed. In these experiments, precision uncertainty was as low as +/- 0.053 mg/L and +/- 35.18 micro-Siemens/cm. As a viable water data retrieval platform, experimental applications are being explored. In continued experiments, the multi-rotor platform will conduct water monitoring missions with a Blue Robotics ROV. In an effort to automate and streamline water data acquisition methods, the heterogeneous vehicle pair is projected to operate in conjunction to complete a common task.

Acknowledgements

Foremost, I praise God, the Almighty from Whom all blessings flow. I thank Him for His daily care and the opportunity He has given me to pursue graduate studies. Thanks be to Him for the many individuals He has brought into my life to help me in my studies and challenge me to ultimately do all for His glory.

I would like to express my deep and sincere gratitude for my advisor, Professor Javier Diez-Garias. I am hard pressed to find words to reflect my appreciation for his continued support during my research and for his patience, motivation, enthusiasm, and immense knowledge. I could not have imagined having a more preparative advisor and mentor for my studies as a MS student and for my future in industry.

With gratitude, I thank Professor Dario Pompili and Mehdi Rahmati for their guidance throughout my degree. Their support both guided me academically and grew me as a research student. With the help of Professor Pompili and his generous funding through the National Science Foundation, I was able to complete my studies as a full time graduate assistant.

I also want to thank Professor Edward P. DeMauro for his continual assistance and guidance throughout my studies. His guidance directed me through challenging times of research and the writing of this thesis.

I desire to express my thankfulness for my beautiful wife. No matter the challenges I experienced in my studies, she ever patiently supported and encouraged me. I am assured life as a graduate student was made much easier having my lovely wife by my side. With the birth of our precious baby boy, Micah was a great motivation in the last months leading up to the culmination of this work.

With love, I thank my family for their constant support throughout my studies. My parents, Joao and Marki ceaselessly supported me with love and encouragement. My sweet

siblings, Markie, Harley, Angela, Eslie, Anna, Luke, Katie, Levi, Evelyn, and Madeline ever brought me joy and happiness.

Finally, I want to thank my fellow graduate students, Aristedes Costeas, Andrii Hlyvko, and Jubilee Prasad for their advice and assistance with my work. I especially want to thank Bhavesh Narala for his many hours of researching with me and never tiring of the many questions I asked. Lastly, I would like to thank Paul Ferri for all his advice and sharing his knowledge of graphing and data analysis.

Table of Contents

List of Figures

Chapter 1

Introduction

An eloquent translation of Plato's Republic reads, "Necessity is the mother of invention." Rare is the occasion that one will stumble upon a novel idea without the pre-existence of a need. In accord with this proverb, aerial flight was conceived with the vision of revolutionizing the methods of travel and the art of warfare. Incidentally, aerial flight was first introduced at the turn of the twentieth century; a time of global tensions and looming threats of war. In 1907, rudimentary multi-rotor flight began with the Breguet brothers' 578 kg Gyroplane No. 1 [1].

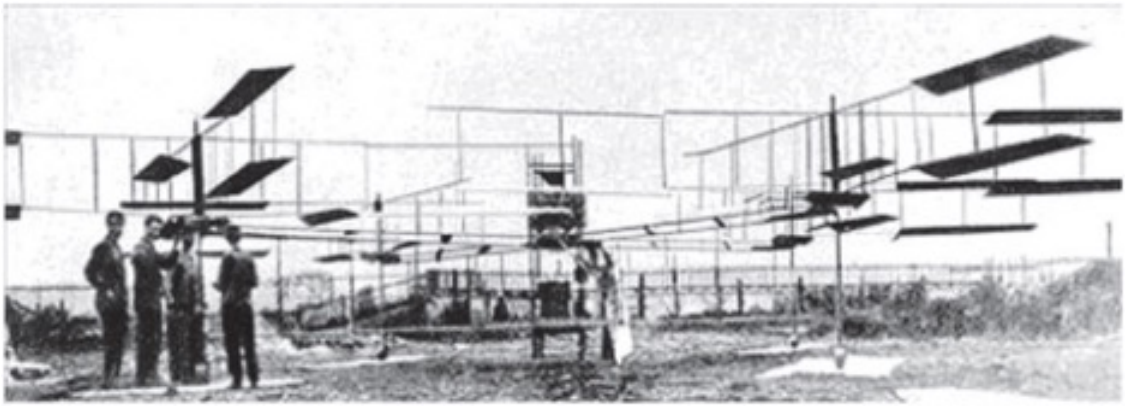

Figure 1.1: Breguet-Richet's Gyro-plane No.1 enabled vertical flight using a multi-rotor setup as early as 1907 [1]

Controlled solely through the skill of an on-board pilot delivering manual inputs, the Brequet's model suffered severe instability. Fast forward to the present, the multi-rotor business has grown to a multi-billion dollar endeavor [2]. Lucrative multi-rotor companies have emerged with state-of-the-art drone technology. Perhaps the most notable, Da-Jiang Innovations (DJI) is a world leader in public consumer multi-rotor products. Their Inspire

2 boasts extreme stability while offering numerous amenities including sense and avoid systems, computer generated cinematographic maneuvers and 4K video acquisition. Since the inception of the aerial multi-rotor, numerous applications for multi-rotors have developed. In a seldom touched niche, the project addressed in this paper relates the design, testing and application of a multi-medium octo-rotor drone for the use of hydro data acquisition. In the following paragraphs, a brief history of aerial flight will be reviewed including the advent and progression of multi-rotor design. In subsequent sections, the theory and basic components of current multi-rotor design will be studied at length.

1.1 Advent and Progression of Multi-Rotor Aerial Flight

On the 17th of December, 1903, true fixed wing aerial flight was achieved by brothers Orville and Wilbur Wright [3]. Although merely a 12 second flight over 120 feet, the Wright's successful flight both encouraged and proved the viability of human flight. Shortly after they reached this milestone, interest in flying machines surged. Within his lifetime, Orville witnessed the development of the jet engine, the helicopter, the bomber and the fighter plane [3]. While the vast majority of study, testing and advances were performed on fixed wing aircraft, inventors realized inevitable drawbacks to planes in certain situations. A plane may be a perfect solution for many aerial applications, however as with many inventions, one may point to the numerous situations where a fixed wing aircraft would fall short of addressing the task at hand. In many scenarios, a need for vertical take off and landing (VTOL) or single point hovering is crucial.

To address these engineering problems, inventors began the journey of creating multi-rotor aircraft for aerial flight. Just 4 years after the Wright's first flight at Kitty Hawk North Carolina, Louis and Jacque Breguet with the help of French scientist Charels Richet, had designed, constructed and tested the first multi-rotor [1]. Although an amazing feat of engineering, it soon became clear that manually flying a multi-rotor aircraft was nearly impossible. Designers realized a multi-rotor operates on the basis of controllable variable thrust from each individual rotor. A human does not have the ability to control each rotor with adequate precision; rendering stable flight impossible to achieve. In the Richet design, a pilot could only control the craft's rotor acceleration as a whole. With such complexities

involving aircraft stability and efficiency, research in multi-rotor design became stagnant until the introduction of novel technologies in the 1990s [1]. During the stagnant decades, improvements to multi-rotor structural design, engine power and multi-rotor mechanics were achieved; but instability remained a deadly flaw. In 1921, Nikola Tesla created design drawings of VTOL capable biplanes. However, his designs were never modeled.

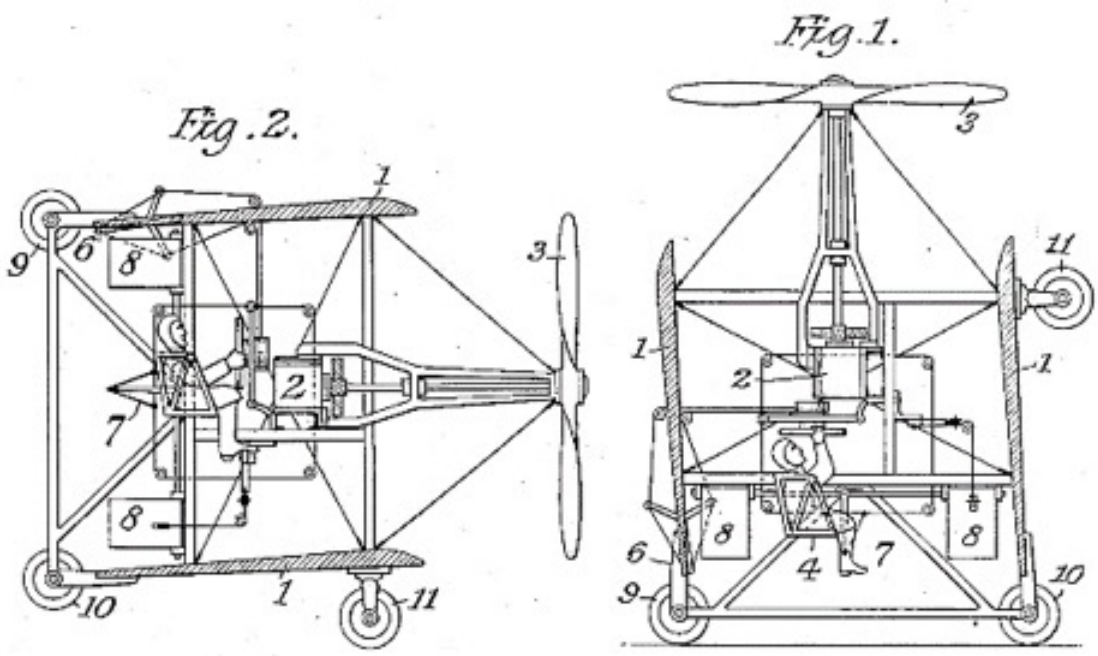

Figure 1.2: Nikola Tesla's 1921 design of a VTOL capable modified biplane [4].

With the rise of the Cold War, renewed interest surged in VTOL aircraft for special missions and for close quarter situations. Combining multi-rotor and fixed wing aircraft designs, engineers developed vehicles capable of VTOL as well as fixed wing horizontal flight. A craft with these abilities would posses great value. While not only achieving the efficiency and speeds of ordinary fixed wing aircraft, a craft of this nature possessed the capabilities of launching and landing without the need for large, flat, open spaces. Hybrid vehicles of this nature provided a middle ground between full fledged unstable multi-rotors and naturally stable fixed wing craft. Although still unstable, take off and landing of hybrid vehicles contributed to only a short portion of flight time. The majority of flight time was in stable horizontal flight. However, it would be a grave understatement to say the design of a hybrid VTOL fixed wing aircraft was a simple task. The United States military

experimented and tested hundreds of designs [5]. Due to the complex requirements of a VTOL fixed wing craft, only the Hawker Siddeley Harrier design emerged as a true success in the Cold War triggered efforts [6]. With the rise of more advanced technologies and computer assisted systems, many different designs have been achieved to date. Models ranged from tilt-rotors and tilt-wings to lift-fans and thrust vectoring engines to tail-sitters and transitioning unmanned aerial vehicles (UAVs).

(a) XV-3

(b) CL-84

Figure 1.3: Both XV-3 tilt-rotor and CL-84 tilt-wing demonstrating VTOL capabilities on aircraft carriers.[9][7]

Tilt-rotor and tilt-wing models such as the XV-15 and CL-84 were designed and tested for their cruise efficiency. By combining lift and engine thrust systems while eliminating rotor drag common on helicopters, tilt-rotor and tilt-wing designs greatly reduced aircraft propulsion weight. However, despite the advantages, these designs posed critical issues with system complexity. Other complications included program risk and weight issues associated with tilting mechanisms [7]. The following figures depict experimental aircraft in real world testing scenarios.

In an attempt to eliminate the drawbacks inherent to tilt-rotor and tilt-wing craft, designers engineered lift-fan and thrust vectoring planes. Early models including the Lockheed XV-4 under-performed and led to fatal crashes [7]. Yet other programs such as the Rockwell XFV-12 were canceled when it was discovered the aircraft could not hover [7]. However, the thrust vectoring X-14 project led to the largely successful production of the high speed Harrier designs. By 1980s, the Harrier AV-8A design boasted a top speed of 635 knots or

(a) XV-5 Vertifan

(b) Hawker-Siddeley

Figure 1.4: Examples of XV-5 Vertifan lift-fan and Hwker-Siddeley thrust vectoring aircraft. [7]

1176 km/hr [7].

One final design attempt during the Cold War era was that of tail-sitters. This design's key features were the elimination of bulky tilting mechanisms and inefficient thrust vectoring systems. With fixed rotors or turbine engines, tail-sitters were situated upright with their

(a) Lockheed XFV-1 "Salmon"

(b) Convair XFY-1 "Pogo"

Figure 1.5: Examples of Lockheed Martin and Convair tail-sitter aircraft. [7]

noses set vertically. Using similar designs, Lockheed experimented with its XFV-1 craft while Convair tested its XFY-1 model. Both aircraft promised success, but low speeds. Due to competing technologies with high speed jets, tail-sitter design testing was canceled [7].

According to Bramlette et al., if research had not halted, it is possible tail-sitter aircraft could potentially have been the fastest propeller driven planes in the world.

With the advent of new technologies introduced in the 1990s, the concept of transitioning UAVs rendered itself viable. New technologies not only reduced the costs of experimental craft by enabling model size reduction, but also revolutionized the safety aspect to experimental testing. Before the introduction of novel instruments, flight testing was performed with large scale models and operated by an on-board pilot. The solution for flight stability among others presented themselves in early 1990 with the inventions of microelectromechanical systems (MEMS), brushless motors, micro-processing systems and efficient battery power systems. Prototypes such as Google's Project wing and Amazon's Prime Air Demonstrator have utilized these current technologies to span the gap between stable VTOL and fixed wing horizontal flight. The arrival of the flight controller and electronic speed controller have enabled stable multi-rotor flight by solving the problem of manipulating each individual rotor independently. The addition and infusion of numerous electronic sensors

(a) Google's Project Wing

(b) Amazon's Prime Air Demonstrator

Figure 1.6: Examples of Googles efficient and Amazon's high speed hybrid quad-rotor UAVs. [7]

have enabled the arrival of smart multi-rotor technology. To date, developers such as Skydio have developed multi-rotors capable of extensive autonomy. As versatile as multi-rotor technology has become, researchers claim they have only yet begun to uncover the vast potential for UAV application and capability.

1.2 Components and Theory of Multi-Rotor Flight Dynamics

The bedrock for modern multi-rotor design and control was laid during the 1990s when various technologies were simultaneously developed. Although designs had been studied and evaluated throughout the past decades, the advent of small electronics and hardware enabled the development of miniature light-weight multi-rotors. The development of on-board micro computers may have been the greatest breakthrough for multi-rotor flight. However, without the development of components such as the small, direct current brushless motor, small UAV operation would not be possible. Basic to the modern multi-rotor are the following components: a flight controller, electronic speed controllers, brushless direct current motors, small aerodynamic rotors and light weight battery power systems. Incorporating each of these components on board the aircraft, a multi-rotor can achieve stable operation. In addition to core multi-rotor components, numerous other components may be added to a system to enhance performance. Many of these extra features are listed in figure 1.7. While multi-rotor mechanical design is simple, electrical design demands greater intricacy.

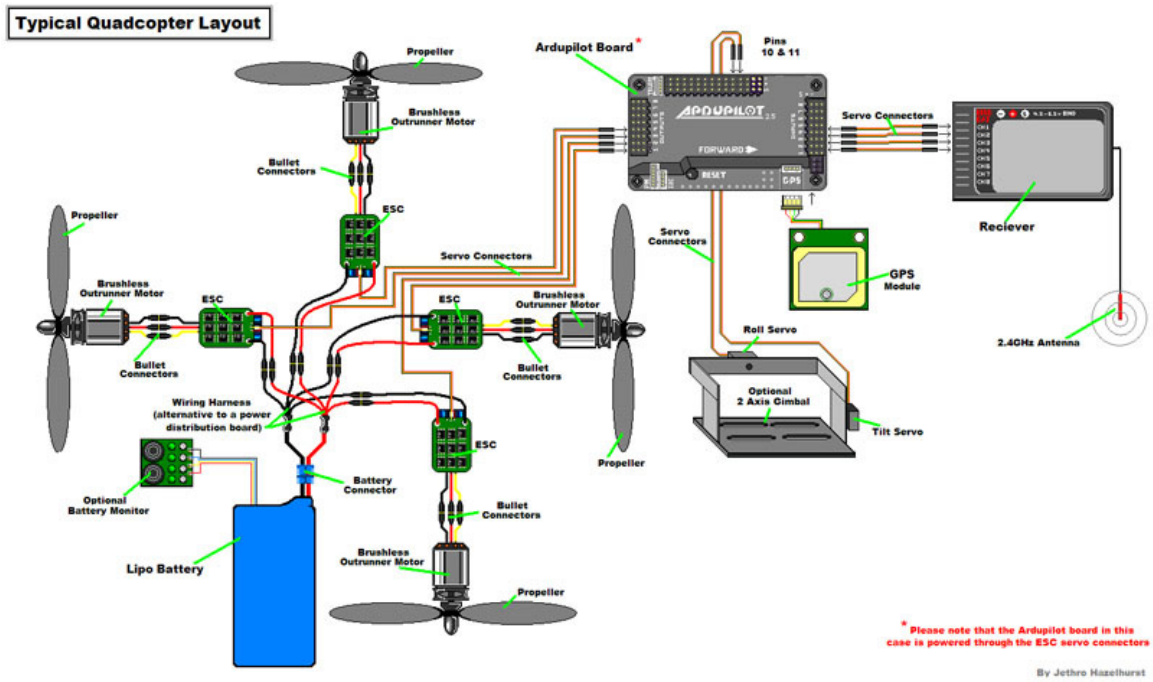

Figure 1.7: Typical multi-rotor system. [8]

As previously discussed, a multi-rotor is controlled solely through the manipulation of its

rotors. Initially, one may surmise the design and operation of a quad-rotor aircraft to be quite simple. After all, hovering flight is simply achieved by the equal thrust of four spinning rotors. If the world were a perfect place, multi-rotor flight would have been a success long ago. However, the world as we know is riddled with error and abundant space for uncertainties; many beyond the power of a human mind to account for. Regardless of how precise the propulsion and rotor design of a quad-rotor, discrepancies will exist. When placed on a vehicle, these small inconsistencies produce large differences in rotor thrust leading to aircraft instability virtually impossible for a human to control.

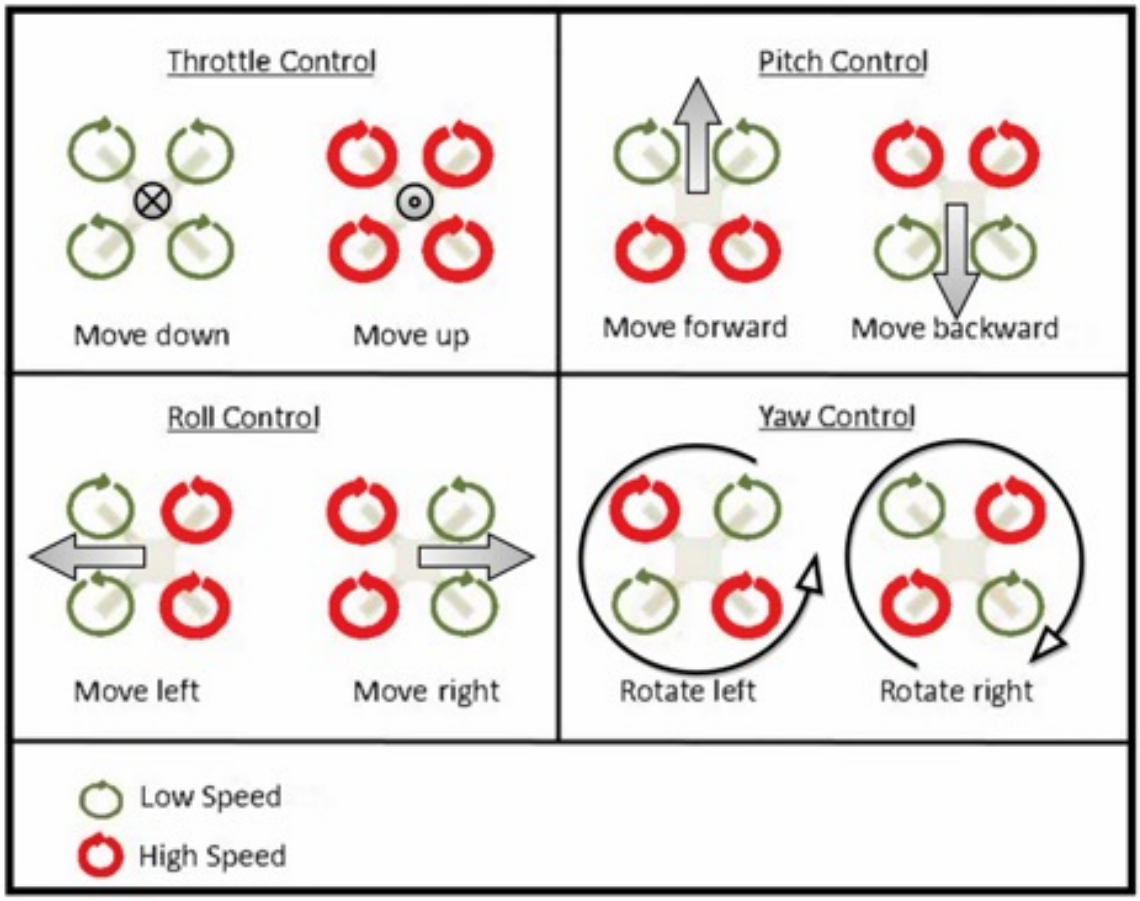

Figure 1.8: Quad-rotor flight dynamics. [5]

To overcome the difficulties of securing stable multi-rotor flight, one must obtain an adequate comprehension of the aircraft's control. A quad-rotor aircraft seen as a physics problem, possesses 6 degrees of freedom (DOF), 3 translational and 3 rotational [10]. However, a quad-rotor has only 4 independent inputs, namely, 4 rotors. Consequently, it is an

under-actuated nonholonomic aircraft and demands complex control algorithms to secure stabilization [11]. To achieve the required 6 DOF, two translational and two rotational motions are coupled. Figure 1.8 depicts the necessary coupling motions for a quad-rotor to achieve position and orientation in space. Beginning with throttle control, one can see how the altitude behavior of a quad-rotor is manipulated. Increasing throttle accelerates all rotors producing greater thrust and thereby lifting the aircraft. Decreasing throttle reduces rotor angular speed and lowers the aircraft. Pitch control is governed by pairing front rotors and rear rotors respectively. To produce forward pitch motion, rear rotors are accelerated while front rotors are kept at a lower or simultaneously decreased speed. The opposite is true for reverse vehicle motion. To achieve left and right bearing, roll control is implemented. Roll movement is performed by the pairing of right and left rotors respectively and following identical logic to that of pitch control. Finally, yaw performance is achieved by pairing diagonal rotors. By manipulating diagonal rotor velocities, torques of varying magnitude are introduced leading to aircraft rotational movement while remaining fixed in space. With the ability to mix any or all of the aforesaid couplings, one may fully control a quad-rotor aircraft. Important to note, precise coordination and dynamic rotor control for throttle, pitch, roll and yaw are only possible with the implementation of the electronic speed controller (ESC) [5]. The ESC functions as a bridge between the flight controller and each motor to interpret electronic signals to precise motor angular speeds. In a subsequent section, the functions of an ESC will be discussed in greater detail.

1.2.1 Flight Controller Development and Basics

Shortly following the emergence of micro-sensors and programmable single board micro-controllers, developers and hobbyists began experimenting with these technologies to produce multi-rotor flight controllers and software. With an ever growing public interest in multi-rotor control, the rise of fully open source flight controller firmware was initiated [5]. In a common effort to perfect the flight controller and steer it toward autonomous capabilities, internet communities and academia joined to create firmware and software programs compatible with both closed and open source programmable micro-controllers. Among the most notable of software are Arducopter, Multiwii and Pixhawk [12]. Along with both

programming firmware and designing custom flight controllers, developers have created interface software capable of directly connecting to compatible boards for firmware upload, sensor calibration, FC customization, etc. Known also as Ground Control Stations, popular interfaces include Qground Control, APM Planner and Mission Planner. Among the most popular flight controllers compatible with these interfaces are the Phenix, OcPoC, Pixhawk, Pixhawk mini, APM, Erle-Brain and PXFmini [12].

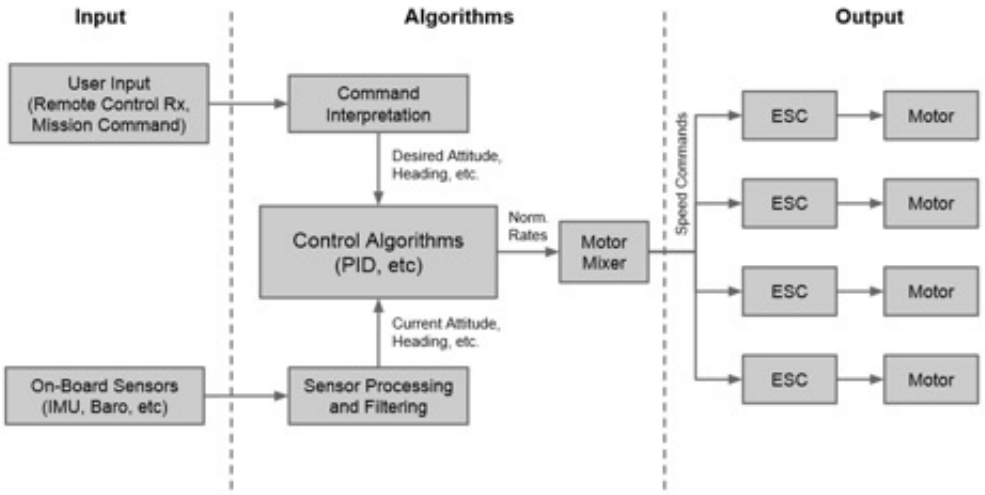

Figure 1.9: Control system process flow. [15]

A flight controller is no simple electronic device. It is the computational powerhouse of a multi-rotor. It processes and coordinates all operations of a multi-rotor system [12]. The key component of a flight controller is the on board Inertial Measurement Unit (IMU), responsible for aircraft tracking and orientation. To complete the task of inertial navigation and maneuver, an IMU uses a combination of accelerometers, gyroscopes and magnetometers. Accelerometers and gyroscopes enable the IMU to accurately estimate an aircraft's attitude (pitch and roll) while magnetometers assist the IMU with measuring vehicle heading (yaw), and determining a vehicles specific force, angular rate and surrounding magnetic fields. On-board barometers allow direct pressure measurement enabling altitude data. Although each sensor listed provides vital data for aircraft stabilization, sensors are prone to drift, and are susceptible to vehicle vibration, environmental interference, slow response time and thermal/temporal degradation [13]. Extensive measures are taken to eliminate

these errors by incorporating sensor redundancy and more importantly, sensor fusion. Sensor fusion records multiple sensor measurements and processes the data through a control law such as the Kalman filter. After adequate compensations are accounted for through the extensive control law algorithm, resulting data allows for accurate vehicle position modeling [14]. Following the diagram depicted in figure 1.9, one can see the basic process utilized by a flight controller to analyze data and consequently produce stabilizing commands. Both sensors and user commands are inputs evaluated by the on board algorithms. Once accurate data has been obtained, electric signals are relayed to the ESCs which, in turn, translate the data into precise physical motor acceleration.

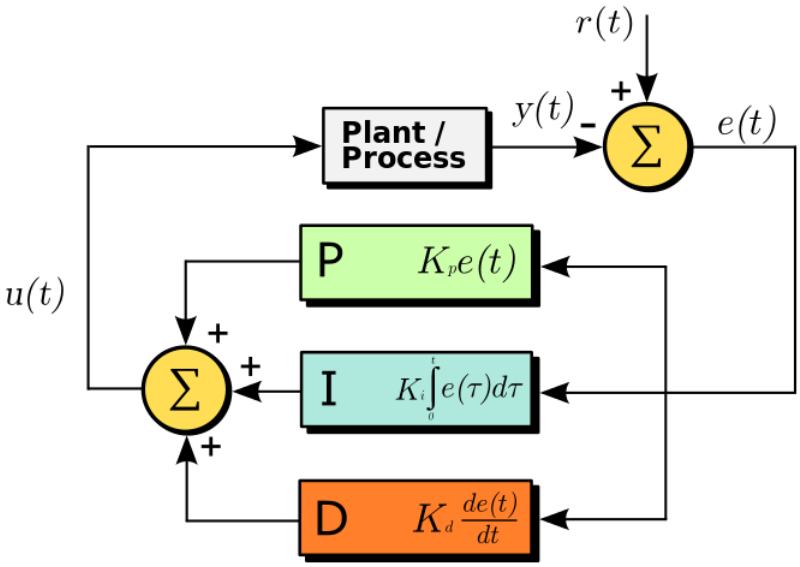

Figure 1.10: Proportional, integral, derivative (PID) control. [16]

Yet another stabilizing system on board a flight controller is the PID (Proportional control, Integral control, Derivative control) loop; figure 1.12. Using attitude data from the filtering process, the PID control algorithm analyzes past and present changes in aircraft attitude and seeks to adapt to future conditions that may affect the aircraft. In figure 1.12, r(t) is considered the input, y(t) is the output and e(t) is the error between input and output. K_p, K_i and K_d are scaling factors which determine the proportions in which each module (P,I,D) add together. Each module is specialized for a specific purpose. Proportional control is designed to stabilize the vehicle when it is exposed to sudden or instantaneous

disturbances. Integral control averages data over a long period of time to ensure smooth damping while stabilizing the vehicle for present and future disturbances. Finally, derivative control is designed to reduce steady state error that can accumulate over time [16]. Failure to properly adjust each of these control modules will lead to either slow or overly actuated vehicle behavior. For example, if the Integral control scaling factor (K_p is set too high, the aircraft will be prone to overshoot when attempting to stabilize. This problem can be seen if an aircraft displays high frequency vibratory motion. When properly tuned, a PID system will ensure resilient vehicle stability with minimal vibrations.

The overview presented should provide the reader with a basic understanding of FC logic. Although the past paragraphs have discussed flight controller key components and their functions, a much deeper understanding would be needed for actual FC programming.

1.2.2 Brushless Motor and ESC Design and Mechanics

Although electric motors have been in existence for over a century, direct current brushless (BLDC) motors were only invented in 1962 by T. G. Wilson and P. H. Trickey [17]. In keeping with the the proverb of necessity driving invention, (BLDC) motors were only invented when the need for reliable, efficient electric motors presented itself with the onset of the Space Race [5]. Data from rocket tests showed that conventional brushed motors were prone to failure when exposed to a vacuum. In many cases, brush wear was compounded rapidly causing motor failure within minutes. To remedy this weakness, engineers developed the brushless motor design which operates using a 3 phase brushless system. To control the torque and rotational speed of a brushless motor, the electic speed controller was developed. The ESC acts as a "smart" bridge between the flight controller and battery to the BLDC. The speed of a brushless motor is governed by the provided voltage. From battery to motor, the ESC precisely regulates the provided voltage based on signals received from the flight controller. In this manner, the angular rate of a BLDC motor is precisely controlled. Although when introduced, BLDC motors were expensive and lacking in power, progress in brushless motor design has produced highly efficient and high torque motors while keeping designs compact.

Via a series of metal-oxide-semiconductor field-effect transistors (MOSFETs) and diodes,

an ESC modulates a 3-phase signal applied to a brushless motor [18]. Generally, ESCs incorporate 6 or more MOSFETs to produce motor commutation steps. Referring to figure 1.11a, one can trace the commutation logic given the phase rotation schedule of figure 1.11b.

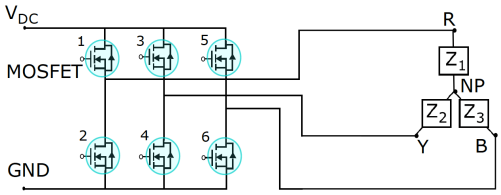

(a) MOSFET inverter system.

MOSFET	Step 1	Step 2	Step 3	Step 4	Step 5	Step 6
1	I	O	O	O	O	I
2	O	O	I	I	O	O
3	O	O	O	I	I	O
4	I	I	O	O	O	O
5	O	I	I	O	O	O
6	O	O	O	O	I	I

(b) Phase rotation schedule

Figure 1.11: 3-Phase commutation schedule of a 6-MOSFET system ESC. [18]

For each commutation step, one transistor provides voltage to the motor, one acts as ground and the third is disconnected. Using this process, a combination of energized electromagnets are used to propel the connected motor. When the six steps in figure 1.11 are repeated at varying frequencies, the angular velocity of the motor will be controlled accordingly. However, if a motor were to commutate blindly, the ESC would lose track of the motor positioning and lead to motor stall and impairment. For this reason the third disconnected transistor in each step sequentially tracks motor positioning via back electromotive force (EMF) sensing. Back EMF is the magnetic field that generates a voltage in the direction opposite to current flow. Using this system for motor commutation, motor speed can be reliably achieved and precisely monitored.

Fundamentally, motors are designed to convert electrical energy to mechanical energy. Although there are various types of motors in production, small brushless motors are most common in multi-rotor vehicles because of their light weight and high efficiency. A common BLDC motor is made up of two main components, a stator and a rotor [18].

The stator is a fixed circular armature, housing electromagnets and central bearings. Since BLDC motors operate on a 3-phase current system, the electromagnets arranged around the stator are categorized in triplets. Each individual electromagnet is referred to as a stator tooth and each triplet is referred to as a stator stack [5]. Regardless of motor size, the number of stator teeth will be a multiple of three. Wound around each stator tooth is an insulated copper wire. When current is provided to the stator, the flow is forced to circulate

around the tooth inducing an electromagnet. Depending on the direction of current flow, the polarity of the electromagnet may be manipulated between north and south.

The rotor is a circular hub that generally circumvents the stator with permanent magnets facing inward. The permanent magnets are arranged in pairs with alternating polarities of north and south around the inner circumference of the rotor. Generally, the rotor is attached to the stator by sliding an axle through the bearings which is fixed to the stator.

To produce rotational motion, a BLDC motor follows a basic set of steps. These steps were alluded to in the paragraph discussing the functions of an ESC. Since each set of magnets is contained on their respective armature (stator and rotor), they will pass each other without touching. However, the force they exert on each other is the means by which they propel the rotor. By coordinating this force interaction, continuous motor commutation is achieved. When an ESC sends signals to spin a motor, numerous electromagnetic pulses with varying polarities are initiated and cycled. To gain a basic understanding on how a

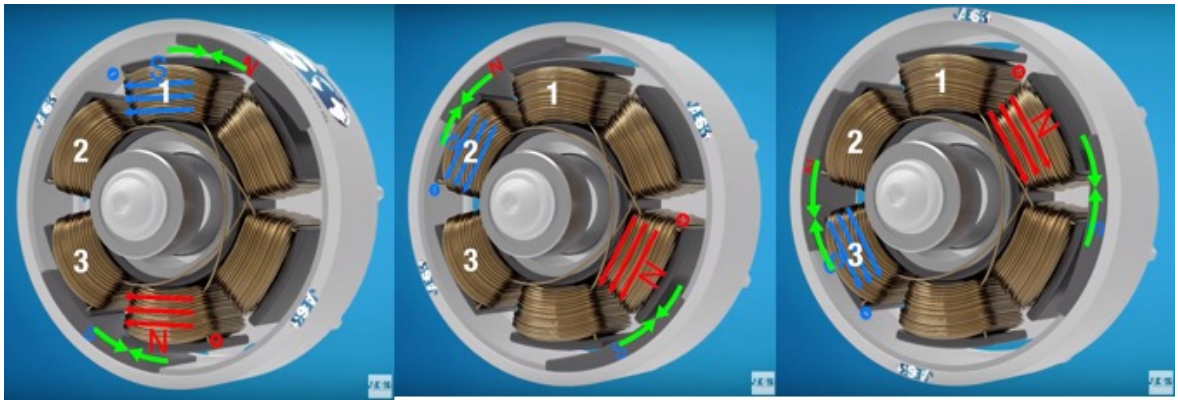

Figure 1.12: Simplified commutation process of a BLDC motor. [19]

BLDC motor commutates, consider the example depicted in figure 1.12. For this scenario, there are two permanent magnets and 6 electromagnetic stator teeth. The motor will continue to commutate by perpetually cycling through a set of specific schedules. When the permanent polar north magnet draws near to stator tooth 1, stator tooth 1 will energize to create a polar south magnet. Simultaneously, the stator tooth directly opposite tooth 1 will produce a polar north electromagnet. Taking advantage of the magnetic forces, the above polarities of tooth one and its opposite will pull the permanent magnets counterclockwise. As soon as the permanent north magnet is reaching its highest point of attraction with

tooth 1, tooth 1 will become neutral. At this point, stator tooth 2 will energize as a polar south magnet to pull the polar north magnet counterclockwise yet again. This motion will continue to propagate though each stator tooth. A complete cycle is said to be accomplished when each stator tooth has cycled from neutral, to polar south, to polar north, to neutral again. In the scenario of figure 1.12, there will be 12 steps for 1 complete rotation of the rotor. In a more realistic motor, there will be many more outer permanent magnets. With more permanent magnets, more electromagnets can be utilized simultaneously. Increasing the number of active magnets directly increases motor torque and rotational smoothness [5]. Based on these physics, one can greatly increase a motor's torque while keeping the size of the motor constant.

1.3 Status and Overview of Robotics for Environmental Monitoring of Water Bodies

Given the present popularity and capability of multi-rotors, it is clear they will be instrumental in revolutionizing traditional methods for numerous processes. The methods of aerial photography and cinematography have greatly changed. Previously, when aerial footage was needed, manned planes or helicopters were hired. Due to the expensive nature of previous processes, aerial footage was not readily available to the general public. With the rise of both open source and commercial multi-rotor platforms, photographers of practically any financial status have numerous venues to access aerial footage. Both military and commercial communities have displayed great interest in multi-rotor potential. Military applications include multi-rotors for search and rescue, surveillance, scouting and explosive mine searching. Commercial venues include multi-rotors for bridge inspections, power line inspections and aerial deliveries. The list of uses for both military and commercial applications is virtually in-exhaustive.

In this project, specific interest in applying multi-rotors for the use of environmental water body monitoring is explored. Currently, water quality monitoring is largely dependent on human labor [20]. To address this issue, research is being conducted in this field of study. Researchers, Francisco Marques et al. in their work, "A Critical Survey On Marsupial

Robotic Teams for Environmental Monitoring of Water Bodies" present both the benefits and challenges of robotic use for water monitoring [20]. In a subsequent study, Marques et al. implement the use of a marsupial robotic team for environmental monitoring [21]. A marsupial team is one in which one robot possesses the ability to carry other robots.

Figure 1.13: Example of a marsupial robotic team composed of an unmanned surface vehicle (USV) and an unmanned aerial vehicle (UAV). [20]

Marques' platform utilized a surface watercraft and an aerial multi-rotor. Working in tandem, the watercraft was optimized for long endurance and close range sampling while the multi-rotor specialized in short missions covering large regions of interest at high altitudes. In this joint endeavor, "the multi-robot team increases the overall robustness by joining the high endurance afforded by water surface robotics systems with the far field perceptual capabilities of aerial vehicles [20]."

However, there are situations in which marsupial robotic teams are not the optimal solution. In another work, researchers present a solution for water quality monitoring using a waterproof multi-rotor [22]. Authors of, "An Open-Source Watertight Unmanned Aerial

Vehicle for Water Quality Monitoring," pose multiple scenarios in which current methods of environmental data collection are impractical and dangerous. When collecting data in locations such as high current rivers or on turbulent coastal waters, procedures can be perilous to both humans and valuable equipment. When testing in areas with numerous small bodies of water, it is greatly cumbersome to continuously transport a watercraft to each point of interest. In addition, when testing on a body of water, one may encounter obstacles (ie, fallen trees, dams, etc.) which pose cumbersome challenges to work with. These challenges could be greatly reduced with the implementation of a waterproof multi-rotor. Authors of [22] demonstrate the implementation of such a multi-rotor. As they relate,

Figure 1.14: Waterproof unmanned aerial vehicle demonstrating aerial flight over water surface. [22]

a multi-rotor of this nature eliminates the need for humans or expensive equipment to access remote or dangerous areas. With the ability to take-off from a lake's surface, their floating multi-rotor possesses the ability to fly over any obstacle laying across its path. Designed as a surface vehicle, their craft samples data continuously while floating on a body of water and only takes flight to avoid obstacles or return to the ground station. In this manner, the endurance of the vehicle is greatly enhanced due to the low energy consumption of water

surface navigation [22]. However, the platform presented by the authors of [22] is limited to surface and aerial navigation only.

For this reason, the goal of the project at hand seeks to address the challenges of using a multi-rotor not only for aerial and surface locomotion, but sub-surface navigation as well. Ultimately, steps were taken to design, fabricate and test a custom multi-rotor, capable of amphibious sub-surface, surface and aerial navigation. In this manner, subsequent tests sought to expedite the collection of salient water data.

Chapter 2

Naviator X8-Rotor Drone

As mentioned before, the task pursued in this project sought to design a small multi-rotor aircraft for the purpose of retrieving salient hydro data. With a vision of using this UAV for future multi-vehicle collaborations, the multi-rotor was developed to be easily customized to the users needs. To gain a broader understanding of the UAV designed in this project, a detailed overview will be conducted on the previous multi-rotor versions that led to the project at hand.

2.1 Naviator Multi-Rotor Concept Development

When analyzing processes in certain industrial fields, it is the job of an engineer to brainstorm and optimize the method in which a task is completed. Quite often, when one is presented with a difficult task, inspiration is gained by studying processes in nature. When one is motivated by nature and desires to mimic a natural process, it is expressed as a bio-inspired innovation. Examples of bio-inspired designs are common in everyday life. The basic designs of many aircraft are directly derived from studies seeking to emulate the aerodynamic flight mechanisms of certain fowl. Such innovations can be seen in the work of David Rival et al. entitled, "The influence of airfoil kinematics on the formation of leading-edge vorticies in bio-inspired flight" [23]. Under the guidance of Professor Javier Diez of Rutgers University, research students developed the bio-inspired, highly maneuverable multi-medium aircraft known as the Naviator. The Naviator is a multi-rotor aircraft possessing 8 rotors configured in a double coaxial manner. In effect, this design could be thought of as two quad-rotors (octo-quadrotor) stacked with an optimal spacing between top and bottom rotors. Intrigued with the abilities of aquatic birds to fly through the air, dive into and swim through water and finally transition to aerial flight once again, the Diez group developed a mechanical system

which sought to mimic this behavior. However, an aquatic bird can only remain underwater for a limited time due to its aerial design. Fish on the other hand are optimally suited for aquatic locomotion. Certain fish posses the ability to glide over water for a short period of time, but soon re-submerge to their natural habitat. Understanding the mechanics and

Figure 2.1: Naviator bio-inspiration. [25]

locomotion necessary for multi-medium maneuverability is crucial. As depicted in figure 2.1, the driving locomotion factors governing birds and fish are listed. The main forces acting on a bird in flight are lift, weight, thrust and drag, while key forces acting on a fish are buoyancy, weight, thrust and drag [24]. Figure 2.1 illustrates a simplified analysis by disregarding drag. By combining the different attributes of both aquatic birds and flying fish, the Naviator multi-rotor is able to achieve efficient aerial flight, aquatic maneuverability and seamless multi-medium transition.

2.2 Naviator Design, Mechanics and Locomotion

The octo-quadcopter (X8) design of the Naviator was not chosen at random. The first Naviator and progressively, the later versions of the Naviator sought to optimize performance in both air and water. To determine optimal performance, extensive testing incorporated proper propeller diameter, motor sizing and adequate battery systems [25]. At length, it

was found that the octo-quadcopter design provided a simple yet effective system for multi-medium locomotion as well as seamless medium transition. When operating in air, the Naviator behaves in accord with common aerial multi-rotor dynamics. However, in water, the Naviator rotates 90 degrees to propel itself in the lateral direction. Core to the design of the Naviator is its biplane coaxial configuration. The most difficult obstacle to overcome in multi-medium flight is the transition period; especially the transition from water to air [26]. Referring to figure 2.2, aircraft transition takes place from left to right. For simplicity, only

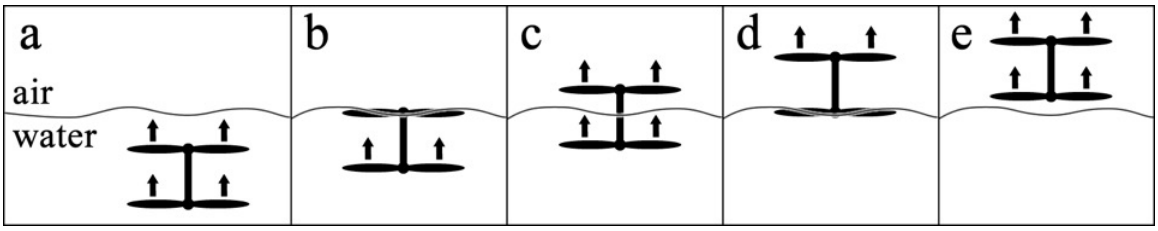

Figure 2.2: Rotor motion for multi-medium transition processes. [26]

one coaxial pair of rotors are depicted. The line crossing each cubicle corresponds to the air-water interface. Beginning with (a), both rotors are rotating at slow RPMs and producing upward motion. It is important to note that the same thrust in a more dense medium (ie. water) can be generated with much lower RPMs as compared to a less dense medium (ie. air). Once the top rotor has reached the air-water interface (b), the top rotor ceases to rotate in order to ensure stability on the unpredictable surface. Once passed the surface (c), the top rotor switches to air mode (high RPMs) while the bottom rotor remains in water mode. When the lower rotor reaches the interface (d), the same logic as step (b) is followed. Finally, once all rotors are in the air (e), full air mode is implemented and normal aerial flight is commenced. With the coaxial configuration and specialized firmware following the above procedure, the Naviator can seamlessly complete a water to air transition within 2 seconds [25].

Another important aspect to the design of the Naviator is the need for dry electronics. In each iteration of the Naviator, changes have been made to optimize buoyancy and water-proofing methods. In an attempt to create a slightly negatively buoyant Naviator V5 and V6, an airtight center-body was 3D printed to house batteries and the flight controller, while acting as the main frame of the vehicle. By utilizing high quality 3D printing technology,

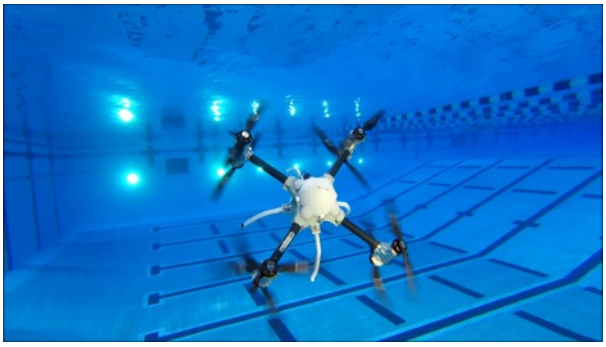

(a) Naviator Version 5.

(b) Naviator Version 6.

Figure 2.3: Image a depicting NV5 conducting autonomous mission and image b showcasing NV6 design. [26]

the complete aircraft body was meticulously customized for its purpose. To dissipate heat generated by the ESCs used on the Naviator V5, airtight aluminum motor mounts were constructed to house the 8 motor controllers. In this method, all electrical components on the aircraft were isolated in an impervious system. Such a system renders the Naviator a rugged aerial vehicle capable of operating in exceedingly harsh environments.

Common to certain applications, aerial missions are performed by aerial vehicles and aquatic missions are conducted with submersible craft. Applications addressing multi-medium procedures require the use of multiple vehicles to accomplish a single task. The Naviator multi-rotor design seeks to address the complications and expenses of multiple vehicle implementation. This is achieved by delivering a single multi-medium vehicle, efficient in both aerial and aquatic environments. From bridge structure inspection to oceanic oil spill evaluation, the list of uses for such a vehicle are numerous indeed [25].

2.3 Naviator Version 7

Building upon the design concepts of the previous Naviator versions, the project at hand sought to customize a Naviator for the purpose of experimental hydro data acquisition. Simultaneously, multiple aspects of the traditional Naviator designs were altered in an attempt to produce a simple, modular, low cost, multi-rotor vehicle. As will be discussed in future sections, the goals for this project were culminated in the complete design and

implementation of the Naviator Version 7.

Although the idea and creation of the Naviator existed before the design of the NV7, it was advantageous to tailor a vehicle to the requirements of this project. Improving on past

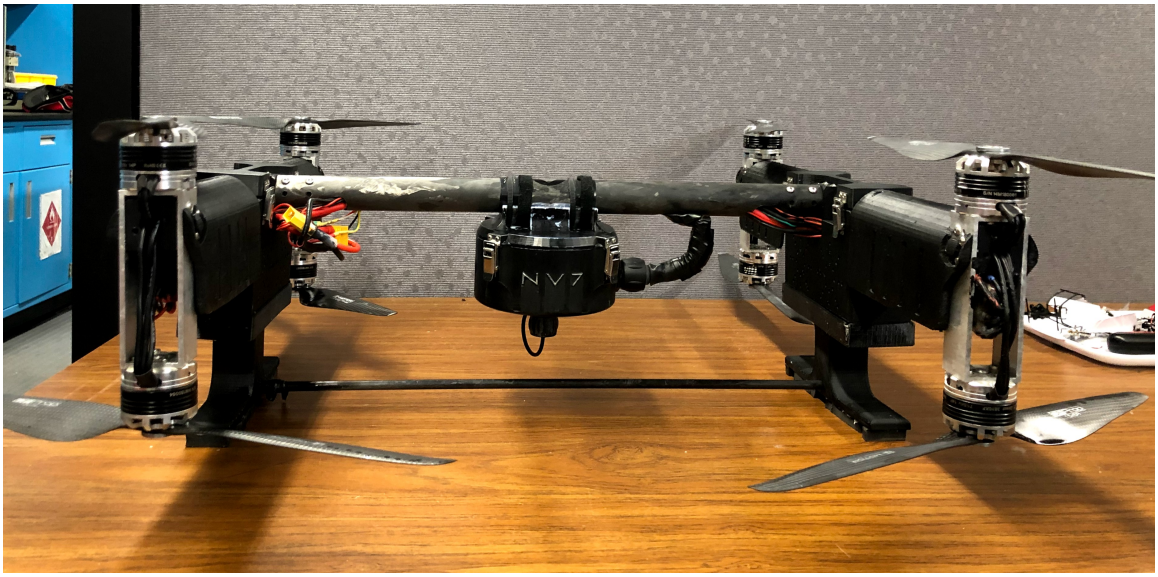

Figure 2.4: Naviator Version 7 in its completed state.

experiences, the NV7 was designed to minimize cost, fabrication time and maintenance while increasing its capabilities. The previous Naviator's precision resin, 3D printed bodies were expensive. If there were any mistakes during post processing, the entire body would need to be reprinted. However, the NV7's body is made from commercially available parts for a fraction of the price. The lower cost of this multi-rotor allows for the production of many vehicles for the purpose of swarming, or having many multi-rotors flying simultaneously. There would be no need for post-processing and the parts would be easy to replace if they were to be damaged. Every component was replaceable without needing to disassemble large portions of the multi-rotor. The previous versions of the Naviator depended on a waterproof enclosure, limiting their space for payloads or equipment attachments. Because of the extra space provided by the H-configuration, the NV7 allowed for a wide range of uses and payloads. With ample mounting room, a user could attach multiple instruments at a time. Due to its rigid carbon fiber chassis, the attached payload was guaranteed to remain fixed in place. With its 3D printed battery compartments and modular assembly, the NV7 was easily scalable to fit the specifications of the project at hand.

Since its design and fabrication, the NV7 was tested extensively in both air and water operations. Systematic operations were conducted in both controlled pool areas and the ocean. When experimenting in the Tampa bay, the NV7 performed exceptionally well. Multiple tests were conducted in which the multi-rotor was subjected to performing 20 water to air transitions consecutively. The NV7 successfully completed each goal.

The NV7 was primarily designed as an experimental vehicle expected to transport scientific water instrumentation. In the immediate scope, the NV7 transported turbidity and dissolved oxygen sensors. Equipped with these instruments, the NV7 conducted pre-defined

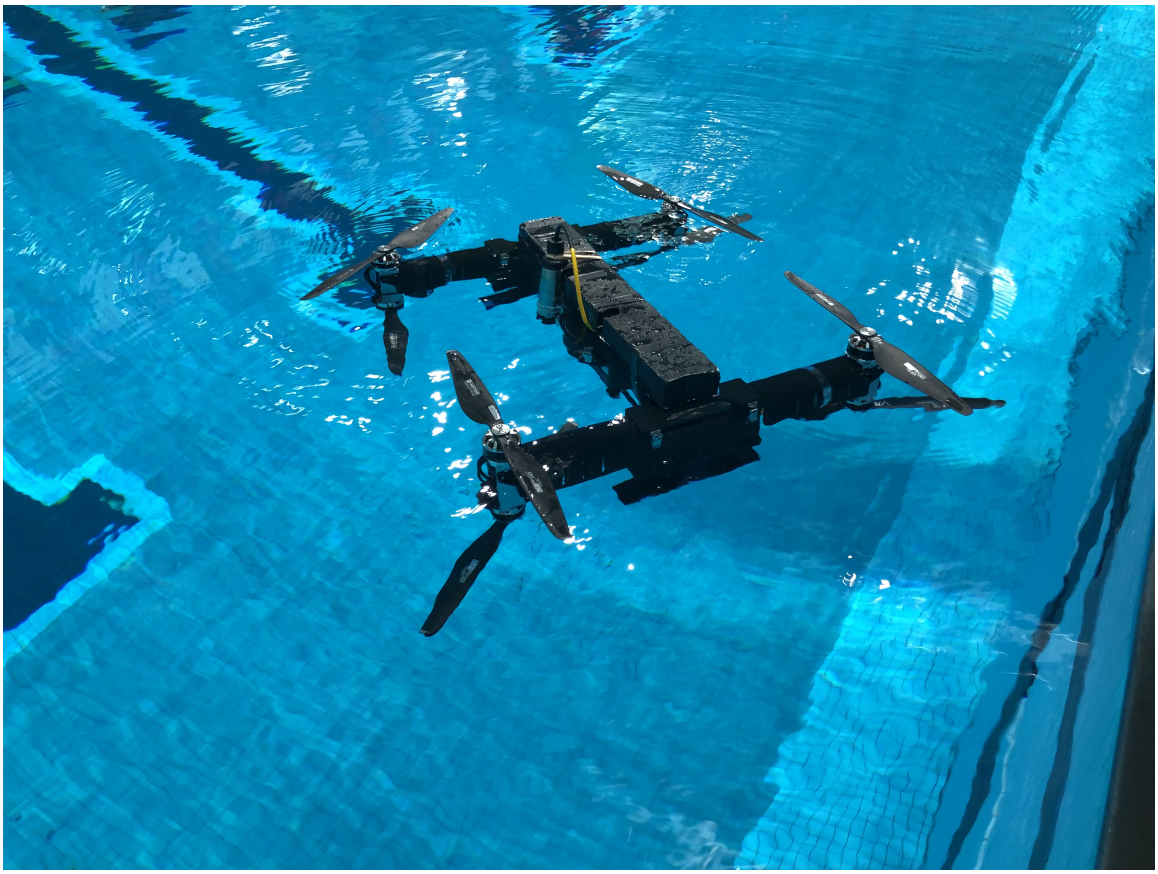

Figure 2.5: Depiction of NV7 conducting mission and gathering turbidity data.

missions in which it collected data samples from multiple pre-allocated points of interest, hovering over the water or submerging at each location. Conventionally, water monitoring is conducted by collecting water samples for laboratory analysis, single point in time measurements with probes, or logging at regular intervals over longer periods of time. However, these methods are susceptible to biases. In collecting water samples, error is introduced if

the sample inaccurately represents the chemical construct of the entire area of interest. Collecting single point or regular interval measurements in one location also poses the problem of non-representative measurements. Although these discrepancies may be reduced, tedious methods would need to be undertaken to analyze large areas of interest. The ability of the NV7 to quickly perform missions and retrieve water data, allows users to dramatically cut back on time spent manually scanning and collecting data over an entire area of suspected interest. Utilizing this method of data collection and streaming allows for real time data analysis and spatio-temporal measurements from a predefined area of interest. Obtaining data from multiple locations with the NV7 reduces the possibility of irrepresentative data while greatly minimizing the labor and time needed when compared to conventional methods.

Chapter 3

Naviator Version 7 Design and Fabrication

In the following sections, the research and methods performed to design and construct the Naviator Version 7 will be described in detail. Beginning with the reasoning for choosing the experimental multi-rotor design, sections will follow describing the modularity of the vehicle as well as the power-system development.

3.1 Configuration Design process

Before finalizing the multi-rotor design for this project, specific task requirements and objectives were realized and listed. The goal of the multi-rotor was to act as a formidable, easy to use platform for the acquisition of water data. In its final form, the Naviator V7 was seen as a "plug-and-play" tool that one could simply throw in the water and begin the process of testing. To successfully perform, the vehicle for the task at hand would need to meet certain criteria. Firstly, the multi-rotor design would need to be durable. When used in real-life scenarios, the NV7 would be exposed to multiple flights encountering obstacles, hard landings and potentially crashes. While no vehicle is completely destruction proof, the NV7 was constructed of highly resilient materials. Banking on the high likelihood of crashes, the NV7 was designed to be modular. If any part of the vehicle were damaged, the multi-rotor's design was such that each part could be replaced with minimal copter disassembly. While doubling as an essential means of water-to-air transition, the octo-rotor configuration of the model enabled extra safety redundancy measures. Using the octo configuration, safe aerial flight could still be possible if up to four motors were impaired. Secondly, the Naviator V7 design needed to be simple and inexpensive to manufacture. As opposed to previous expensive Naviator models, the Naviator V7 was designed to be assembled and disassembled in a matter of minutes with the majority of components available on the commercial market.

Thirdly, vital to any multi-rotor is the need for indefinite flight. Since multi-rotors are notorious for limited flight endurance, the need for easy battery replacements was paramount. For this reason, the battery system incorporated on the NV7 was designed to be replaceable without the need of any tools. Finally, the copter was designed to carry hydro-logic sensory equipment. To accommodate these demands, the NV7 needed to provide ample storage capacity for supplementary modules while remaining as compact and lightweight as possible. To develop a vehicle capable of meeting these needs, detailed SolidWork CAD renderings were produced. Drawing all components to scale and assigning specific densities for each component, key insights such as buoyancy and vehicle weight were derived with accuracy. After extensive analysis, it was found that designing a copter with a slender body while maintaining sufficient surface area for the attachment of supplementary sensors was necessary. To best accommodate these needs, it was found that an H-configuration possessing a weight of 6 kg posed the optimal solution.

3.1.1 Naviator V7 Main-Frame

Designed to be light weight, rigid and durable, the Naviator Version 7 main-frame was constructed using 2mm walled carbon fiber tubing and anodized aluminum mounts. Desiring to construct a simple yet durable body for the NV7, a simple H-configuration shape required only 3 carbon fiber tubes.

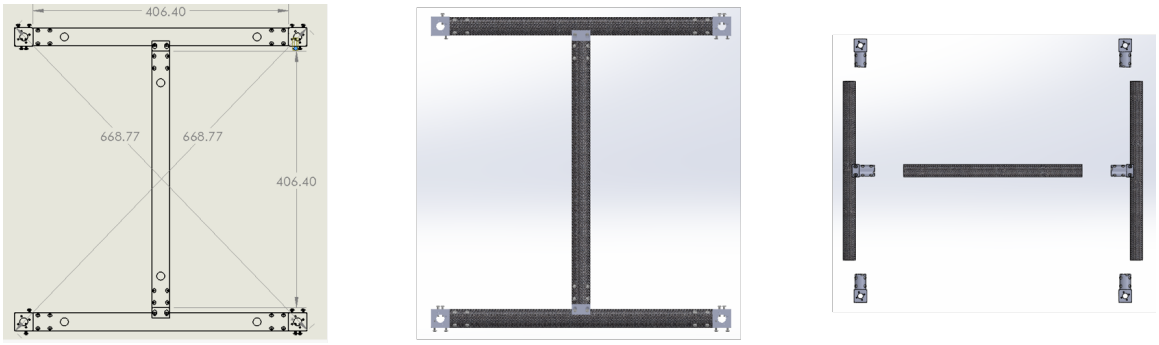

Figure 3.1: Depiction of NV7 conducting mission and gathering turbidity data.

Referring to Figure 3.1, it can be seen that the frame consisted of two parallel arms and one perpendicular tube connecting them. Each tube was connected using RockWest Composite aluminum connectors. In the final design, the chosen front facing orientation

of the NV7 was the direction parallel with the "H" arms. Given the orientation, a large moment force is exerted on the middle tube. If not designed to spec, torsion due to forward and backward pitch motion could cause mechanical failure. Accounting for these mechanics, torsion carbon fiber tubes engineered especially for high torque transfer were used for the entirety of the frame. Although one may think using an H-shape adds complexity to the stability control algorithm, steps were taken to ensure that the multi-rotor would still behave as a regular X-shaped vehicle. The H-design was structured to be an equilateral rectangle. In this method, even though the shape was an "H", the actual underlying design from a computer standpoint was that of a conventional "X" design. Both the perpendicular and parallel arms were of equal length. The dimensions of the multi-rotor were governed by the power system chosen. Since 15 inch propellers were chosen, a 3 inch space was provided as a gap between tip to tip. The final length of each arm was approximately 18 inches. In designing the NV7, steps were taken to construct the most efficient system while ensuring adequate maneuverability. As will be shown later, the larger the rotors on a UAV, the more efficient it will be. Keeping the UAV small reduces weight while heightening its maneuverability. One can see that the final design of the NV7 frame was very simple, consisting of only 3 tubes and 2 connectors. The connectors seen at the end of each parallel arm were attached to the ends of the tubes for the purpose of mounting the motor system. Each connection was made possible by the use of high quality stainless steel screws. Specialized for aquatic climates, both saline and fresh, all components on the NV7 were designed to be corrosion resistant.

3.1.2 Naviator V7 Power System Development

Crucial to the proper functionality of a multi-rotor is an adequate power system. A typical multi-rotor power system is composed of an energy source (ie. battery), motor controllers, motors and propellers. Intrinsically linked, each of these components must be chosen to properly complement each other for the proper optimization of multi-rotor behavior. Striving to keep the NV7 simple and inexpensive, all components considered for the development of the power system were selected from commercially available sources. Although developing a power system with customized components could increase the performance and efficiency

of the power system, the cost and time to develop these components would be impractical. Sourcing data from previous experiments performed in the Experimental Fluid Dynamics Laboratory at Rutgers University, the power system of the NV7 was developed based on both theory and experimental trials. As concluded by the author of [5], multi-rotor efficiency is greatly increased at low motor RPM and increased voltage. To generate sufficient thrust while keeping RPM low, proper rotor sizing was necessary. In keeping with the physics of a

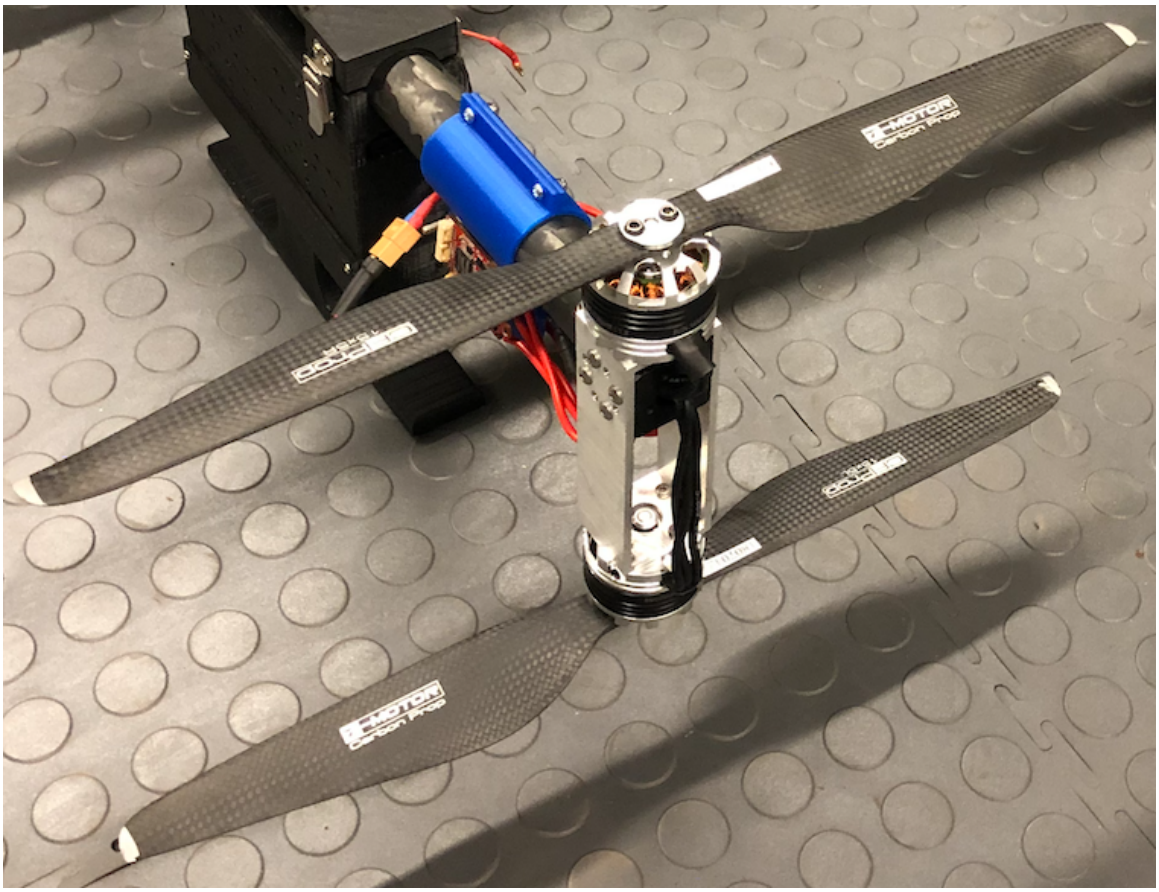

Figure 3.2: KDE 715 KV motor and 15 inch propeller combination.

propeller, one of smaller size will need to spin much faster to produce the same amount of thrust as a large propeller. At the same time, the torque required to spin a small propeller is much less than that needed to spin a larger propeller. Following this logic, a larger motor, yet not too large so as to be overweight, would be needed to spin a larger more efficient propeller. In this vein, rotors had to be chosen so as not to be too large. Oversized rotors would cause the NV7 frame to be enlarged which in turn would contribute to increased

vehicle weight and decreased maneuverability. One can begin to see how each component of a multi-rotor power system must be chosen by weighing in the balance the benefits and drawbacks. Based on prior motor controller experimentation which had proven consistency in both air and aquatic regimes, open-source Flycolor 3s-8s 45amp speed controllers were chosen. In addition, 18650 lithium ion battery cells were selected for the power system

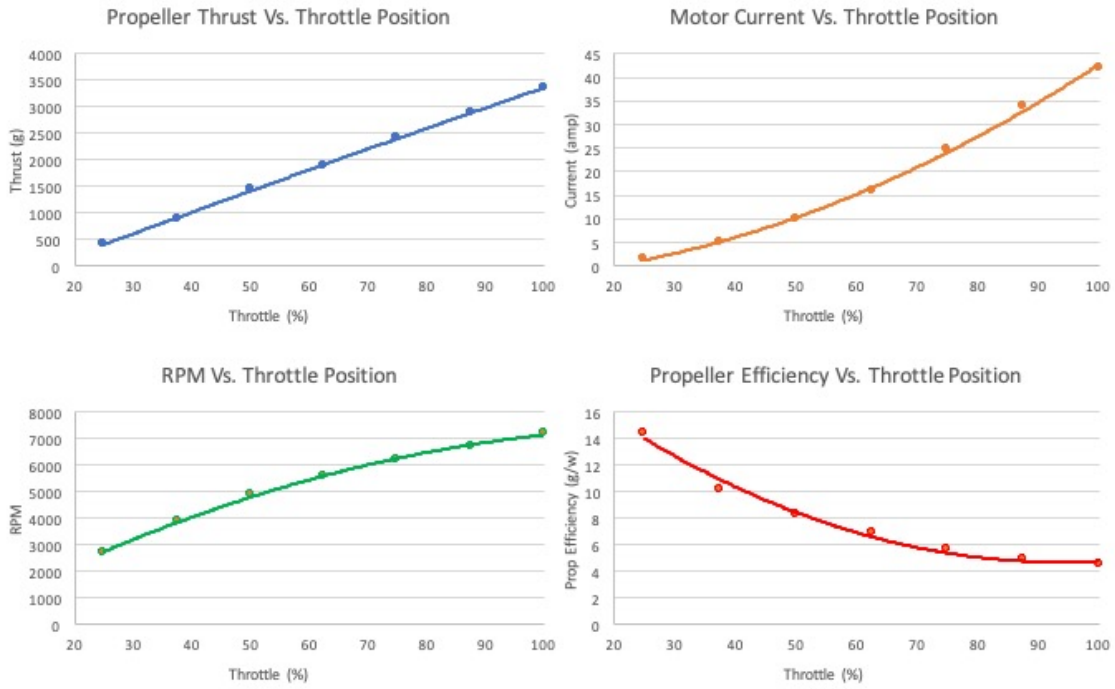

Figure 3.3: Manufacturer data for selected motor. KDE 715 KV motor curves depicting key motor characteristics.

energy source because of their high energy density, discharge rate, customizable form factor and low cost. In a compromise between weight and voltage, a 4s (14.8V), 8p battery system was adopted as the battery of choice. Both the battery and ESC configuration were paired with the KDE 715 KV motor and 15" X 5 pitched propeller. Using manufacturer and experimental data and the components listed, it was projected that each propeller could generate 3,360 grams of thrust at maximum throttle, Figure 3.3.

To settle upon the optimal power system for the NV7, multiple configurations were experimented with. In subsequent tests, factors such as rpm, throttle, torque, current, vehicle weight, thrust to weight ratio, capacity and endurance were analyzed. While not all

configurations were tested, 9 motors who's specifications met those of the NV7 were selected for simulation. In the following figures, plots depicting key power system characteristics are displayed.

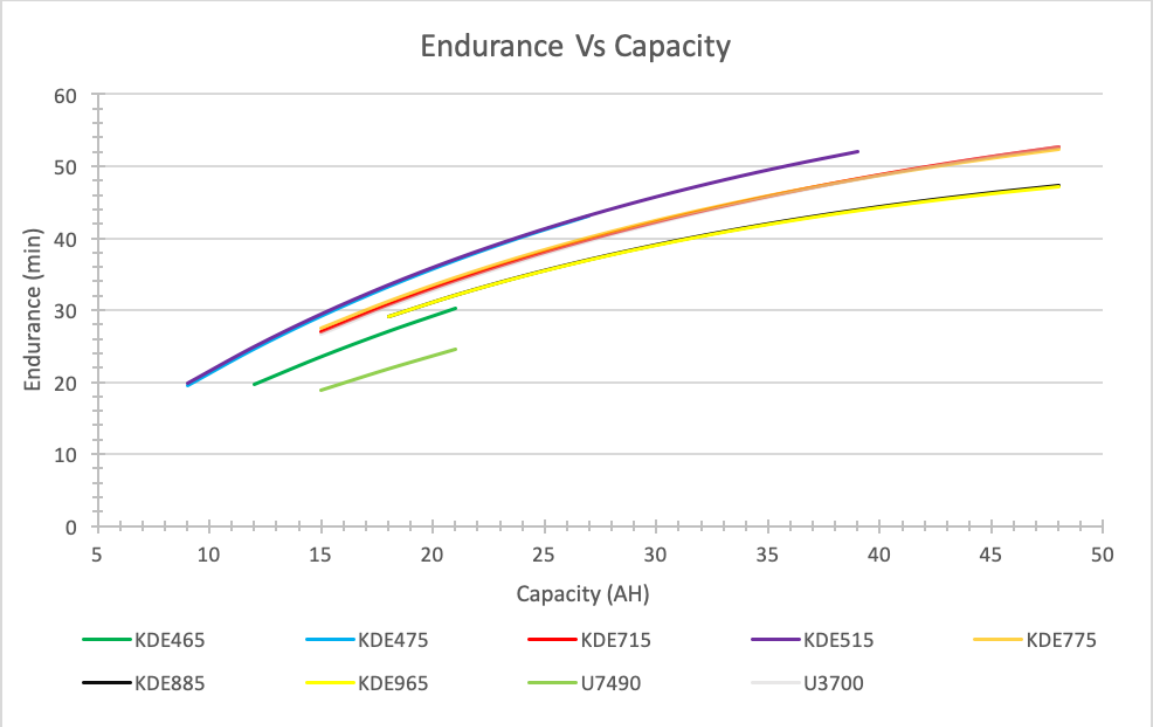

Figure 3.4: Theoretical results calculated from various selected motors using custom software. Vehicle endurance compared to battery capacity.

In the plots, the legend lists the motors used for testing. Each color corresponds to a motor used while the following text refers to the motor brand and kilo-volt (KV) rating. While the data presented in the plots are prone to error, such as inadequate compensation for drag forces, all configurations experience identical error. Keeping such details in mind, although the data presented may be inaccurate, it provides valuable information of the systems compared to each other. For example, an experimental projection may estimate the endurance of a certain power system to be 40 minutes. However, in reality, when numerous unpredictable and unaccounted forces interfere with free flight, the actual endurance may be reduced to as little as 20 minutes. In summary, even though the actual vehicle characteristics may differ from calculated results, the differences between compared systems will be accurate.

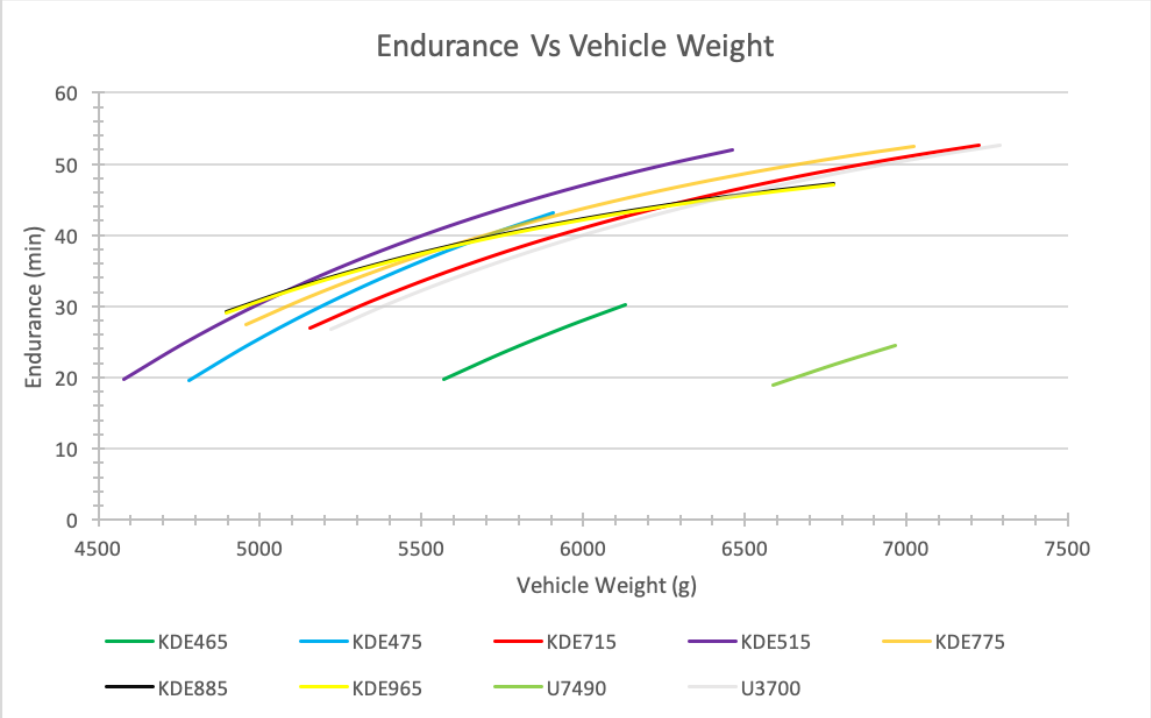

Figure 3.5: Theoretically computed results using custom software. Vehicle endurance compared to vehicle weight.

In Figure 3.4, the endurance of multiple vehicle configurations is compared to various battery capacities ranging from 8 to 48 amp hours. One may see how initially, adding capacity rapidly increases endurance. However, as capacity continues to grow, the increasing rate of endurance begins to wane. If carried much farther, the graphed configurations would plateau and shortly thereafter begin a downward slope. Although Figure 3.4 alone will not offer the optimal configuration, it depicts the separation of two groups. Immediately, one may surmise that both the KDE465 and U7490 are less suited for the purpose of the NV7. Systems KDE715 and KDE775 closely follow identical paths and indicate a slower rate of decaying endurance.

Similar to Figure 3.4, Figure 3.5 offers a comparison between endurance and vehicle weight. In effect, Figure 3.4 offered a comparison between endurance and vehicle weight due to increasing battery capacity. However, Figure 3.5 depicts the effects of both increasing weight via capacity and other payloads. The slight variations in the two plots correspond to vehicle power allocation. While increasing capacity increases vehicle weight, it also increase the onboard power supply. However, increasing vehicle weight with hardware and payloads only reduces vehicle endurance.

A key multirotor characteristic to consider when designing a vehicle, is the thrust to weight ratio (TTWR). Depending on the ratio value, a multirotor may be classified as under-powered or increasingly maneuverable. As is implied by its name, the thrust to weight ratio of a multirotor is the comparison of the full propulsion force to the vehicle weight. If a multirotor's TTWR is too small, the vehicle will be under-powered and difficult to operate. Continuing to decrease a vehicles TTWR will ultimately render it unable to fly. Generally regarded as an acceptable benchmark, a vehicle with a 2:1 TTWR is sufficient for stable operation. As the ratio continues to increase, the agility of the vehicle will continue to escalate. While increasing the capacity of a power system increases weight and leads to reduced endurance, it also negatively affects a multirotor's TTWR. Figure 3.6 depicts the comparison of TTWR versus vehicle capacity. One may see how any increase in capacity simultaneously reduces the TTWR. Once again, two regimes are displayed. As a trend, the graphs presented depict a separation between lower and higher KV motors. Between the two regimes is an offset of approximately 2. Logically, it may be inferred that the lower

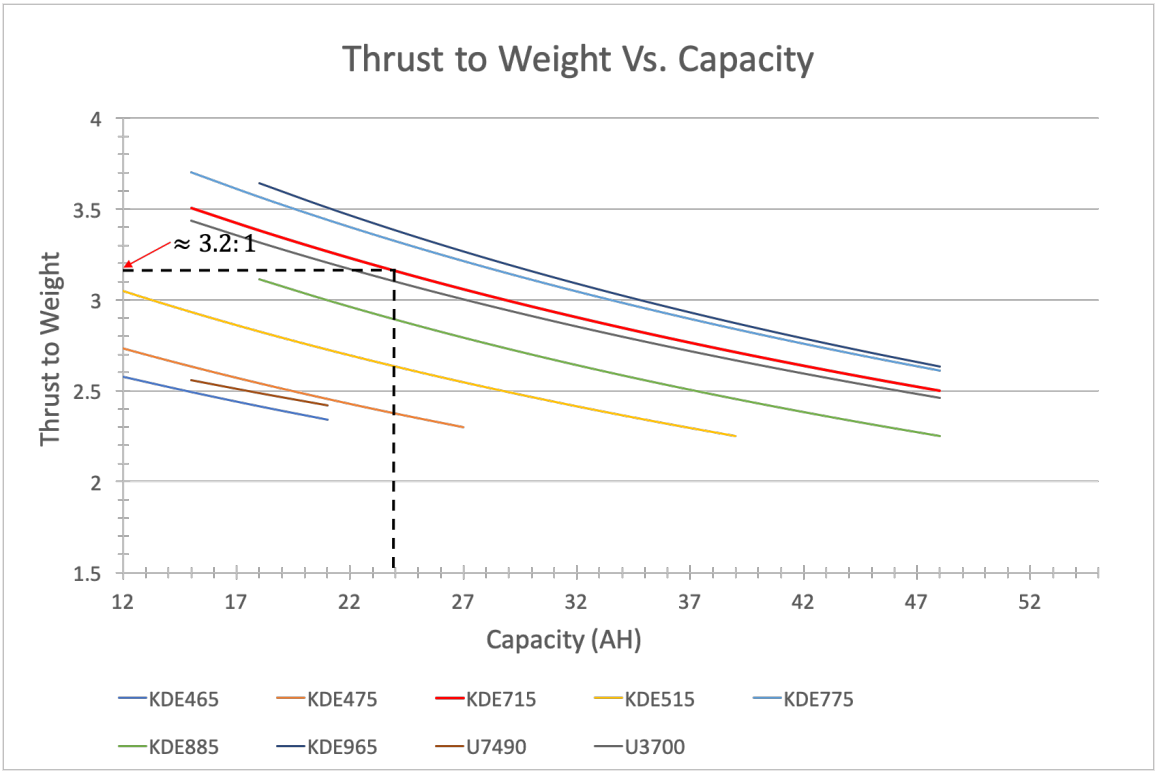

Figure 3.6: Theoretical results computed using custom code. Vehicle thrust to weight ratio compared to battery capacity.

KV motors would be more suitable for the NV7 design. While informative, even with the data offered in Figure 3.6, the optimal NV7 power system can not be determined. For this reason, a comparison of multiple vehicle characteristics must be compared to settle on the optimal system.

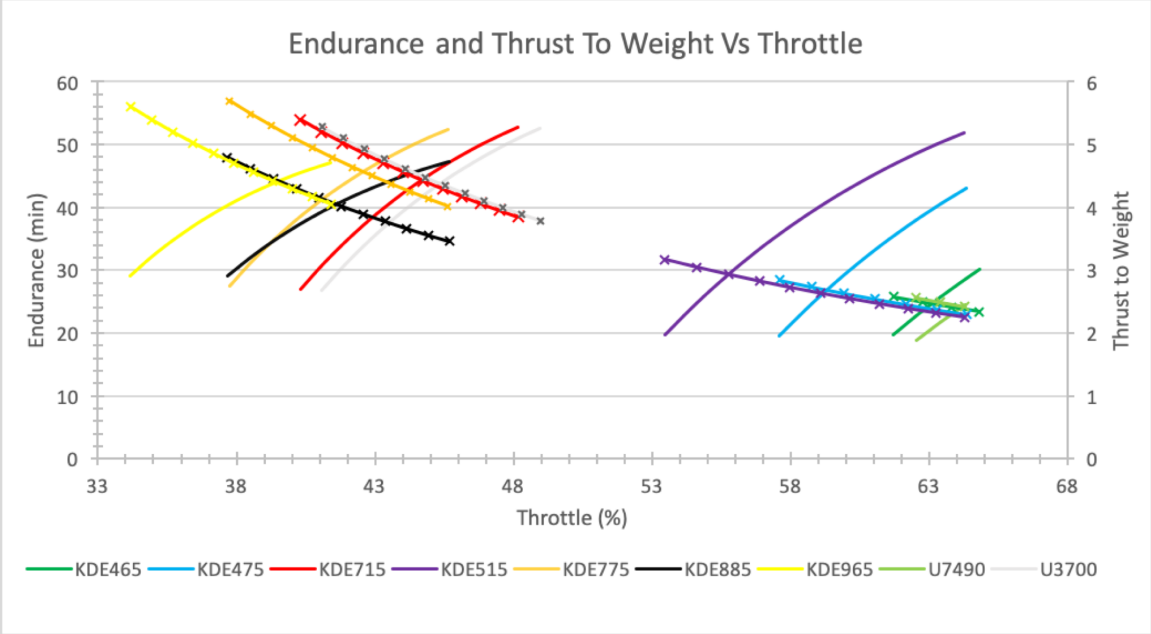

Figure 3.7: Plots generated using customized source code. Vehicle endurance and thrust to weight ratio compared to hover throttle.

Figure 3.7 was developed to depict the process conducted in choosing the optimal power configuration for the NV7. After having concluded the NV7 should possess a TTWR of approximately 3.2:1, it was found that a battery capacity of 24 AH would be a reasonable choice. Although a considerably high TTWR, it was projected that the NV7 would have payloads of approximately 2 kg. With an increased TTWR, the NV7 would continue to perform well despite added weight. Even subjected to a 2 kg payload, the NV7 would still possess a TTWR of approximately 2.34:1. Having settled on the proper battery capacity, Figure 3.7 was constructed. In this plot, endurance and TTWR were compared to the throttle needed to hover. Referring to Figure 3.7, each motor configuration is color coded for both endurance and TTWR versus throttle respectively. The solid lines portray the comparison between endurance and throttle while the lines with x's denote the comparison between TTWR and throttle. Plotting the comparisons in this method allows one to

simultaneously evaluate multiple characteristics and settle upon the optimal system for a given task. Since the NV7 was primarily a vehicle for experimentation, it was necessary for it to possess increased efficiency, endurance and TTWR. Accounting for inherent error, it was concluded that an endurance of 42.5 minutes was required. Even though calculations projected the system would fly for 42.5 minutes, actual flight endurance was later found to reach approximately 20 minutes. However, since all data presented in Figure 3.7 possessed identical error, the deductions inferred from the plot were regarded viable. Referring to Figure 3.8, an endurance of 42.56 minutes was selected. Following the dotted line across to the

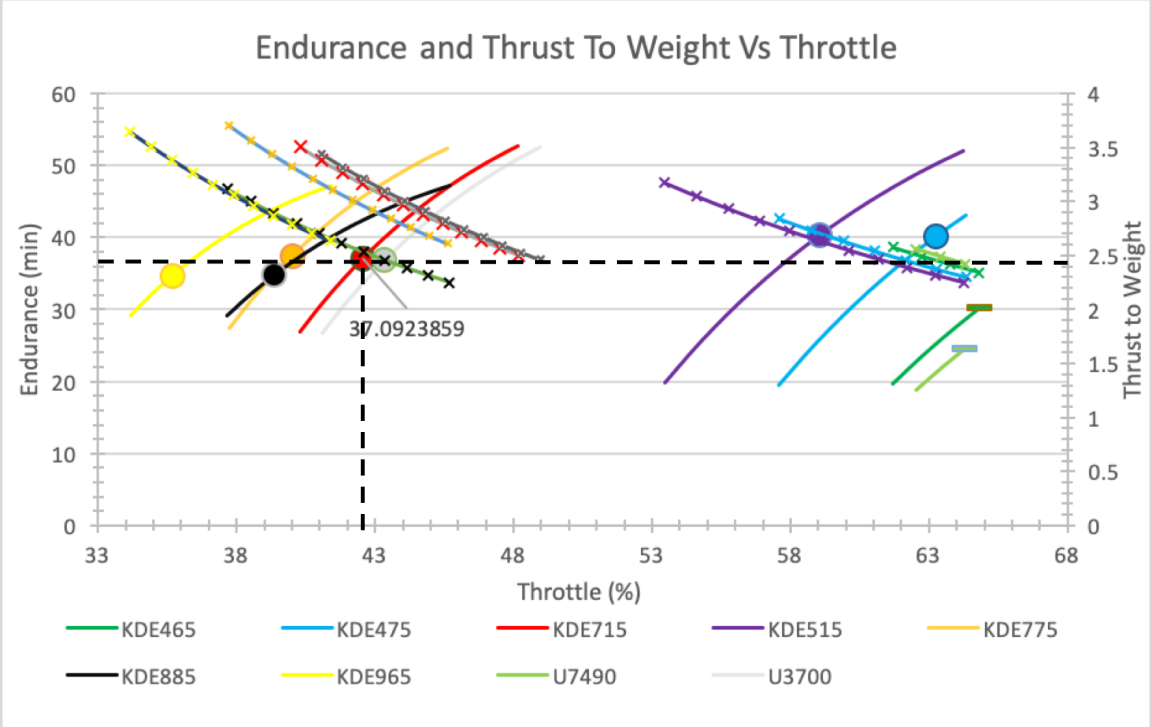

Figure 3.8: Method by which the optimal motor configuration was selected for the NV7. Solid lines correspond to endurance. Solid lines with crosses correspond to thrust to weight ratio. Solid circles correspond to 24 amp hour battery configuration.

right vertical axis of Figure 3.8, it can be seen that at hovering throttle, the system would still retain a TTWR of 2.4:1. Once endurance and TTWR were settled upon, each motor was evaluated to determine optimal efficiency. Looking closely, one may see the small circles on each of the endurance versus throttle plots. Each circle corresponds to the endurance of a system with a 24 AH battery. With such knowledge, it was quickly concluded that the two

motors of choice would be the KDE715 and the KDE775. While the KDE775 would provide a slight increase in throttle efficiency, it was decided to use the KDE715 motor due to its greater diversity. With a lower KV rating, the KDE715 would allow for more flexibility in propeller sizing. With increased torque, the KDE715 would perform with greater reliability when subjected to water propulsion scenarios. With such experimentation, comparisons and plots, it was determined the NV7 system would be composed of a 24 AH battery, KDE715 motors, 45 Amp ESCs, and 15 inch propellers.

The power system for the NV7 was attached to the structural frame in the following manner: the batteries were fixed to the center of each parallel arm via a battery compartment. Each motor was mounted to a bracket and fixed at the ends of the multi-rotor arms. As depicted in figure 3.2, Carbonnect joints were located at each arm end to allow the motor mount to be screwed tightly in place. Between each motor set and battery, a pair of ESCs were clasped to the respective multi-rotor arm. Figure 3.9 demonstrates the nature of the motor mounts.

As before mentioned, the NV7 was projected to have a dry weight (battery and vehicle) of 6kg. With this design factor, certain valuable conclusions may be drawn by referring to the plots depicted in figure 3.3. Note, the data points were provided according to manufacture specifications [27]. In the above plots, motor thrust, current, RPM and efficiency are compared to throttle. Each graph is representative of a single motor/propeller system.

Referring to the upper left plot, it can be seen that each propeller can generate 3.4 kg of thrust at maximum throttle. With the NV7 configuration of 8 motors, at maximum throttle, the multi-rotor is capable of generating approximately 27 kg of thrust. Although the NV7 only weighs 6 kg, it was assumed that multiple sensors would be attached to the multi-rotor. Theoretically, a sensor package weight of up to 7.5 kg can be placed on the NV7 before it reaches a 2:1 thrust to weight ratio. As generally accepted, a 2:1 thrust to weight ratio signifies adequate copter agility [5]. In a study performed by Holzsager, the effect of coaxial rotors will limit the maximum thrust of successive rotors [28]. His studies would suggest that the maximum thrust generated by the NV7 coaxial configuration would not scale directly to 27 kg. However, the losses introduced by the coaxial design can be considered when adding sensor packages to the vehicle. If a 7.5 kg weight is too heavy for

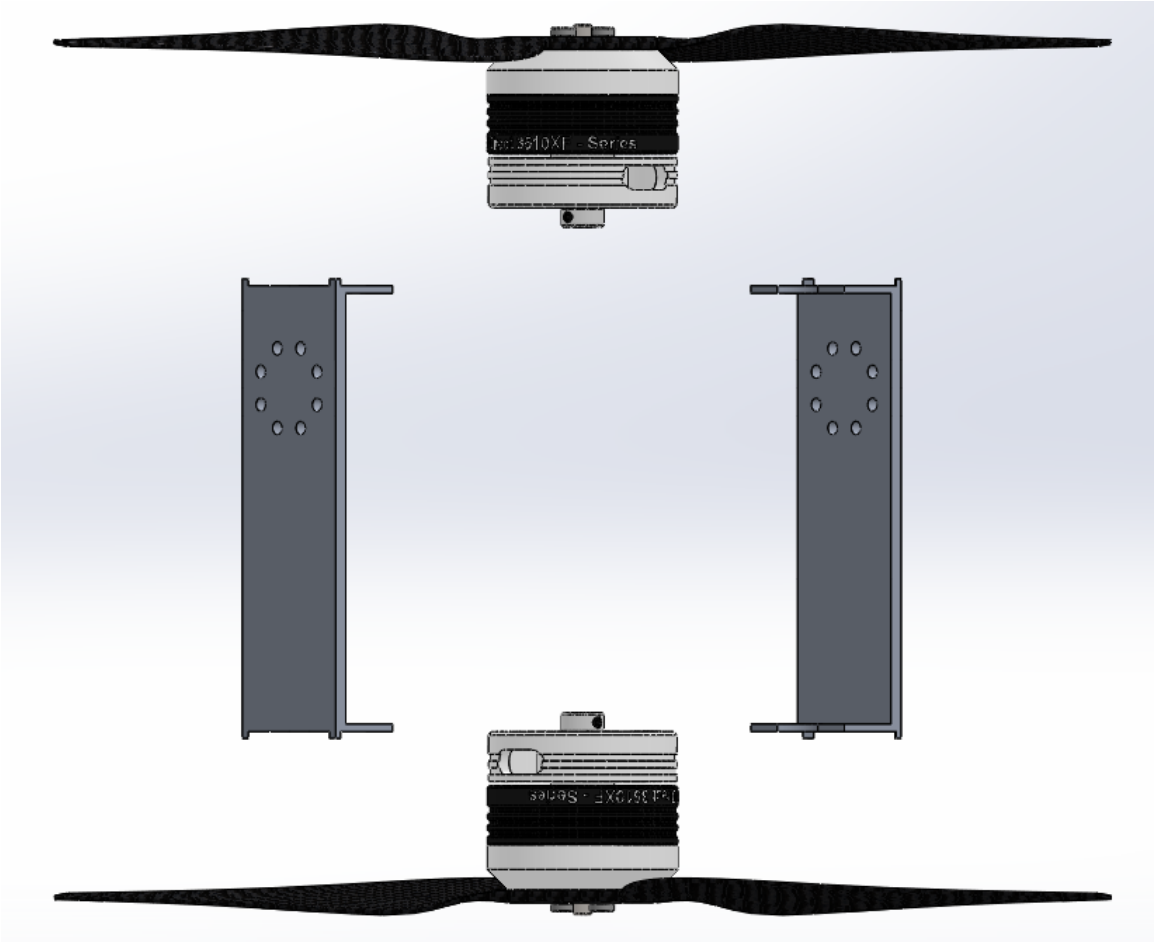

Figure 3.9: Motor mount rendering.

the NV7 to perform well, reduced package weights would need to be experimented with. In the tests performed in this project, sensor packages were limited to approximately 3 kg.

To maintain a fixed hover with dry weight, the NV7 throttle needed to only be at approximately 30%. With this throttle value, it can be seen that the corresponding RPM value is relatively quite low (approximately 3,500). Keep in mind the lager the propeller, the slower the RPM needed to generate the same amount of thrust compared to a smaller propeller. Finally, using the above hovering throttle, one can conclude the efficiency of the system. Derived from the 'Propeller Efficiency' graph, it can be seen that the efficiency of each motor at 30% throttle is approximately 13 grams per watt. Given the above power system characteristics, it was concluded that the system was well suited for the Naviator V7.

3.1.3 Naviator V7 Battery Configuration

While a key component in the development of the NV7 power system, the battery design was optimized for endurance. Once the proper voltage of 14.8 V was chosen for the power energy system, steps were taken to optimize battery capacity. Chosen for this project were the Sony VTC6 18650 lithium ion battery cells. Each 18650 cell provided a nominal 3.6 volts with a capacity of 3000 mah. A battery's configuration is formed of cells in series and in parallel. Cells arranged in series are linked in alternating polarity and contribute to battery voltage, while cells arranged in parallel are linked to identical poles and contribute to battery capacity. In this method, the simplest configuration 14.8 V battery would possess a capacity of 3000 mah and consist of 4 cells in series. A battery of this configuration would be labeled as a 4s 1p system. Using this information, the final endurance of a multi-rotor can be computed using equation 3.1.

$$Endurance = \frac{capacity}{consumption * 8} \tag{3.1}$$

In equation 3.1, capacity is in amp hours and consumption is in amps. Consumption is multiplied by 8 to account for each motor of the octo-rotor. To design a battery with the adequate capacity, one must first decide the required payload. Desiring a 3 kg weight to be attached to the NV7, one must obtain the resulting throttle necessary for hovering

flight. After computing the throttle, use the 'Motor Current' graph in figure 3.1 to find the corresponding current consumption. Given a current of 10A, the multi-rotor as a whole would draw 80A continuously. With the use of equation 3.1 and varying the capacity of the battery, one may obtain the proper endurance needed. In the case of the NV7, a flight time of approximately 30 minutes was needed. Consequently, a battery with a capacity of 24,000

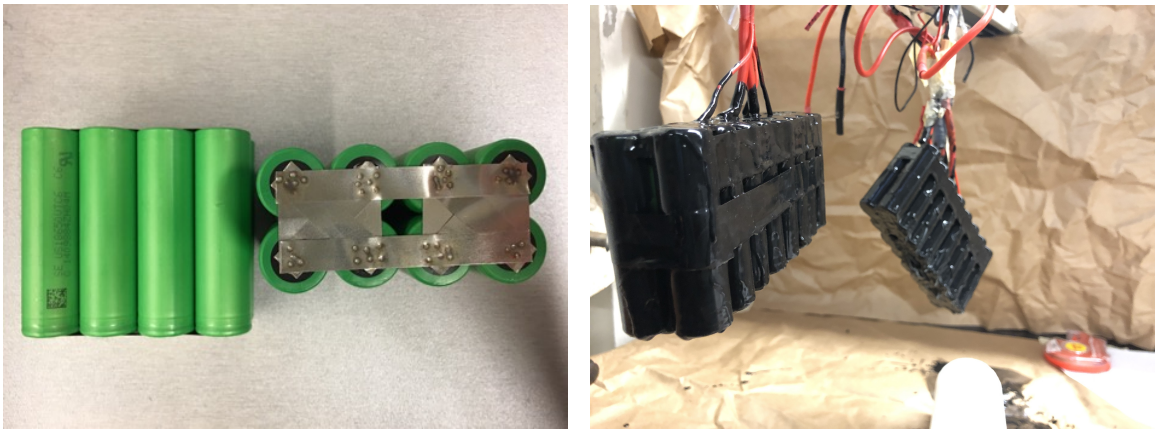

(a) NV7 individual 8p cells. (b) Battery waterproofing method.

Figure 3.10: Images depict the manufacturing process of a lithium ion battery pack using 18650 cells.

mah was designed and manufactured. The NV7 battery configuration would be considered a 4s 8p system. The above equation acts as a guide to battery capacity sizing. Due to many factors in real world scenarios, such as winds and the natural dynamics of constant accelerating and decelerating, actual flight times tend to be less than those computed. In figure 3.10a one can see 2 of the battery pack cells composed of 8 small cells each. In figure 3.10b, the waterproof battery coating process is depicted. Notice that there are two main cables; power and ground. The other small leads are for battery balancing purposes used when charging. Once manufactured, advanced waterproofing methods were taken to ensure complete battery electronics isolation.

To accommodate certain criteria of the NV7 structural design, the battery was designed to be streamlined and replaceable. Combining multiple functions at once, the NV7 battery compartment housed the batteries while serving as the aircraft's landing gear. Designed to be replaceable, one could easily remove the battery cases by merely unlatching tension

clasps. Figure 3.11 offers a clear depiction of the battery housing. Although not shown,

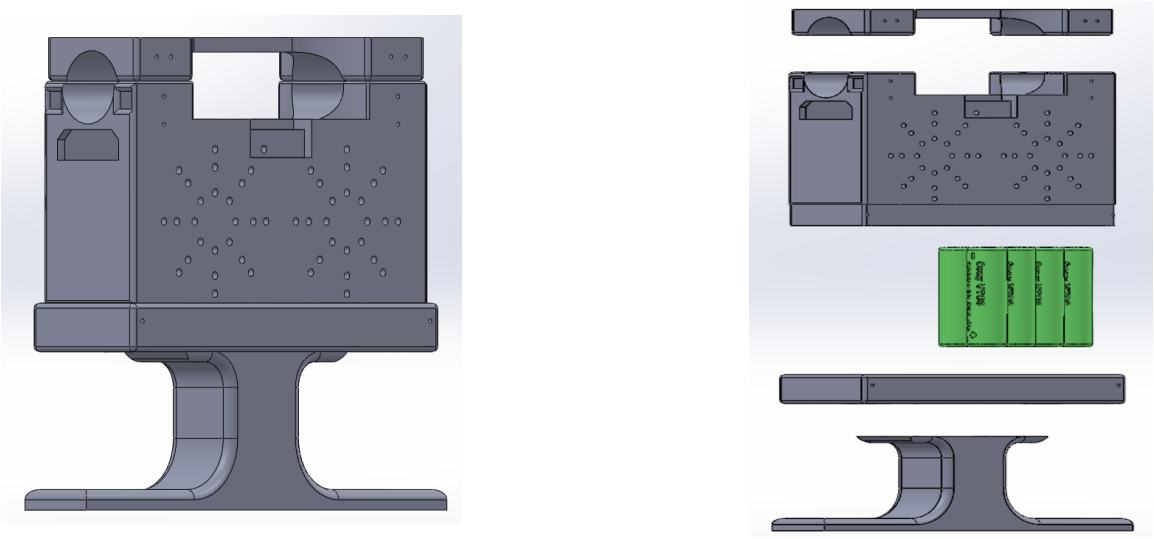

(a) Assembled battery case.

(b) Battery case exploded view.

Figure 3.11: CAD rendering depictions of assembled and exploded battery case. Using such a design allows the battery case to house the aircraft's battery while also serving as the landing gear.

each battery compartment clamped to one of the parallel multi-rotor arms. In this manner, replacing battery packs was easily accomplished without the use of tools. With the ease of battery replacement, one could continue testing in the field with supplementary battery packs.

3.1.4 Naviator V7 Flight Controller and Program Interface

In an earlier section, current popular flight controllers and their respective program interfaces were discussed. Given its user friendly and in-depth programming capabilities, Mission Planner was the chosen software interfacing program of choice. Designed specifically for Mission Planner software, the Pixhawk Mini V2 flight controller was used as the NV7's processor. Possessing ample processing power for this project's purposes, the Pixhawk mini opted as an adequate choice because of its small structural footprint. Since a flight controller must always be available for connecting sensors, re-flashing firmware or conducting calibrations, it was necessary to house the FC in a custom designed water-tight pressure vessel. The

(a) Pixhawk mini.

(b) Mission Planner HUD.

Figure 3.12: Depiction of flight controller and software interfacing program used for Naviator V7.

pressure vessel was designed using CAD software and manufactured using a high precision resin 3D printing process. While keeping all electronics within the capsule dry, power and signal cables among others were connected to the FC. To establish connection in a streamlined fashion, all cabling was reduced to a single 14 pin connector. Utilizing this method, the pressure vessel could easily be released from the multi-rotor frame. Figure 3.13 depicts a complete list of main components in the capsule. No wiring is displayed. Referring to figure 3.13b, the pressure vessel consisted of a cap and main capsule. When connected to the NV7 frame, the cap could be strapped on with Velcro or zip-ties. The lower capsule was held to the cap using both pressure and 4 tension clasps. Inside the capsule was housed the flight controller, receiver and data logger. Although unnecessary for multi-rotor functionality, a data logger was included in the capsule for recording data from water sensors attached to the copter. All communication between inside and outside on board electronics was conducted using the side waterproof UTS 14 pin connector. The bottom connector was used for communicating with the vehicle when performing sub-surface maneuvers. Using the small cylindrical capsule design, easy access to the FC and minimal pressure vessel weight was achieved.

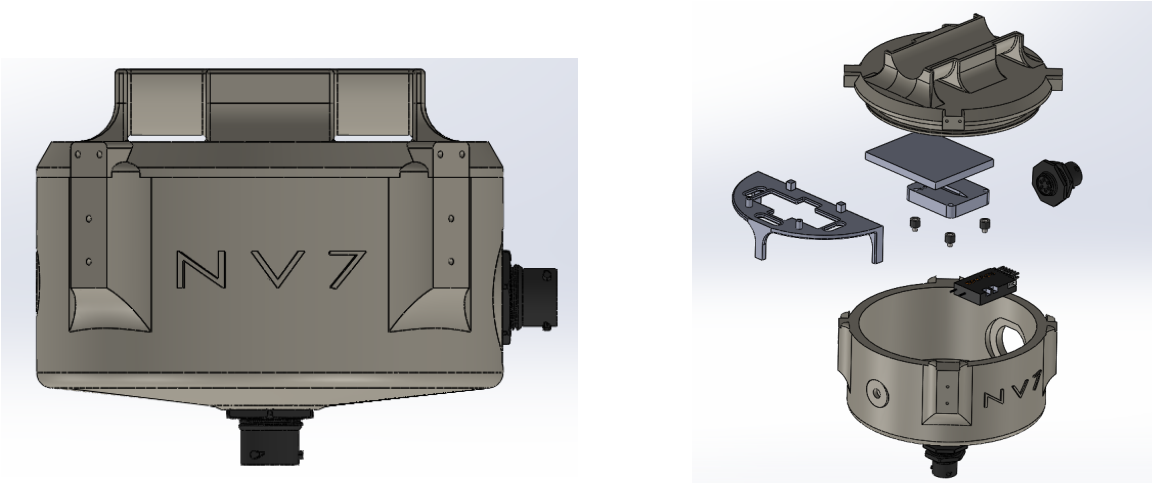

(a) Assembled pressure vessel.

(b) Exploded view of pressure vessel and housed content.

Figure 3.13: High procession resin 3D printed pressure vessel and housed electronics.

3.2 Naviator V7 Completed Fabrication

In its completed form, the NV7 was a fully functional H-configuration multi-rotor.Designed to be modular and easily disassembled, the NV7 was dimensioned properly for convenient transportation. Figure 3.14 demonstrates how the NV7 could be transformed for ease of carrying. Since its design and fabrication, the NV7 was tested extensively in both air and water operations. Systematic tests were conducted in both controlled pool areas and the ocean. In each mission, the NV7 demonstrated characteristics of durability and endurance. In the following chapter, NV7 evaluation testing and results will be discussed. In addition, water quality testing and demonstrations proving the viability of a multi-rotor vehicle for hydro-data acquisition will be discussed.

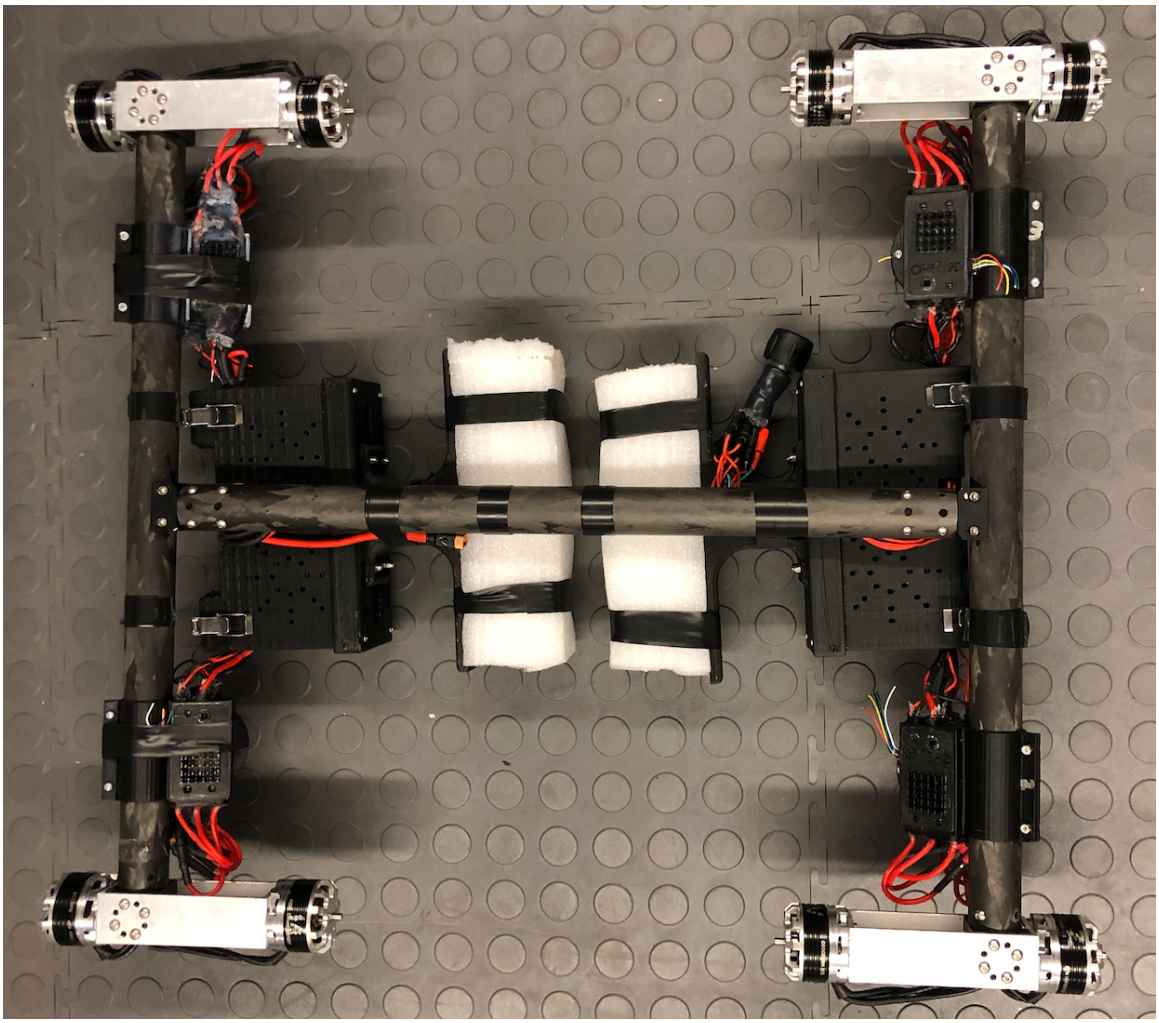

Figure 3.14: Depiction of NV7 in folded form for ease of transportation.

Chapter 4

Testing and Results

Designed for the purpose of assisting users with hydro data acquisition among others, steps were taken to manufacture a remote platform capable of performing special tasks. Adhering to the engineering design process from defining the problem, researching, brainstorming and building prototypes, the fabrication of the NV7 was the defining product of this project. In this chapter, steps will be taken to prove the viability of the NV7 for the tasks at hand. Initial sections will discuss methods comparing the behavior of the NV7 to that of previous Naviators. Ensuing sections will discuss actual tests performed with the NV7 and offer metrics comparing the validity of the data obtained. The credibility of the NV7 will be considered not only in its abilities to function as a multi-rotor and Naviator, but also in its ability to retrieve salient hydro related data. As is fitting with any engineering design, the chapter at hand seeks to perform and evaluate proper testing of the final solution.

4.1 Viability of the NV7 as a Naviator

The creation of the NV7 sought to customize a Naviator multi-rotor for a specific task. While doing so, the design approach to the NV7 reduced vehicle complexity and cost. As before discussed, the simple frame of the NV7 was a fraction of the cost of previous Naviator pressure vessel frames. Without a watertight housing for all electronics, solutions were developed to remedy this novel problem. With the exception of the flight controller, all cabling and electronics were individually waterproofed. Each cable joint throughout the design of the NV7 was waterproofed using a combination of aquatic grade heat-shrink, liquid tape and seal coating. To ensure proper battery waterproofing, multiple coats of liquid seal coating were applied to the battery packs. Finally, the ESC waterproofing process demanded durable measures. Using a 3D printed mould with the ESC positioned inside, marine epoxy

was poured in; encasing all electronic components. To allow heat dissipation, heat sink fins were allowed to protrude through the epoxy surface. Marine epoxy and proper coating techniques, guaranteed the waterproofing of electronics.

Basic to the prerequisites of a Naviator was the absolute waterproofing of the vehicle. Waterproof evaluation of the NV7 consisted of both testing each electronic component individually, as well as testing the functionality of the fully assembled multi-rotor. For cable and battery testing, the components were submerged in slightly chlorinated tap water. Signs of an inadequately waterproofed battery or cable would be the presence of bubbles or over the course of a 2 days, the presence of oxidation. To test the water resistance of each speed controller, a battery, motor and servo controller were connected to the ESC and submerged in water. With the motor spinning continuously, the ESC was kept submerged for approximately 2 minutes. If the motor rotation was consistent for the duration of the time, the

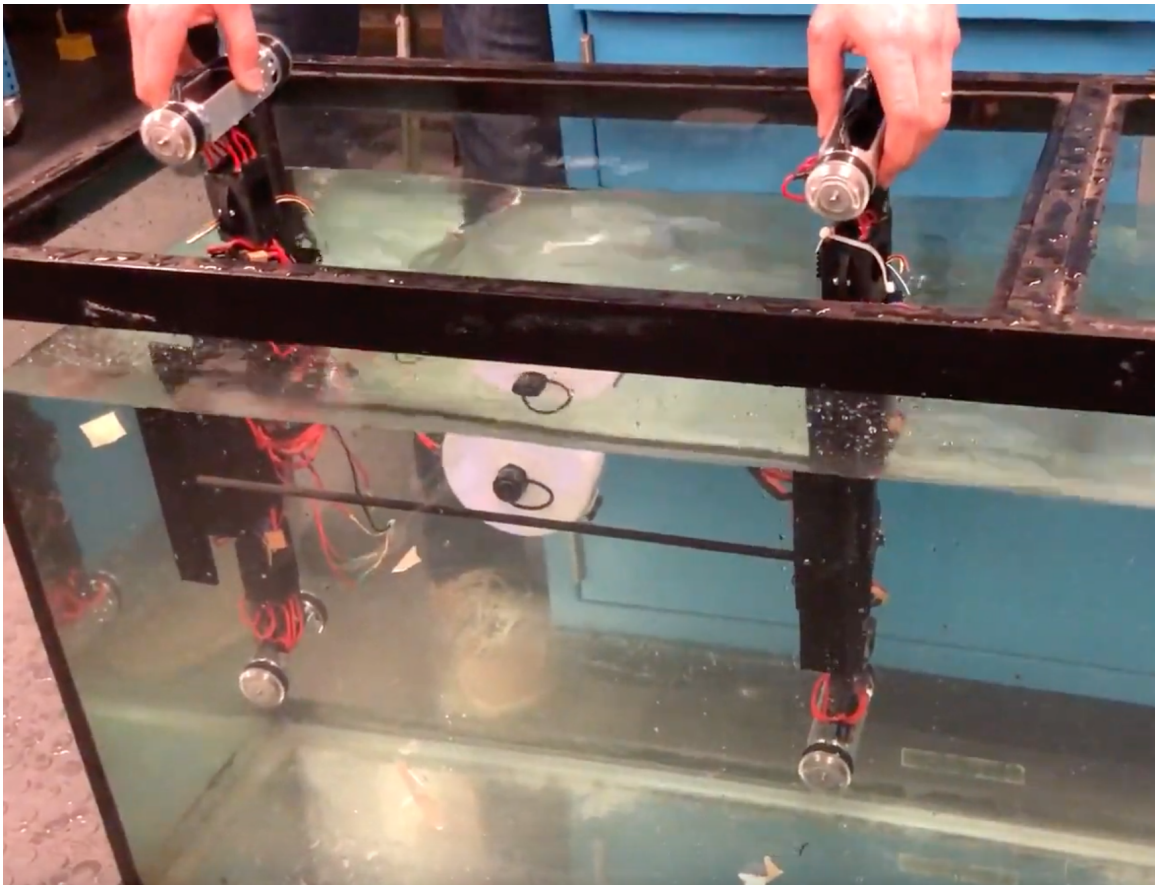

Figure 4.1: Waterproof testing of the NV7.

ESC was said to be water-tight. When testing a powered ESC underwater it is important to ensure it can spin a motor reliably. Even if an ESC does not short and display visual electronic failure, certain errors in the waterproofing process may lead to hardware failure. Spinning a motor while simultaneously submerging the ESC allows one to know the condition of the component immediately. Finally, after ensuring each electronic component was individually water-tight, the fully assembled multi-rotor system was tested for sub-surface functionality. By directly submerging the NV7 completely powered up, any exposed electronics would immediately short. Once submerged, remote stick commands for throttle, pitch, roll, yaw and auto-level were tested. If all vehicle responses were in accord with stick inputs, the basic waterproofing test was considered successful. Subsequent tests were then performed with the entire vehicle at depths up to 17 feet. After successfully completing all the above water tests, the water resistance of the NV7 was considered on par with that of the Naviator standard.

The second and perhaps most important characteristic of a Naviator is its ability to seamlessly transition between air/water mediums. With ongoing research and testing, each version of the Naviator seeks to improve air/water transition maneuvers. It is one thing for a

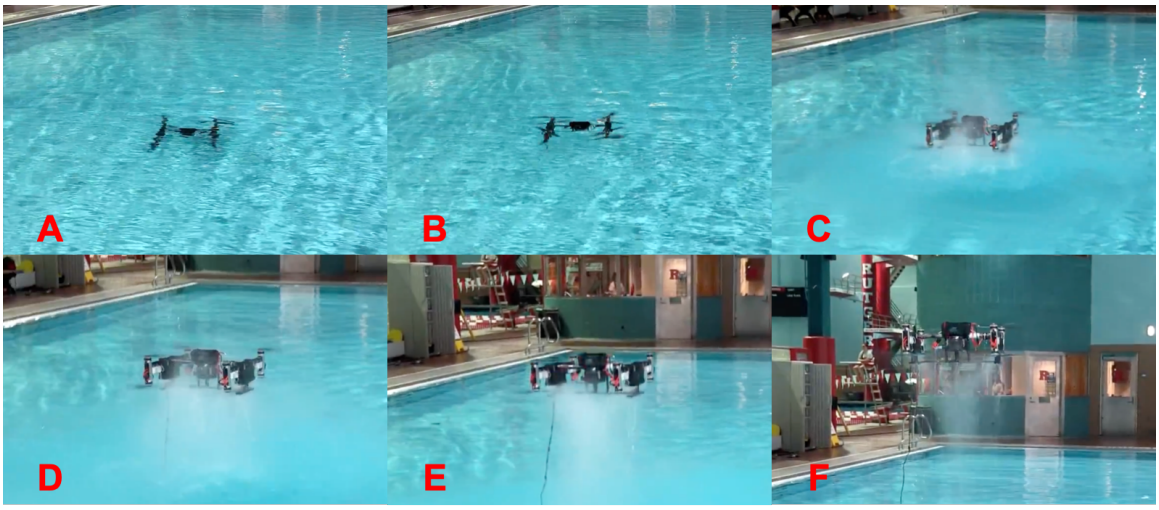

Figure 4.2: NV7 performing a complete transition from water to air.

multi-rotor to successfully transition between air and water, but an entirely different matter to achieve numerous, repeatable transitions. To better monitor the "goodness" of a medium

transition, metrics were devised in which one could succinctly compare a multi-rotor's transition capabilities. Metric standards for transition maneuvers include the following: time required for a complete transition, transition repeatability and consistency and transition sound levels. Referring to Figure 4.2, one can see the NV7 performing steps of a complete water to air transition. Beginning with step (A), the multi-rotor is completely submerged. In step (B), the NV7 is surfacing. Step (C) depicts the NV7 emerging from the water's surface. Finally, steps (D-F) present the multi-rotor's complete emergence and stabilization. Important to note, the time taken to perform steps (A) to (F) was approximately 2 seconds. As is evident, it is crucial for a Naviator to posses the ability to reliably transition repeatably in a timely manner. A complete transition is considered the time it takes a Naviator to shift entirely from one medium and stabilize in the following medium. After numerous trials, adequate medium transition times for a Naviator have been reduced to under 2 seconds [25].

Although one may surmise the transition from air to water is a feat any multi-rotor could accomplish, the elements of a smooth and quiet transition pose challenging metrics. Although not crucial to a successful transition, a smooth and quiet transition demonstrates competent agility. To achieve such a transition, a combination of adequate piloting skill and proper vehicle programming is needed. To reduce transition noise when conducting air/water transitions, the pilot must allow the multi-rotor to descend in a stable, vertical manner. Once the vehicle is about 3-2 feet from the water's surface, the bottom coaxial rotors must be disengaged. In this manner, the vehicle will descend into the water without

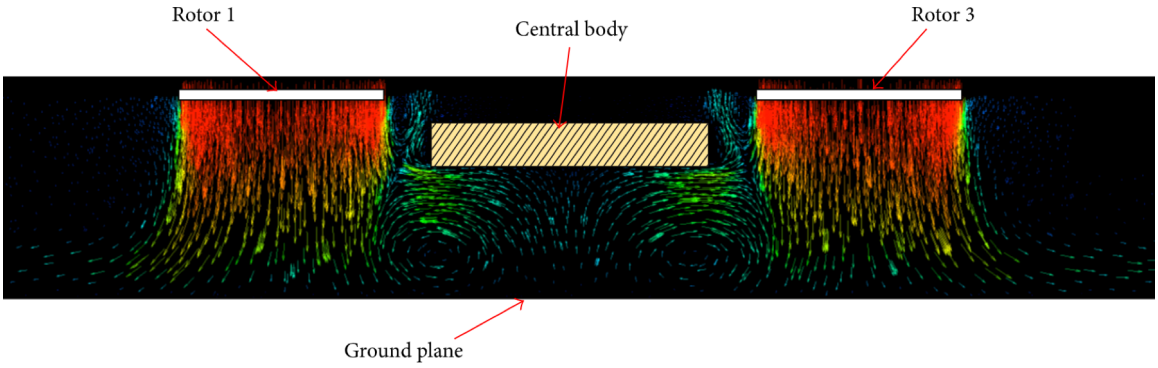

Figure 4.3: Simulation of a multi-rotor experiencing ground effect. [29]

creating turbulent propeller washing. When disengaging the bottom coaxial rotors, the pilot

must adeptly account for the surge in needed thrust from the top rotors to compensate for the thrust lost. Harnessing the benefits of ground effect, rotor disengagement is performed close to the water's surface. Consequently, the thrust gradient compensation is greatly reduced. Figure 4.3 offers a visual representation of the ground effect experienced by a multi-rotor [29]. As thrust is generated, the accelerated air rebounds; generating an air cushion pocket. Once in effect, the thrust generated by the upper rotors may be reduced. After initial contact with the water's surface, the top propellers also are disengaged and the entire vehicle is allowed to submerge. Such a transition may be performed in as little as 1-2 seconds.

As related in the previous two paragraphs, metrics by which to quantify the "goodness" of a Naviator transition were discussed. Given the importance of these Naviator characteristics, this project sought to concentrate design specifications in these areas. Designed with a proper thrust to weight ratio, the NV7 successfully performed continuous medium transitions in as little as 2 seconds. With regard to smooth and quiet air/water transitions, little effort was made to improve NV7 transition sound levels. Although the NV7 fully possessed the ability to perform such transitions, the greater portion of research was directed toward the development of repeatable, seamless water/air transitions. While primarily designed for reliable sensor transport, future work on the NV7 could be focused on the stealth element of air/water transitions.

4.2 NV7 Performance Subjected to High Salinity Regions

As will be discussed in the following paragraphs, crucial to the viability of the NV7 was its ability to perform properly in real world conditions. While most testing in the development process of the NV7 was performed in a controlled pool environment, multiple successful outdoor tests were conducted. The reliability and durability of the NV7 was tested in multiple regions ranging from low salinity pool water to the high salinity Tampa Bay waters. In each mission, shortcomings in the NV7 were realized and mended. A major challenge in highly saline environments is increased conductivity. Commonly measured in siemen per centimeter, the range from just tap water to seawater varies from 800 at maximum to 5500 uS/cm. Incidentally, the NV7 required improved waterproofing methods for these regions.

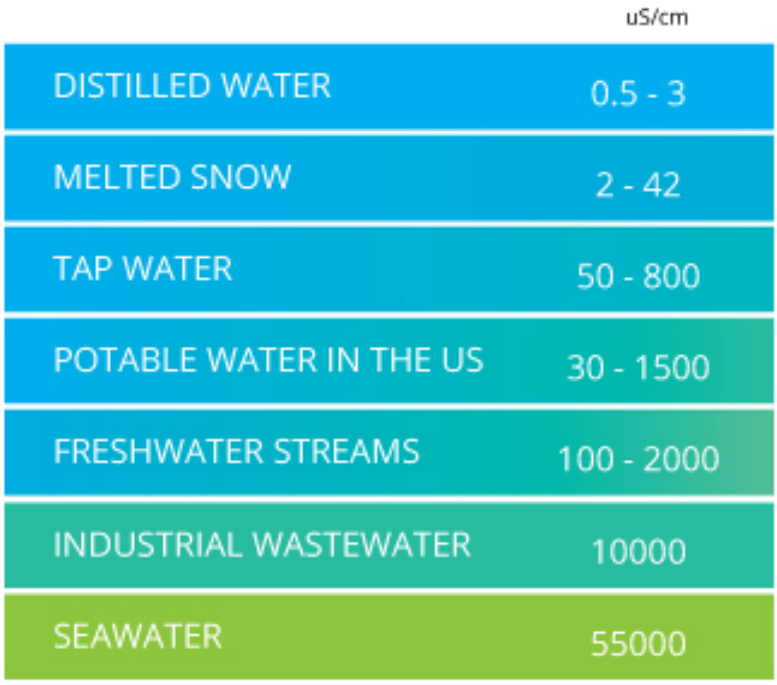

Figure 4.4: Conductivity levels present in various water types. As the water type increases in salinity, conductivity also increases. [30]

In saline water, electronics are prone both to oxidation and signal interference. While testing in the Tampa Bay, ESC signal interference proved to be problematic and required supplementary waterproofing. While numerous successful tests in controlled pool water suggested the NV7 was ready for real world missions, initial outdoor tests speedily curtailed such suppositions. After completing necessary adjustments, the NV7 was deemed worthy of missions in environmentally harsh conditions. The following paragraphs will briefly discuss NV7 missions performed in Tampa Bay and on the coast of North Myrtle Beach.

4.2.1 Tampa Bay Testing

After serving as a testing ground for the NV7's performance in saline water, subsequent missions were performed in the Tampa Bay. As inspiration for one of the many uses of a Naviator, underwater object imaging posed an intriguing topic. Conventionally, subsurface imaging is conducted via manned vehicles or well trained divers. However, one may readily point out the high costs and dangers involved with subsurface manned missions.

Consequently, the mission proposed sought to validate the viability of replacing the task of a diver with that of a Naviator. In said mission, the goal of the NV7 was to serve as a remote multi-rotor imaging 10 objects of interest (ie. bricks). While operated by a remote pilot at the time, future experiments are to be focused on creating an autonomous system for sub-surface imaging. Successful completion of the mission at hand required the NV7 to consecutively transition at each object location and capture video footage of each brick. For the initial mission, each brick was placed in a prealocated location and fully submerged. The depth of of the brick positions ranged from approximately 4 to 8 feet deep. Once deployed, the NV7 was piloted to each object location consecutively. At each point of interest, the NV7 would completely submerge to the ground floor while imaging each brick. Figure 4.5

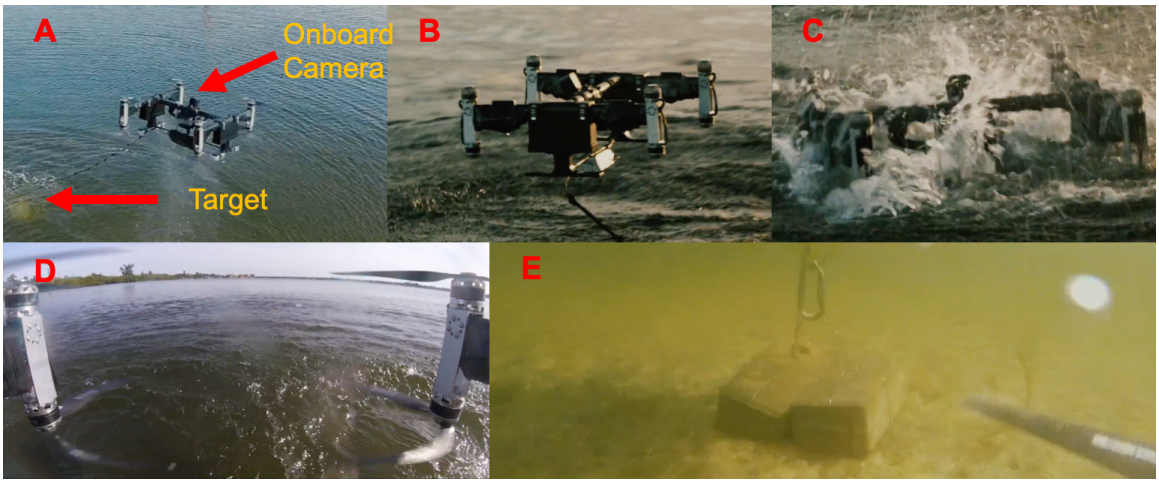

Figure 4.5: NV7 performing sub-surface object searching operation.

depicts both the view of the pilot in operation of the vehicle as well as the camera view on the vehicle. In step (A), one can see the targeted object. All underwater footage was recorded with the GoPro camera attached to the frame of the NV7. Steps (D and E) depict images collected using the onboard camera. After collecting salient footage, the multi-rotor would transition to air and fly to the next point of interest. Once all bricks were imaged, the process was repeated a second time before the NV7 returned to its ground station. In this manner, the abilities of the NV7 to perform 20 consecutive transitions while capturing salient footage were clearly demonstrated. With ongoing experimentation, the Naviator platform could be developed into a formidable system for numerous subsurface missions such

as object searching and evaluation.

4.2.2 North Myrtle Beach Testing

With a combined task of developing methods for retrieving water data and evaluating the performance of the NV7 in turbulent conditions, testing was conducted on the North Myrtle Beach coast. Reserved specifically for academic use, multi-rotor operation could be per-

Figure 4.6: Map listing key features as well as intended fight plan.

formed in a safe manner. Both the flight layout and plan is depicted in Figure 4.6. In this mission, having attached a dissolved oxygen probe to the vehicle, the NV7 was planned to land just before the breakers on the ocean side and log data. Although the data retrieved was not analyzed extensively, it provided an educated approximation of the surrounding dissolved oxygen content. In the more immediate scope of the mission, the performance of the NV7 transitioning with a sensory payload in turbulent waters was of greater importance. Due to the long distances the NV7 needed to fly beyond the breakers, the ensuing flights were conducted tetherless. Since radio waves are very limited to water penetration, a float system was placed on the NV7 frame to keep it slightly buoyant. However, due to the transmitter antenna lengths, problems were still experienced with radio connectivity. Although modified for subsequent tests, the challenge of limited flight distances was remedied by placing the pilot in command in closer proximity to the vehicle landing sites. Aside from this limitation, the major objective was the transitioning ability of the NV7 in rolling waves. After multiple

tests in which the NV7 successfully transitioned, it was deemed reliable enough to entrust high cost sensory payloads for outdoor missions.

While evaluating the transitioning capabilities of the NV7 was key in these experiments, the data collected demonstrated the versatility of the platform. As the NV7 maneuvered from location to location, it gathered salient dissolved oxygen data. In this method, the platform performed remote data acquisition from multiple points of interest in a streamlined manner. Presenting the data in Figure 4.7, the average dissolved oxygen concentration

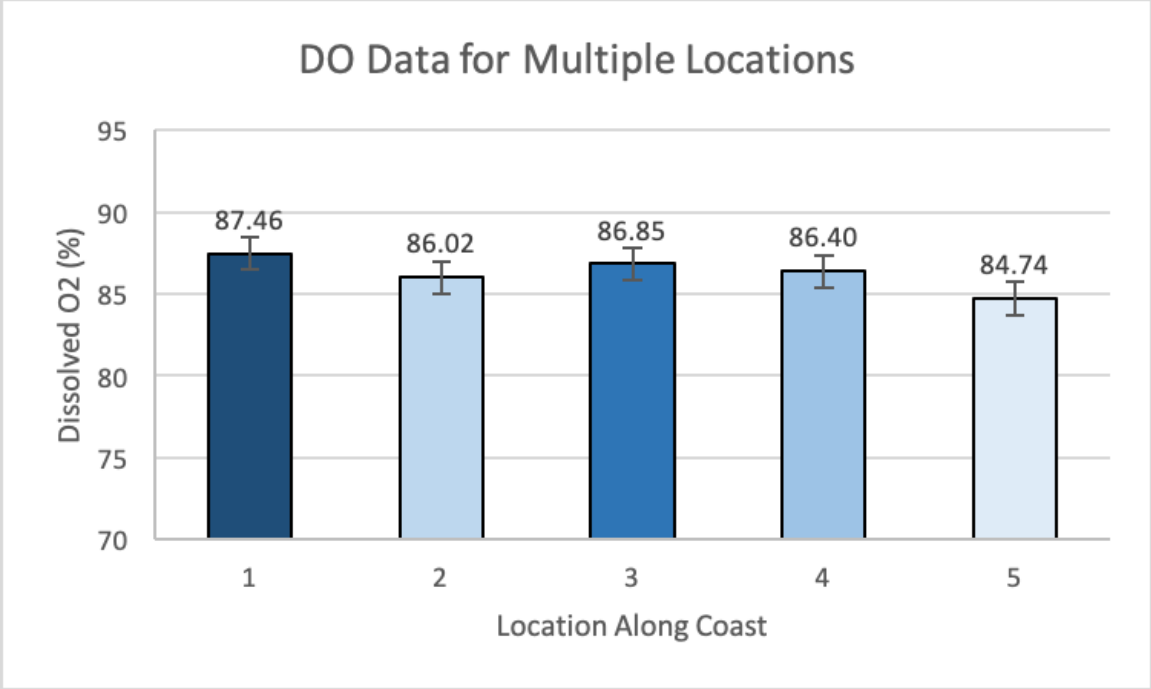

Figure 4.7: Dissolved oxygen data collected at five remote locations using the NV7 platform.

at each location was computed. Although the data fluctuates at each location, the measurements are quite similar. While the greatest deviation existing is 2.72%, such variations could be due to measurement errors. For this reason, further analysis would be necessary before one could safely claim there was an actual 2.72% decline in dissolved oxygen from location 1 to location 5. While further testing was needed to evaluate the accurateness of the measurements, the tests demonstrated the vast potential of the platform for expedited remote water quality missions.

Satisfied with the results of the Myrtle Beach experiments, subsequent, missions have

been conducted in Red Bank New Jersey along the Navesink River. In these tests, experiments have been performed in conjunction with a Blue Robotics ROV to demonstrate the capabilities of remote heterogeneous vehicle collaboration for hydro data retrieval. However, in order to verify the advantages of a joint effort in water data retrieval, tests and results must first be offered depicting the viability of the NV7 for recording accurate sensory data. In the following section, experiments validating the use of the NV7 for water monitoring and the subsequent data will be discussed.

4.3 Viability of the NV7 as a Remote Hydro Data Retrieval System

To validate the use of a multi-rotor for the purpose of water monitoring, it was advantageous to conduct testing using salient factors influencing the quality of water. While there are many characteristics affecting water quality, turbidity and dissolved oxygen were chosen for there popularity and importance. In an effort to demonstrate the viability of the NV7 for water monitoring, experiments were conducted comparing manually retrieved and multi-rotor retrieved hydro data. To properly establish experimental credibility, a pair of high grade, reputable sensors and a data logger were selected for testing. Popular among credible sources were the Global water WQ730 turbidity sensor, WQ401 dissolved oxygen sensor and GL500-2-1 data logger. Both designed to be either manually held or attached to a buoy for data logging, it was necessary to evaluate if the data retrieved by designed means corroborated with data retrieved utilizing the NV7 platform. As before mentioned, the sensors were attached to the frame of the NV7. Each sensor was connected to the analog to digital converter data logger housed inside the vehicle pressure vessel. Figure 4.8 depicts the sensory wiring schematic used. In the following subsections, the characteristics of turbidity and dissolved oxygen as well as the experimentation and data evaluation will be discussed.

4.3.1 Turbidity Testing

Turbidity, a common hydrologic parameter, is an optical property used to describe the opaqueness or clarity of water. Many factors can affect the level of water turbidity, including colored material, and most notably, suspended solids. While there are multiple sub-methods

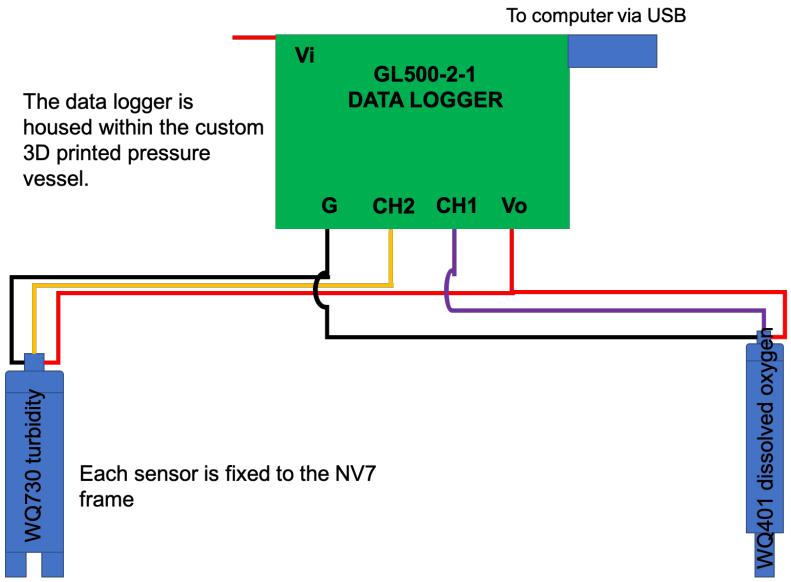

Figure 4.8: Sensory wiring schematic.

for measuring water turbidity, two heterogeneous methods are measurements relative to water clarity and direct measurement of turbidity. First, measurements made relative to water clarity is an inexpensive yet potentially inaccurate means for determining turbidity. Solely composed of a secchi disk or clear tube, this first method depends on human abilities to decipher the resulting turbidity. For this reason, indirect turbidity measurements often are inaccurate; experiencing bias. The latter method of direct measurement offers a much more accurate and reliable method for determining and quantifying turbidity levels. With the introduction of novel technologies, numerous methods for quantifying direct turbidity measurements have been developed. Although each has its own drawbacks, the method chosen for this project utilized the most reliable and commonly recognized USEPA Method 180.1. As the standard for United States Environmental Protection Agency, Method 180.1 performs measurements based on light scatter [31]. Known as nephelometry, methods of this nature use a combination of sensors to produce and detect light scatter. Referring to Figure 4.9, one may see the operating principle of a nephelometric turbidimeter. As the light source on the left hand side of the sensor emits a light beam into the water sample, two strategically positioned photodetectors measure resulting light intensities.

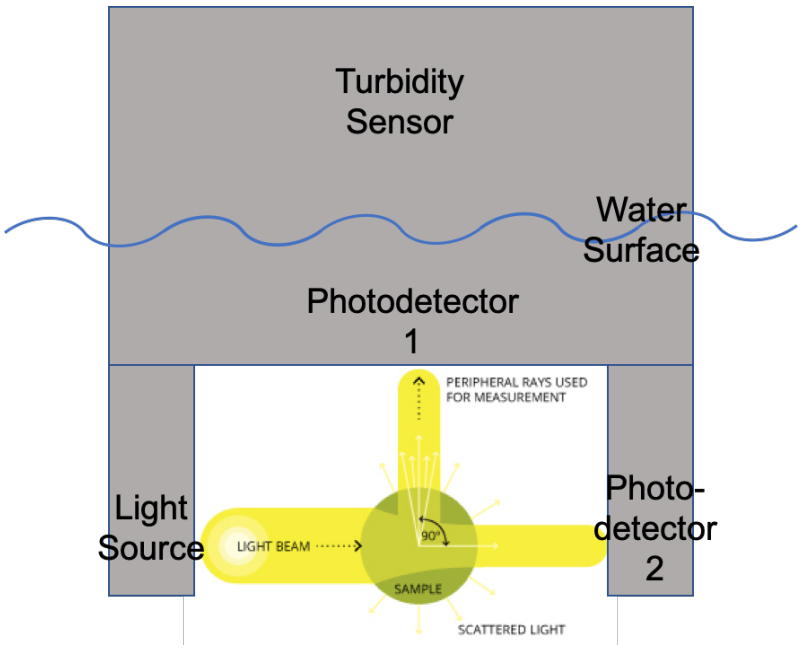

Figure 4.9: Schematic depicting USEPA Nephelometric terbidimeter operating principle. [31]

Interestingly, turbidity units such as NTU have, "no intrinsic physical, chemical or biological significance" [31]. Turbidity units cannot be converted to any other units. Although there are various sensor positioning techniques, basic guidelines have been established to ensure proper data acquisition. Operating on the above principle, the sensor used for this project performed measurements via a 90 degree scatter nephelometer. Focusing a beam into the monitored water, emitted light reflects off suspended particles. The resultant light intensity is then measured by photodetector 1 perpendicular to the projected beam. Drawing on the principles of light scatter, the resultant measured light intensity is directly proportional to turbidity content. To correct for intensity variations, color changes, and minor lens fouling, photodetector 2 is positioned directly opposite the light source [32]. In this manner, direct turbidity measurements are obtained in nephelometric turbidity units (NTU) [31]. For this reason, turbidity sensors utilizing various light configurations cannot be compared. Given the nature of turbidity, measurements collected by a turbidimeter do not provide information on the quality of the water body. For example, just because a body of water is clear, ie. low turbidity, does not mean the water is healthy. Figure 4.10 presents a plot of a

typical low turbidity region. Although the turbidity is low, the chlorinated pool of which the data is representative, was not suitable to drink. To harness the full potential of turbidity measurements, it is important to compare data over time. The presence of turbidity shifts will provide vital indications as to water health [31].

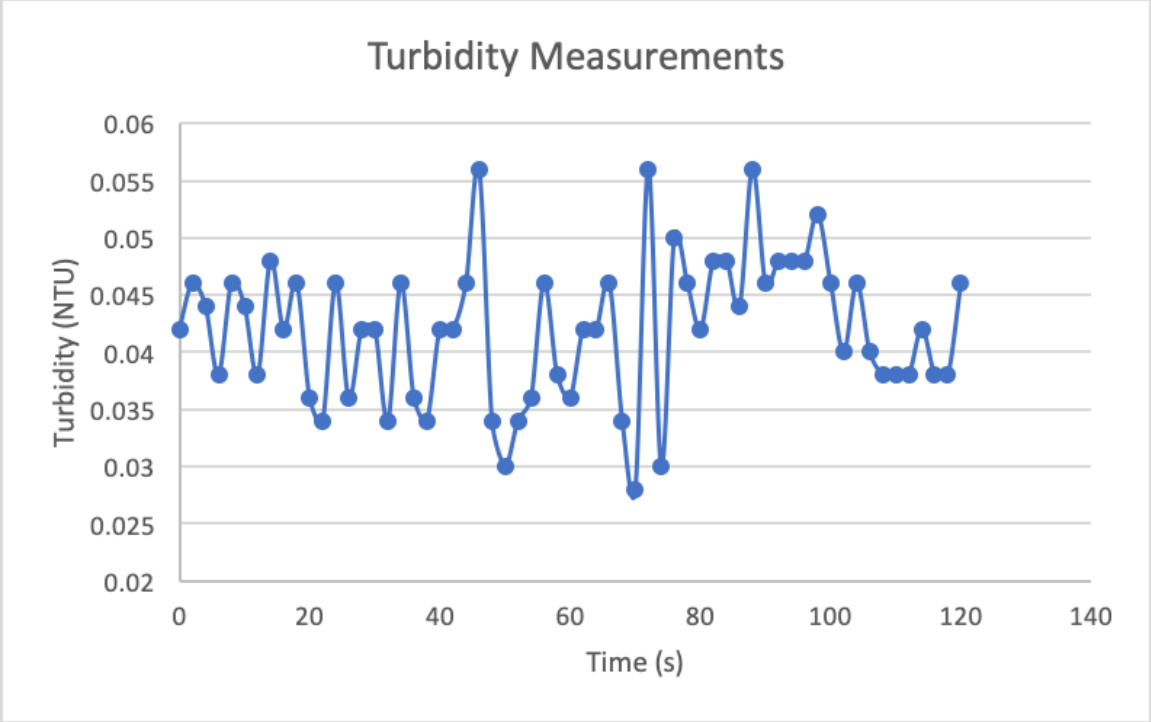

Figure 4.10: Sample turbidity measurements accumulated over the course of 120 seconds. Measurements were taken once every 2 seconds.

Utilizing the NV7 platform for data acquisition, three methods for collecting measurements were experimented with. Each method altered the behavioral characteristics of the NV7. First, experiments were performed by flying the NV7 to points of interest and transitioning at each location. At each transition point, while the NV7 remained surfaced for an extended period of time, continuous sensor measurements were performed and logged. Secondly, missions were conducted by flying the NV7 to points of interest. At each location, the multi-rotor remained hovering above the water's surface while the onboard sensor was submerged to a proper depth. Finally, experiments were conducted to continuously log sensor data. In these missions, while the NV7 followed a predefined course with constant motion, the onboard sensor was dragged through the water. Using these methods, various facets

of mission performance and data acquisition were explored. While each method possessed benefits, so also, each experienced inevitable limitations. Solely consisting of floating and data logging, the first method allowed for extended logging periods and abundant sampling at each transition location. However these tests tended to be lengthy when compared to the continuous motion experiments. As a middle ground between long term sampling and continuous sampling, the second test allowed for quick single location measurements. Due to battery constraints, the time spent at each hover location was limited. Consequently, the data acquired at each location was not as extensive as that obtained utilizing the first experimental procedure. Already alluded to, the benefit of the third experimental procedure was the expedited method in which data was continuously obtained. Using this method, large areas could be sampled in reduced time periods. However, given the continuous motion of the system, data retrieved throughout the mission path was limited to the velocity of the multi-rotor, sensor reaction time and sensor sampling rate. For this reason, it was advantageous to gain a comprehensive understanding of the sensors used.

While one could easily record sensor measurements, without a proper understanding of the sensor's dynamics, the data would possess limited validity. Key to determining the viability of a data set, is the understanding of the sensor's reaction time. With this knowledge, the time needed to secure stable sensor readings would be established. For this reason, numerous experiments were performed with both the turbidity and dissolved oxygen sensor to determine their reaction times.

Beginning with the turbidity sensor, tests were performed to ultimately determine the time the sensor would take to reach stable output values. In these tests, 6 cycles were performed. Each cycle consisted of placing the probe in a water bath for 60 seconds. During this time, the sensor sampled measurements every 2 seconds. Once compiled, the results were plotted. Using manufacturer specifications, error was projected to be 1% of the full scale. Following Figure 4.11 the compiled turbidity data can be visualized. In this plot, each solid line represents the turbidity data measurements for each test over a 60 second period. The error bars correspond to the 1% error which correlated to 0.5 NTU. With the exception of the Test 1, all tests begin by only varying by approximately 0.1 NTU. With an allowed error of 0.5 NTU, if not accurate, the measurements are very precise. All measurements

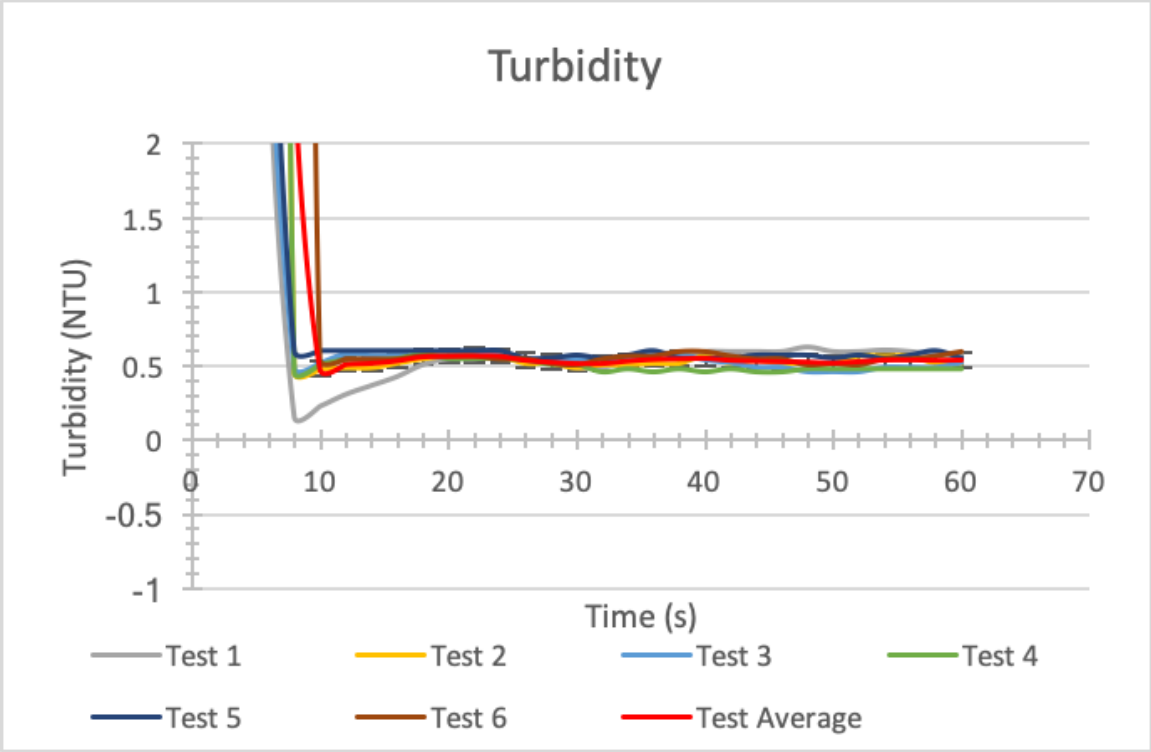

Figure 4.11: Depiction of both experimental turbidity data and error.

remained well within the allotted error range.

After computing the mean projection of the turbidity tests, the resulting data was compiled in Figure 4.12. Reversing the vertical axis, the resulting graph afforded a simpler method for analyzing the data. As reflected, sampling time began at time 0 and ended at time 60. Turbidity fluctuated from 50 NTU in air to approximately 0.547 in water. After approximately 12 seconds, the consecutive measurements largely remained at a constant value. T_s is the time taken for the measurements to settle and tau is the time constant. As can be read from Figure 4.12, the sensor settling time was 12 seconds. At 63.2% of T_s, tau is 5s. The time constant is commonly used to represent the speed with which a system will reach 63.2% of its final value. The specific percentage is obtained by recording the time taken for a parameter to vary by a factor of

$$1 - 1/e$$

or 0.632. In this method, after 5 seconds, the data will possess a confidence level of 63.2%. After 12 seconds, the confidence level will have increased to 99%.

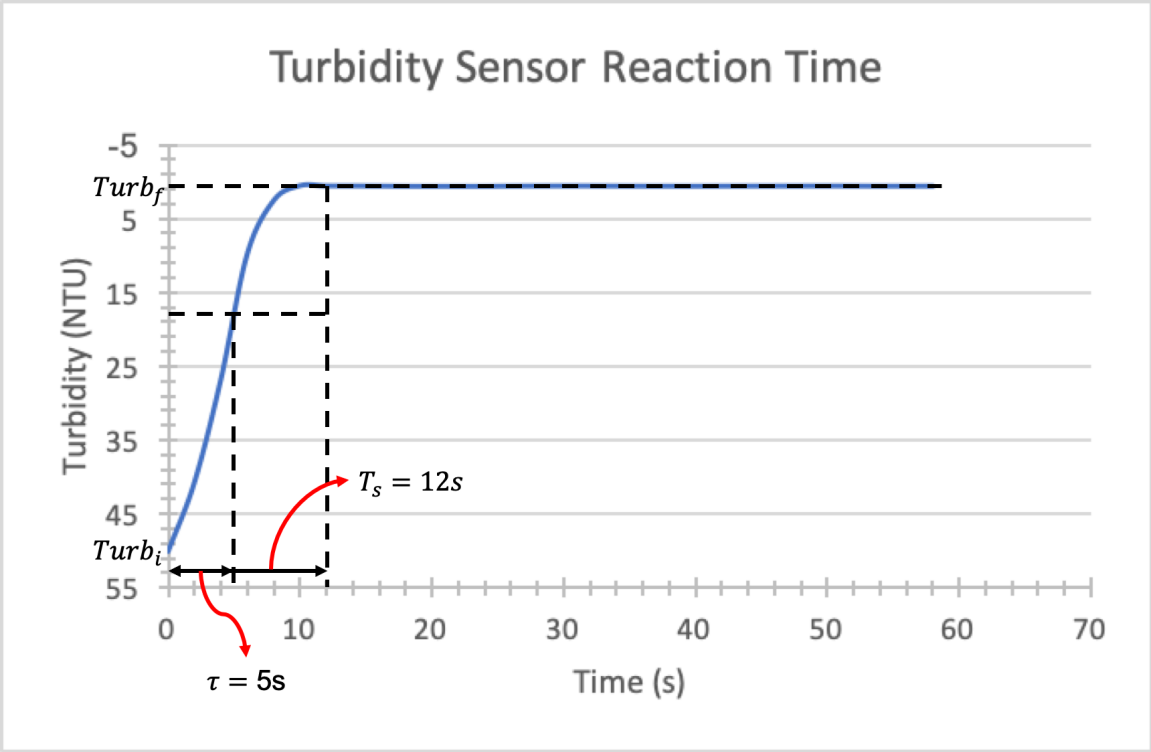

Figure 4.12: Global Water turbidity sensor reaction time.

With this data, it was determined that the turbidity sensor would operate well in all three experimental methods. For method 2, it would be important for the sensor to remain submerged for at least 10 seconds to begin recording accurate data. For method 3, it would be crucial for the multi-rotor to progress at slow velocities. As the velocity of the multi-rotor increased, the confidence level of the measurements would decrease. The nature of test 3 would primarily suite missions that required solely average or general data. Combining the three experimental methods, a robust data acquisition system could be developed. For example, if a body of water needed monitoring, the process of gathering data could be achieved in 3 steps. First, the system would be deployed for continuous, ballpark sensor measurements. Once analyzed, key areas could be pen-pointed and sampled via quick hovering and logging maneuvers. Given a more secure knowledge of the actual points of interest, the NV7 platform could be deployed to each location where it could transition and gather data indefinitely. With each step, the resulting data from each location would possess ever increasing validity. In this method, points of interest could be narrowed down quickly and

monitored with ease.

Of importance to this project was the ability to retrieve consistent data readings both manually and using the NV7 platform. As such, concern was not focused on the accuracy or meaning of the obtained turbidity data. Following standardized testing procedures, experiments were performed for the purpose of evaluating manual and multi-rotor retrieved data. Experiments regarding turbidity measurements were comprised of 5 manual and 5 multi-rotor tests. Each test was conducted by submerging the sensor and logging data for a 120 second period at .5 Hz. In this manner, every data set was composed of 60 turbidity mea-

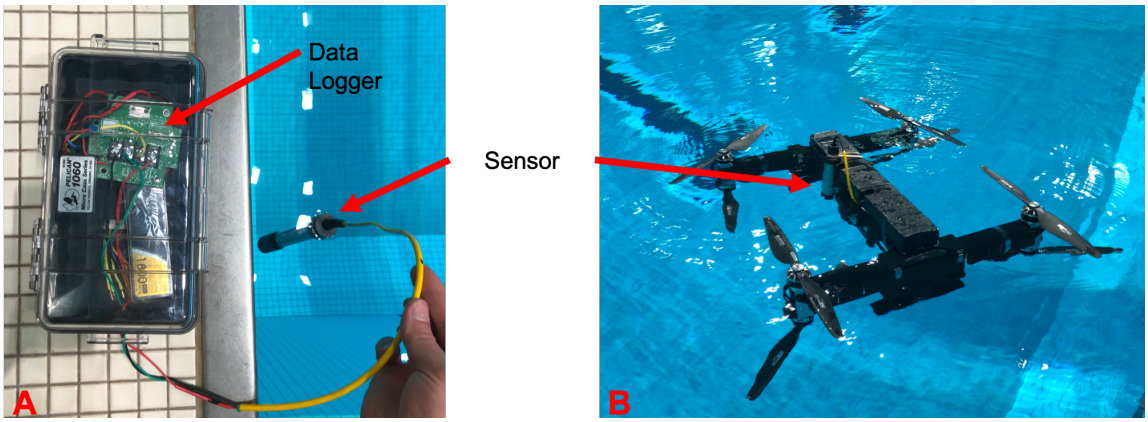

Figure 4.13: Process of retrieving turbidity data, (A) by manual means and (B), using the NV7 platform.

surements. Once all manual and multi-rotor data sets were accumulated, the measurements were averaged respectively and graphed (Figure 4.14).

Referring to the plot in Figure 4.14, one may visualize the data comparison between manually and multi-rotor achieved means. Notice, the blue plot reflects the averaged turbidity measurements retrieved by manual means while the orange plot depicts that of the NV7 retrieved data. Before submersion, the NTU measurements were at a peak of 50 NTU. Once submerged, the measurements rapidly fall to approximately 0.045 NTU. Both data sets closely follow similar readings for approximately 78 seconds. However, after the 78 second marker, the multi-rotor measurements rapidly escalate to a maximum of 0.48 NTU. Although this inconsistency is not optimal, clear factors could readily explain such anomalies. Due to its high sensitivity to light scatter and intensity, the turbidity probe is easily

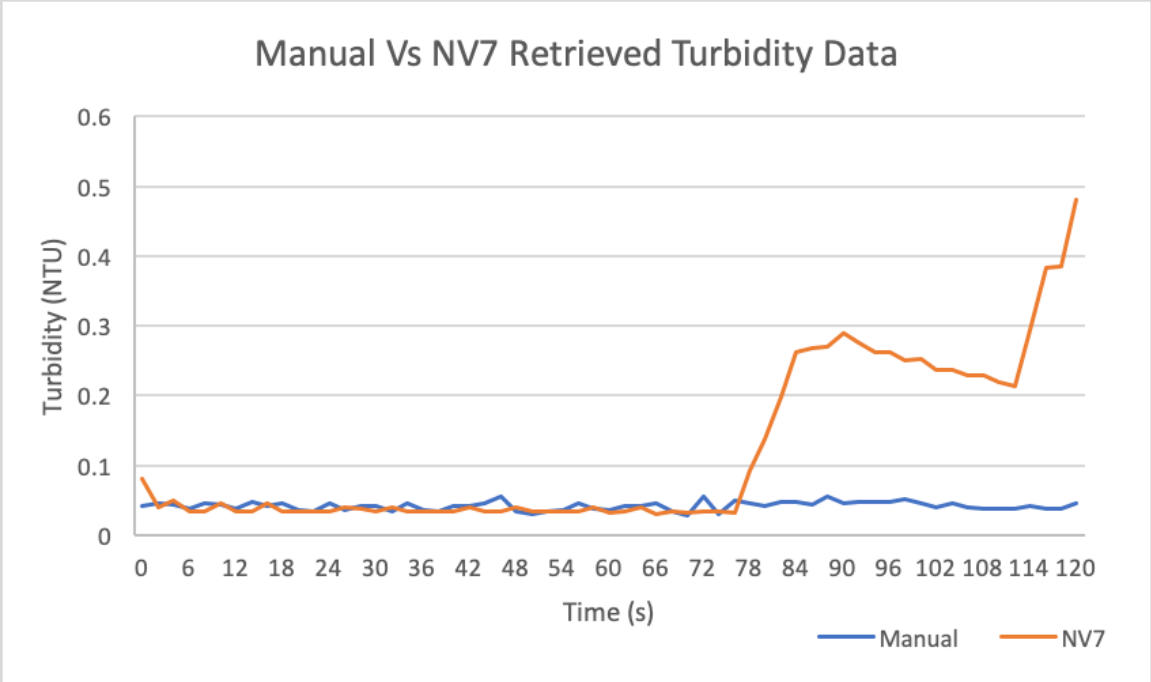

Figure 4.14: Comparison depicting the corroboration of manually and multi-rotor retrieved turbidity data.

susceptible to error. Slight alterations in probe positions will vary surrounding light intensities, leading resultant measurements to reflect inaccurate data. However, the plausible alibi for the anomalous data may be explained by the interference in light scatter. Detrimental to nephelometric turbidimeters is the presence of air bubbles. Air bubbles are notorious for erroneously diverting beam scatter and are generally the cause for instantaneous changes in measurements. In the tests performed for Figure 4.14, air bubbles could have been captured when the multi-rotor transitioned to water and after 78 seconds shifted to the beam path. Another valid proposition is that in maneuvering the NV7 to conserve the proper heading, air bubbles could have been pushed in front of the beam path. In each of these situations, such errors could be avoided by properly situating the sensor. Methods such as positioning the sensor on an angle to allow any trapped air bubbles to escape properly address the issues leading to erroneous data.

Given the close corroboration between the two methods of retrieving turbidity data, it was concluded that the NV7 platform offered a viable method of turbidity data retrieval. While there were deviations in data sets, the obvious reasons for the present discrepancies

settled any concerns regarding the adverse effects rendered by the multi-rotor. Having garnered satisfaction of the NV7 platform for the use of turbidimeter data acquisition, future testing and experimentation could be performed with confidence.

4.3.2 Dissolved Oxygen Testing

Unlike qualitative turbidity measurements, dissolved oxygen (DO) sampling is dependent on quantitative parameters. Frequently measured in percent concentration, DO is a key factor in water quality monitoring. As suggested by the Fondriest Environmental Learning Center, "dissolved oxygen is an essential factor second only to water itself" [33]. Such a claim is plausible due to the vital influence dissolved oxygen constitutes to living organisms within a body of water. While dissolved oxygen suggests the concentration of oxygen in a water sample, not all oxygen within the sample contributes to the oxygen content. Dissolved

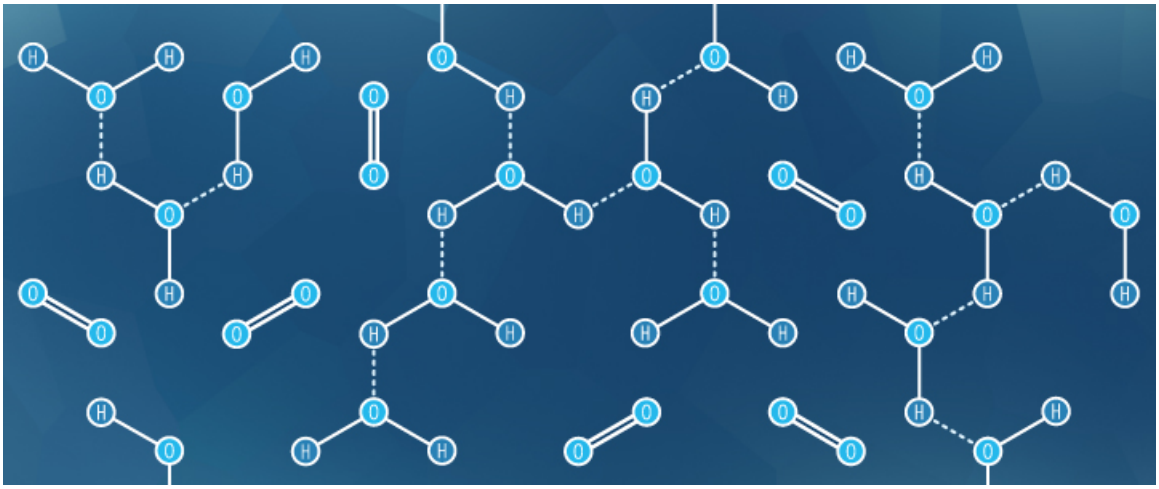

Figure 4.15: Depiction describing the makeup of a water sample. [33]

oxygen refers to the measurement of free, non-compound oxygen in a body of water. Referring to Figure 4.15, one will see that a sample of water is composed of both bonded (H2O) and free (O2) molecules. Free oxygen molecules are dispersed throughout a water sample much in the same way sugar is dissolved in water. When sampling DO measurements, only the free oxygen molecules will be taken into account.

Even though the presence of dissolved oxygen in a water sample is dependent on air/water interaction and photosynthesis, other parameters will affect the actual DO concentration of

a sample. Any factor inhibiting the engagement of air/water interaction or photosynthesis will contribute to the reduction of DO concentration. Such phenomena is recognized when visualizing DO concentrations at increasing water depth. Since air/water interactions cease with depth, the DO concentrations at greater depths are reduced. Interestingly, factors such as turbidity also reduce DO concentrations. By inhibiting sub-surface light penetration, photosynthesis is curtailed leading to reduced DO production [33].

While there are parameters affecting the concentration of DO, there are also factors which contribute to the solubility content attainable in a body of water. For this reason, just because two samples are completely saturated with DO, the actual DO content may not be equal. Factors affecting solubility include temperature, pressure and salinity. With both theoretical processes as well as experimental testing, the effects of each factor have been realized. With increasing temperatures, DO solubility decreases. For example, warm surface water will require much less DO to reach 100% oxygen saturation than deeper cold water. By increasing pressure, solubility also increases. Finally, by increasing salinity,

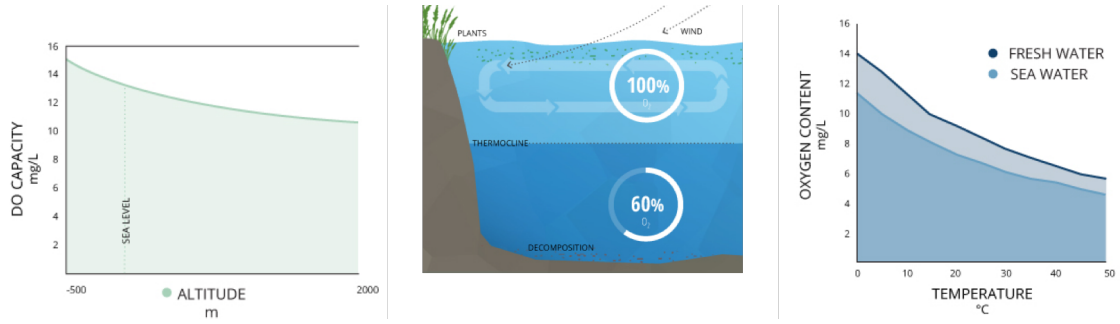

Figure 4.16: Factors affecting dissolved oxygen concentration and air solubility. [33]

solubility decreases. Referring to Figure 4.16, one may see the impact trends of sample solubility and DO concentrations. With the understanding of the above factors affecting DO concentrations, one may surmise that DO concentration will be greatest in pressurized deep cold water. However, due to the factors contributing to the actual introduction of free oxygen molecules in water, the warmer water closer to the surface will retain a greater concentration of DO. Even though deep cold water may have a greater saturation value than surface water, the factors contributing to DO do not have influence at increased depths.

Although the project at hand was not concerned with the actual meaning of the dissolved

oxygen contents in the data accumulated, it was pertinent to have an understanding of DO and its measurement methods. Knowing the importance of dissolved oxygen to limnology, DO measurements were a preferred water property to be experimented with for this project. By demonstrating the abilities of the NV7 platform to retrieve consistent DO data, it would be concluded that the project had successfully developed a viable option for future water quality monitoring missions [33].

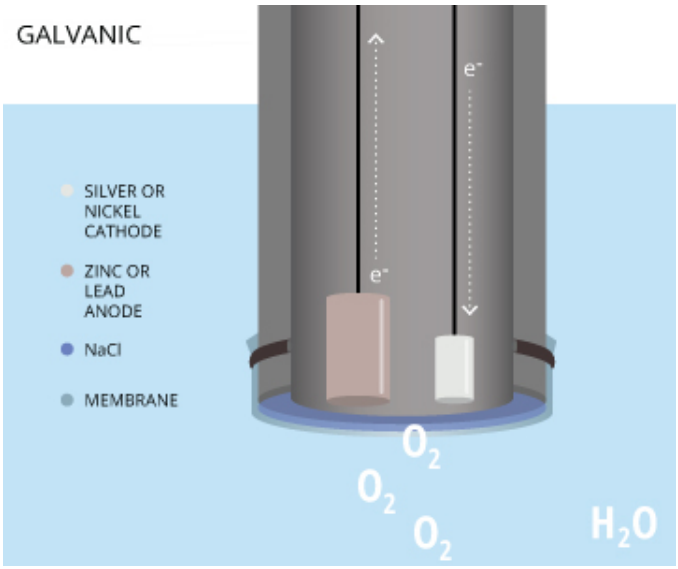

Figure 4.17: Cross-section of a galvanic dissolved oxygen sensor. [34]

For the purpose of garnering greater credibility, the dissolved oxygen sensor used for this project was the Global Water WQ401 dissolved oxygen probe. Known as a galvanic dissolved oxygen sensor, the probe utilizes an electrochemical method to generate a potential. When placed in a solution, the amount of present oxygen activates the chemical reaction and leads to corresponding potential generation. Figure 4.17 offers a rendering of a common galvanic DO sensor. Notice that one metal is the cathode and the other is the anode. The two metals are usually held in a sodium chloride solution and sealed with an oxygen permeable membrane [34].

As performed with the turbidity sensor, experiments were conducted using the dissolved oxygen probe to determine sensor reaction time. In these tests, 4 cycles were averaged and used to determine sensor settling time. In each cycle, the probe was submerged at a fix depth, sampling at a rate of one measurement every 2 seconds for approximately 340 seconds,

ref. Figure 4.18. Due to the nature of DO measurements, obtaining stable measurements

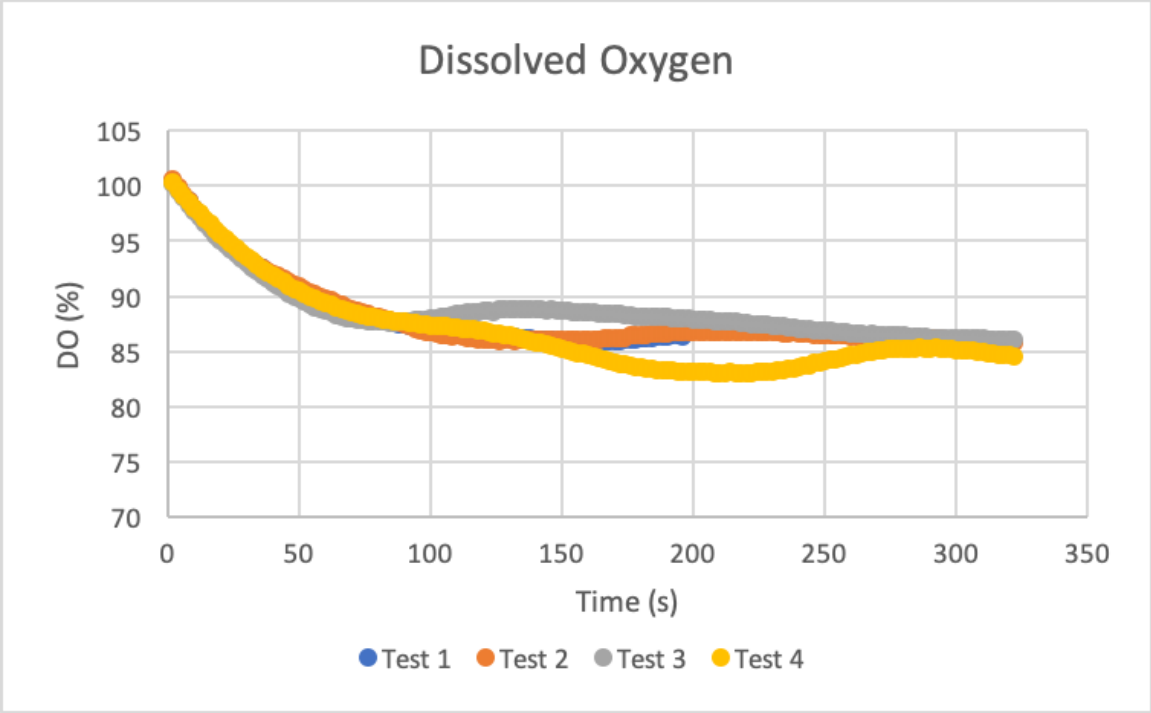

Figure 4.18: Experimental dissolved oxygen concentrations.

is challenging. Understanding the mechanics of the DO sensor allows insight as to the meaning of the data acquired. When placed in a solution, the oxygen in contact with the probe initiates a chemical reaction producing a current. If the probe is held stationary, the sensor readings will continue to decrease until the chemical reaction rate equals the diffusion rate of the present DO molecules. Measurements obtained in this method would reflect inaccurate results of an oxygen depleted microenvironment. To properly obtain DO data, the solution in contact with the probe must be continuously renewed. This phenomenon may be produced either by constantly moving the probe or stirring the solution. When data is collected in this method, the measurements will stabilize once the actual level of DO in the solution is reached. For this reason, dissolved oxygen measurements obtained using the NV7 would be inaccurate if kept stationary. To remedy this, tests were conducted ensuring constant multi-rotor movement. Following identical methods as those used to determine turbidity sensor reaction time, the dissolved oxygen probe results are displayed in Figure 4.19. As depicted in red, the sensor error provided by the sensor manufacturer was 2%. The

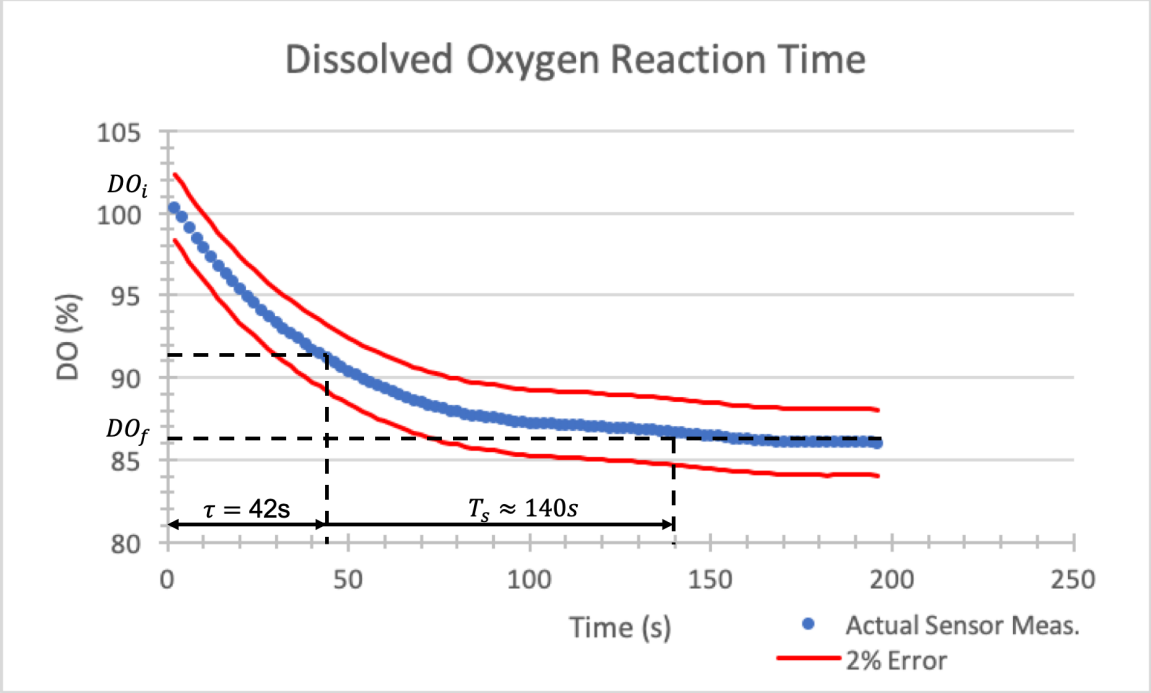

Figure 4.19: Dissolved oxygen sensor experimental reaction time.

blue data points reflect the sensor measurements from time 0 to time 200. After analysis, it was found that the sensor settling time was 140s while tau was 42s. Prone to lengthy settling times, such sensors as the dissolved oxygen probe pose challenges for mobile measurements. Experiments conducted in which the NV7 would continuously maneuver from location to location would not reflect spacio-temporally accurate data. However, such experiments would still provide average DO concentrations throughout a region and indicate areas of varying quantities. In subsequent tests, actual experiments were conducted in which the NV7 continuously sampled designated pool regions.

To demonstrate the viability of the NV7 platform for DO data acquisition, subsequent tests were performed to compare both manual and remotely obtained data. Much like the tests performed with the turbidity sensor, 5 two-minute manual tests were conducted as well as 5 two-minute multi-rotor tests. Once the data was obtained, both the manual and multi-rotor tests were averaged and graphed. As depicted in Figure 4.20, a typical dissolved oxygen plot begins at approximately 100% concentration and descends to the oxygen concentration value present in the tested sample. Whereas turbidity measurements quickly drop to the

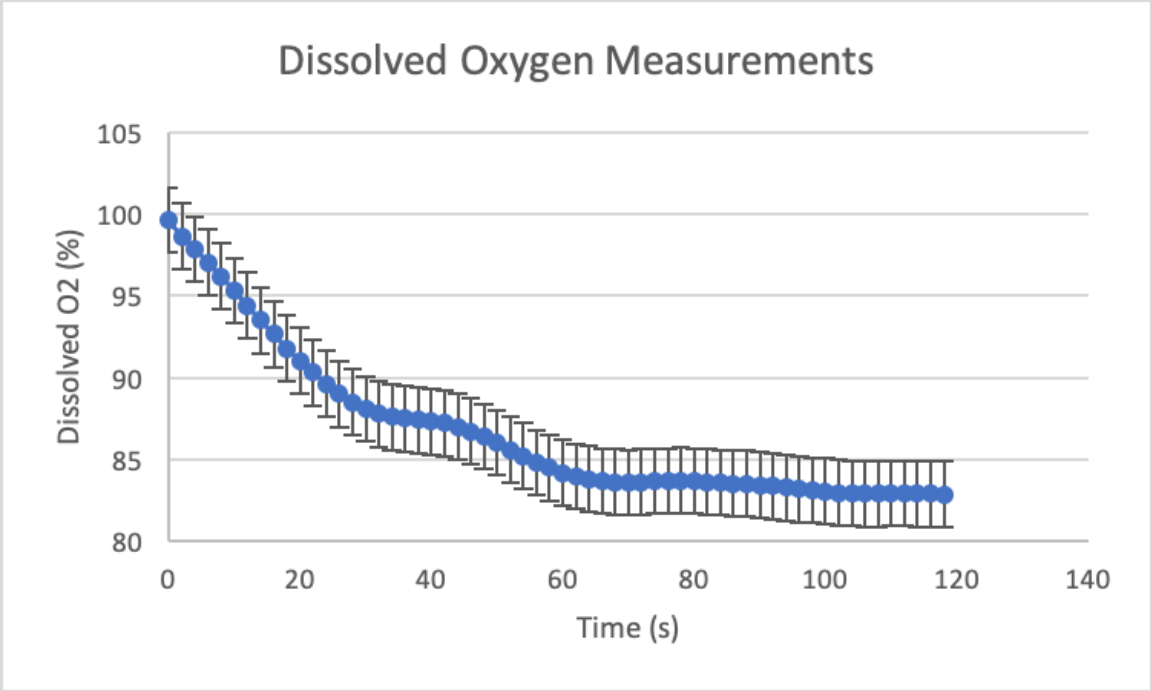

Figure 4.20: Sample dissolved oxygen measurements accumulated over the course of 120 seconds. Measurements were taken once every 2 seconds.

measured value, DO measurements tend to take approximately 30 to 60 seconds to settle. Given the varying amount of DO in contact with the probe at all times, there will be constant slight fluctuations in measurement readings. Although measured as a percent concentration, using specialized tables, one may determine the volume of free oxygen within a sample.

Referring to Figure 4.21, one may see the comparison between the manually and remotely retrieved dissolved oxygen data. Each plot begins at about 100% and over the course of 40 and 60 seconds respectively, reach a more constant low concentration. In the plot, the blue marker corresponds to the data retrieved manually while the orange marker corresponds to the data retrieved using the NV7 platform. While both data sets follow a fairly constant curve for the first 40 seconds, they do have a distinct shift in measurements once they reach their minimum point. At 40 seconds, the manually retrieved data has reached its lowest point. However, because the lowest measurements for the NV7 retrieved data are below that of the manually retrieved data, the curve only reaches its low point at about 60 seconds. When analyzing the measurements, one must consider all factors affecting the

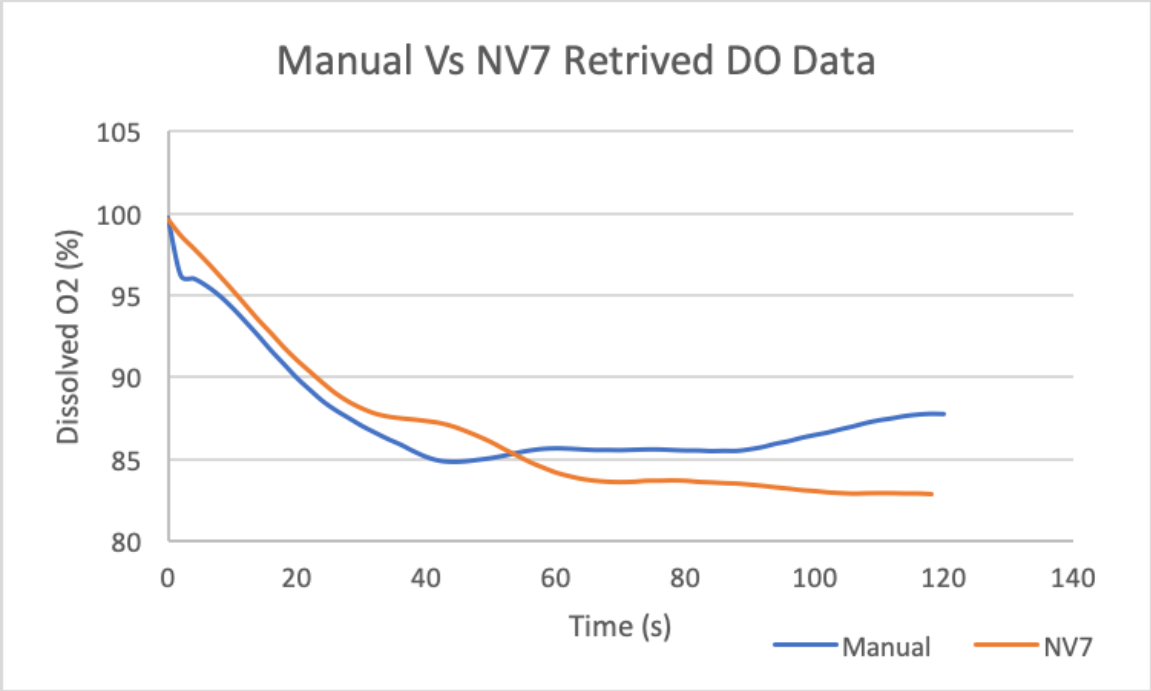

Figure 4.21: Comparison depicting the corroboration of manually and multi-rotor retrieved dissolved oxygen data.

presented data. Although concerns could be developed due to the approximate 3% change between the two data sets, adequate reasoning may assuage them. When the data was being recorded, the hand held data was obtained by allowing the tip of the probe to rest in the water. However, when experimenting with the NV7, the probe was completely submerged. In this manner, the depth change from manually to remotely retrieved data was at minimal, one foot. While not a great difference, one must remember that with increased depth, dissolved oxygen concentration will decline. According to the authors of [33], for every meter in increased depth, there is a 10% decrease in DO concentration. Converting meters to feet, 1 ft corresponds to a 3.05% decrease in DO content. This reasoning explains the approximate 3% change in data sets. Once again, after evaluating the dissolved oxygen measurements and visualizing the corroboration of the data sets, it was concluded the NV7 platform provided a viable method for retrieving consistent DO data.

To compute the actual DO volume (mg/L) according to the data in Figure 4.21, the use of of several factors and the table presented in Figure 4.22 must be used. The factors

TEMPERATURE (°C)	SALINITY (g/kg)								
	0	5	10	15	20	25	30	35	40
28	7.827	7.613	7.404	7.201	7.003	6.810	6.623	6.441	6.263
29	7.691	7.482	7.278	7.079	6.886	6.698	6.515	6.337	6.164
30	7.558	7.354	7.155	6.961	6.772	6.589	6.410	6.236	6.066
31	7.430	7.230	7.036	6.846	6.662	6.483	6.308	6.137	5.972

Figure 4.22: Table containing listings of DO volume according to temperature and salinity. [33]

that must be known are the sample's temperature and salinity as well as the pressure. The pressure was already accounted for by the probe when taking measurements. Since the experiments were conducted in the Werblin diving well on the Rutgers University New Brunswick campus, pool temperature was determined to be 29 degrees Celsius according to: [35]. As related by the authors of [36], fresh water salinity is almost zero parts per thousand (PPT). With the required information complete, the actual dissolved oxygen content may be computed by using equation 4.1.

$$O2\ mg/L = (Measured\ \%DO)\ x\ [DO\ Chart\ Value] \tag{4.1}$$

Accordingly, a dissolved oxygen concentration of 82% would correspond to a volume of 6.306 mg/L. To apply such a value to a real life scenario, the oxygen supply would be ample to support most fresh water fish [33]. However, since the quality of water is never dependent on one factor alone, the pool water analyzed having sufficient oxygen does not mean it is fit for aquatic life. As a beginning, one may see how the process of determining the quality of a body of water is determined.

To demonstrate the ability of the NV7 system to continuously gather data throughout a region, final tests were performed both indoors and outdoors. In the preliminary mission, the NV7 maneuvered over the Rutgers patio pool while dragging the DO sensor. Beginning on the left hand side of the pool, the NV7 flew in a straight path from one side of the pool and back. Once the path was completed, the multi-rotor shifted approximately 4 feet to the right and repeated the flight pattern. This method was repeated until the entire pool was monitored. The results of these tests are presented in Figure 4.23. While the plots closely resemble each other, the actual quality of the data is subject to error due to the slow

reaction time of the DO sensor. To gain more accuracy, experiments would need to allow longer wait times at each location. While not accurate, Figure 4.23 demonstrates the ability of the NV7 system to acquire spatio-temporal data remotely.

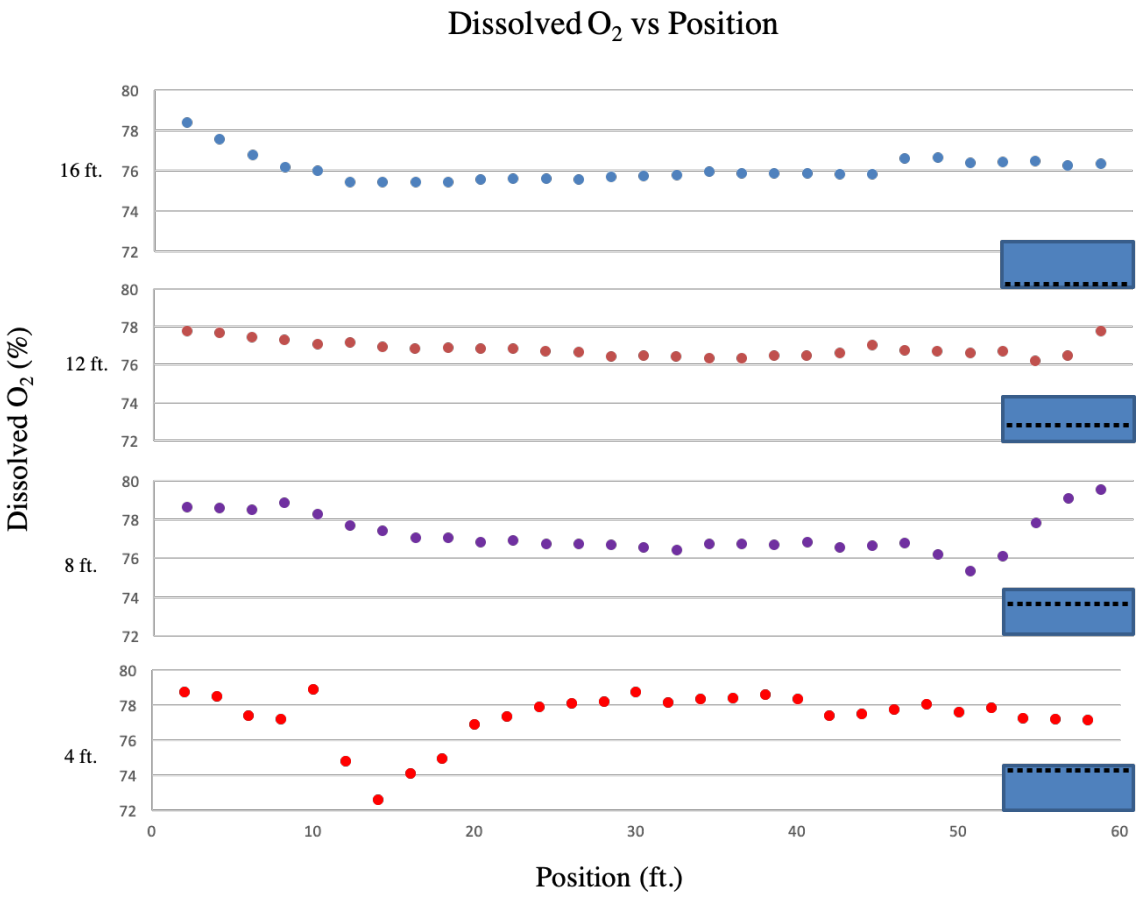

Figure 4.23: Dissolved oxygen concentration throughout the Rutgers patio pool.

4.4 Rutgers Marine Field Station Testing

As a final experiment, testing was conducted using the NV7 to showcase its ability to retrieve salient data from an outdoor location in a timely and effective manner. The testing was conducted at the Rutgers Marine Field Station in south east New Jersey.

For this experiment, the NV7 was equipped with a custom built sensor package composed of a conductivity sensor, a dissolved oxygen sensor and a Raspberry pi. The two sensors were chosen for there lightweight construction and affordable cost. The Raspberry pi was selected

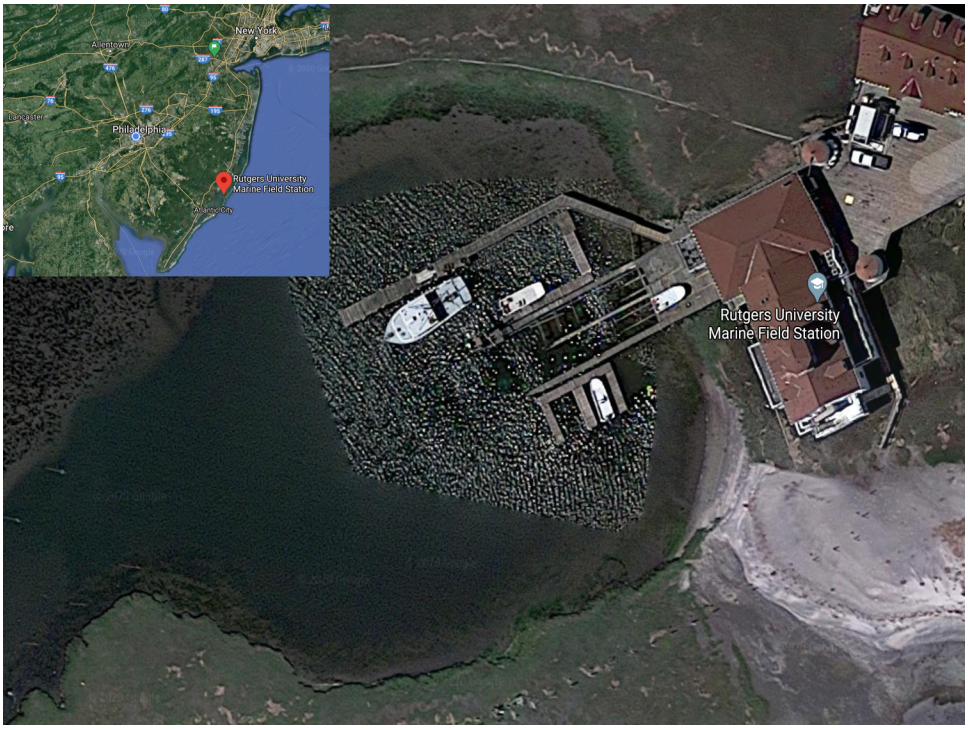

Figure 4.24: Rutgers University Marine Field Station (RUMFS). Data collection site for the following experiments.

for its wireless logging ability as well as its processing capabilities. Referring to Figure 4.25, one may see the experimental process explained. To gain a 3-dimensional understanding of the Rutgers University Marine Field Station (RUMFS) cove water construct, the following experiment was conducted three times. All factors were held constant for each experiment except sampling depth. The initial experiment sampled a one foot subsurface plane while experiments two and three sampled at depths of two and three feet respectively.

Flying from the dock, the multi-rotor was piloted to each location represented by an orange circle. Beginning with the right uppermost location, the multi-rotor continued sampling data in a lawnmower pattern made up of 20 sampling locations 10 feet apart. At each location, the NV7 transitioned to water and sampled data for 60 seconds. With a sampling rate of one measurement every two seconds, a total of 30 samples were collected at each location. Once the initial experiment was completed, 20 locations had been sampled at a depth of one foot. Using the acquired data and post processing, plots were generated depicting the overall water construct for a 10 x 50 foot area at a depth of one foot, two feet

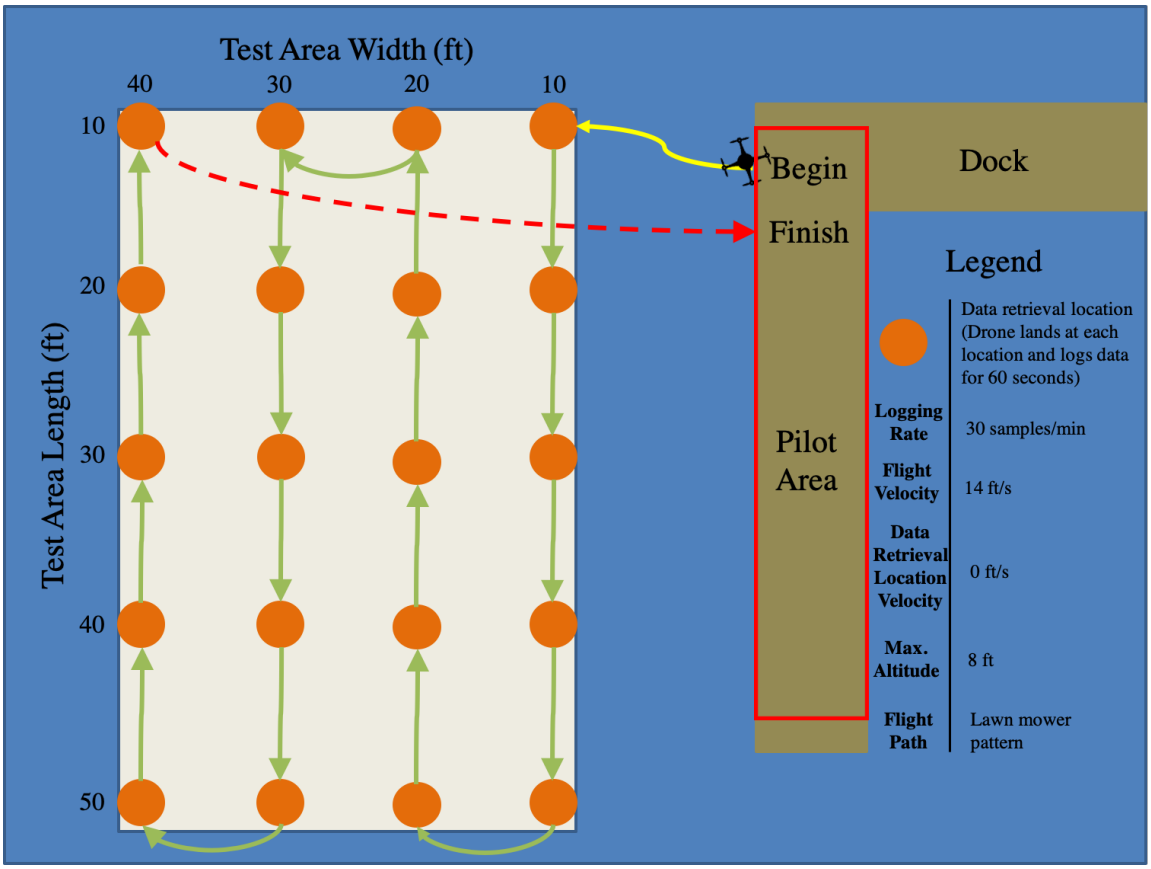

Figure 4.25: Diagram depicting flight path and technical specifications for the experiments conducted at RUMFS.

and three feet.

In the following plots, the data collected is displayed in various methods to assist the reader in visualizing the interpretation of the measurements. As was previously suggested, accumulating multiple data samples from multiple depths allows one to recognize shifting water characteristics in three dimensions. This three dimensional construct is depicted in Figure 4.26.

4.4.1 Conductivity Data Analysis

The first plot presented is that of the marine cove conductivity content. Hydro conductivity is a measure of a body's ability to conduct electrical current. The sensor used for the experiment was a common inexpensive probe. The probe offered an output of micro-Siemens

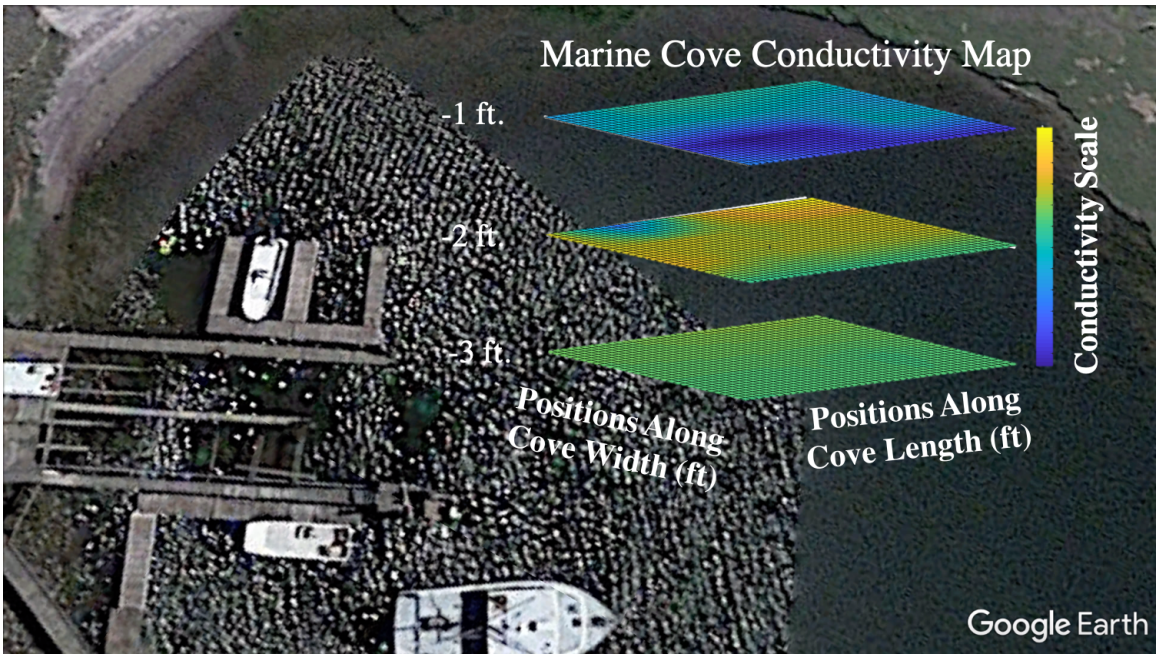

Figure 4.26: Overlay of actual data collected at multiple depths on the actual testing site.

per cm; a common measurement used for quantifying conductivity. In Figure 4.27 the marine cove conductivity is presented at three depths as indicated by the left z-axis. On the right z-axis, a color scale is supplied for quantifying the corresponding levels of conductivity present in the three heat-map plots. The length and width labels correspond to the dimensions of the sampling test areas. While not pictured in this plot, samples were taken at every 10 feet along the width and 10 feet along the length of the test area up to 40 and 50 feet respectively. Referencing the color scale, it can be seen that samples retrieved at -1 foot tended to be the least conductive followed by the -3 foot samples and culminating with the highest conductive measurements at -2 feet.

Typically, water bodies are composed of uniform conductivity concentrations. However, due to its unique location on a side channel adjacent to an estuary opening into the Atlantic Ocean, the marine cove experienced intriguing fresh and saltwater interactions with tidal currents. While purified water is naturally an electrical insulator, saline water is notorious for high conductivity. As the experiments conducted were performed during an increasing tidal period, the data collected reflected new fresh and saltwater interaction phenomena. As saltwater mixes with freshwater, it advances in a wedge shape form as pictured in Figure

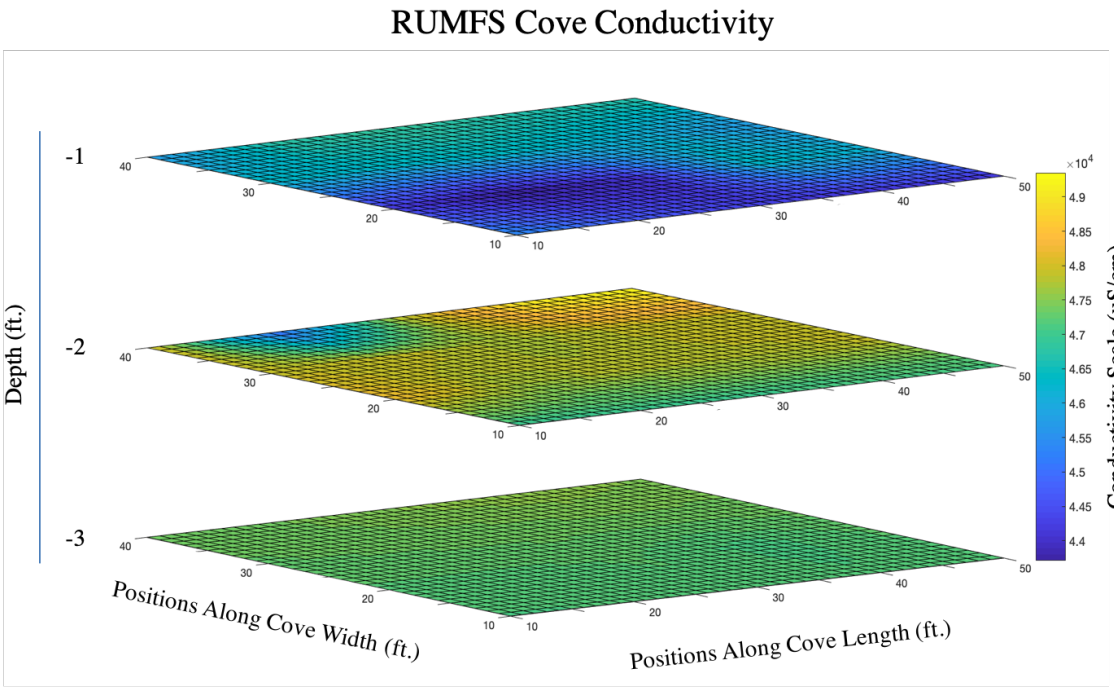

Figure 4.27: Three-dimensional construct demonstrating conductivity trends at three different depths.

4.28. Due to its greater density, the saltwater mass slowly mixes with the brackish lower layer of water while the freshwater from the upstream estuary rises to the surface. In this fashion, the cove experiences stratification consisting of various salinity values. Following Figure 4.27 one may see that the color patterns follow similar logic to that of the cove stratification. At the surface, the freshwater corresponds to a low conductivity, the saltwater mass corresponds to a high conductivity, and finally, the bottom region of brackish water corresponds to a medium level conductivity area. To more clearly visualize the comparison between each surface plot, one may refer to the plots positioned side by side in Figure 4.29. Here again, each plot corresponds to samples taken at each depth beginning with -1 foot on the left and culminating with -3 feet on the right.

Figure 4.30 depicts the actual conductivity values of each sampled location. Utilizing this plot, one may see actual conductivity values clearly, as well as the uncertainty of the data acquired. In Figure 4.30, conductivity values are represented on the primary y-axis, width positions are denoted on the secondary y-axis, and length positions are displayed on

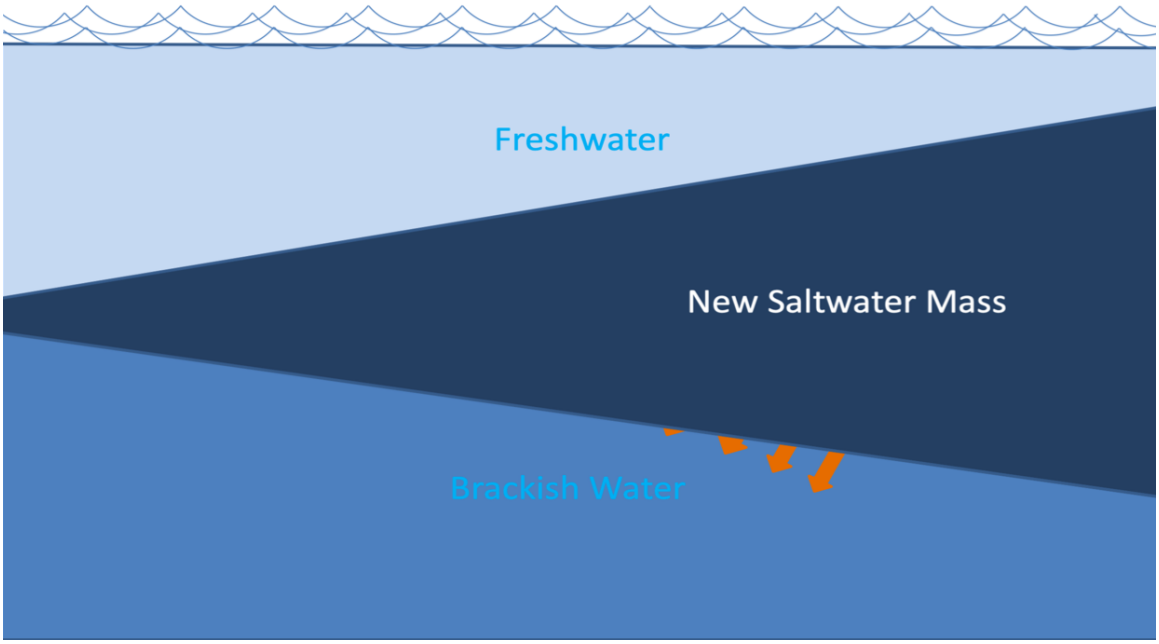

Figure 4.28: Interaction between freshwater and saltwater causing stratification.

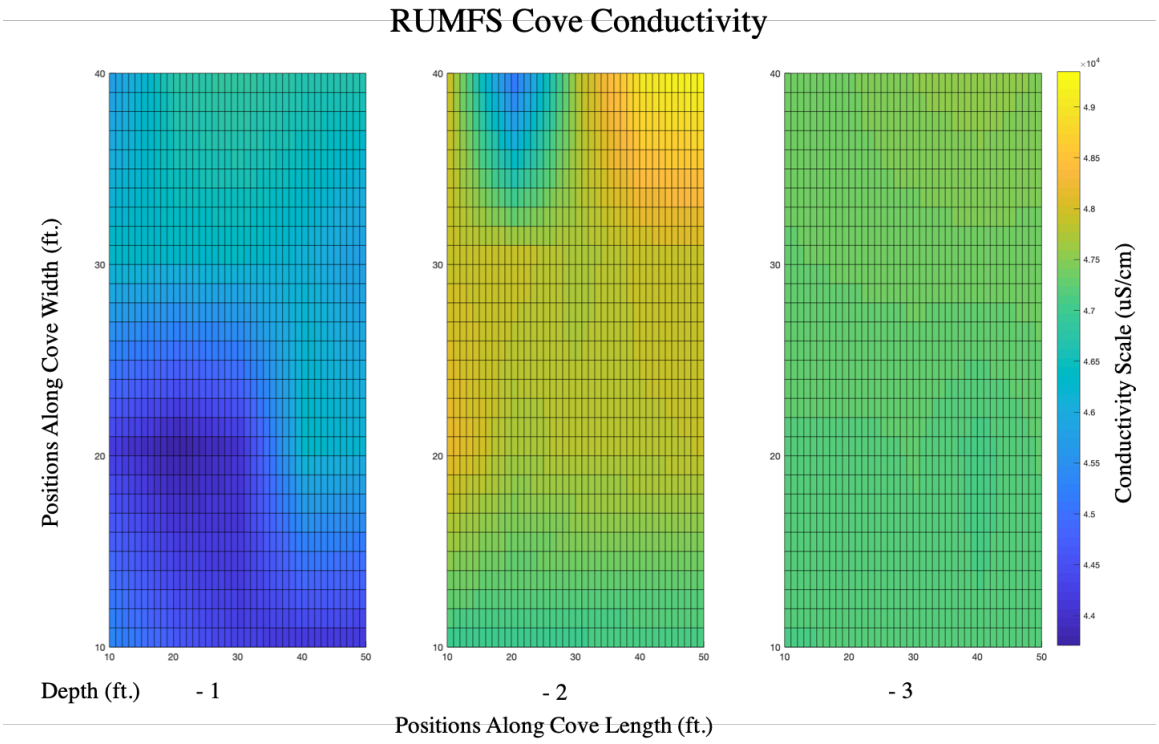

Figure 4.29: Side by side conductivity comparisons at -1, -2, and -3 feet.

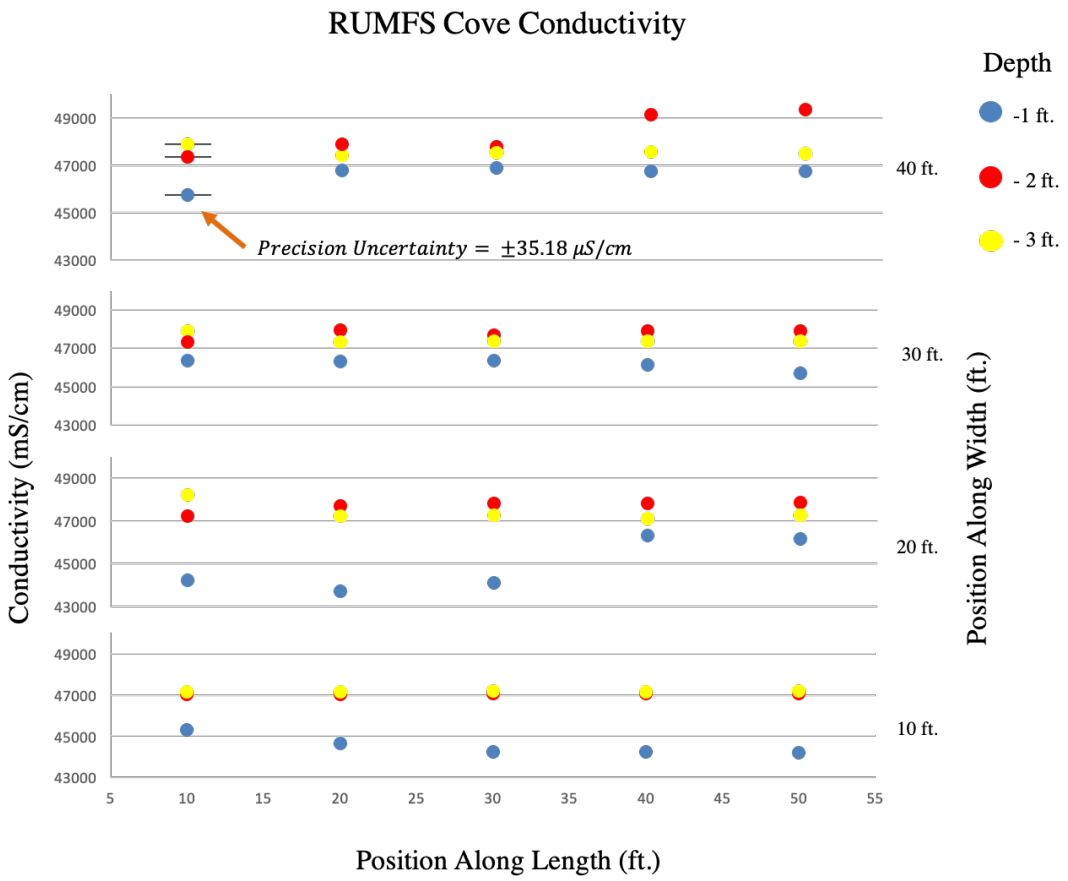

Figure 4.30: Scatter plot depicting quantitative conductivity measurements at multiple depths with precision uncertainty.

the x-axis. The three color types correspond to different sampling depths. Blue corresponds to -1 foot, red to -2 feet, and yellow to -3 feet. In combined form, these data sets offer a quantitative trend corresponding to different water depths. In each location presented, the general trend reflects low conductivity on the 1 foot volume, high conductivity on the 2 foot volume and medium on the 3 foot volume.

The error bars depicted on the upper left data set correspond to the precision uncertainty level of the collected data. By performing simple calculations to determine standard deviation and variance, it was determined all data points could be found within +/- 35.18 microSiemens/cm of the mean measurement with a confidence interval of 95%. Such an interval is very small when compared to the measurement values which range between 43,000 and 49,000 microSiemens/cm. Because of the small uncertainty, the data presented suggests

that the claims of water stratification explained above are accurate.

4.4.2 Dissolved Oxygen Data Analysis

While collecting conductivity measurements, dissolved oxygen measurements were collected simultaneously. Each of the following plots depict similar analysis as was performed with that of the conductivity figures. All dissolved oxygen data was collected in the same fashion in which the conductivity samples were retrieved, greatly reducing the time taken for the experiment sampling sessions. Similar to the conductivity plot, in Figure 4.31, the primary

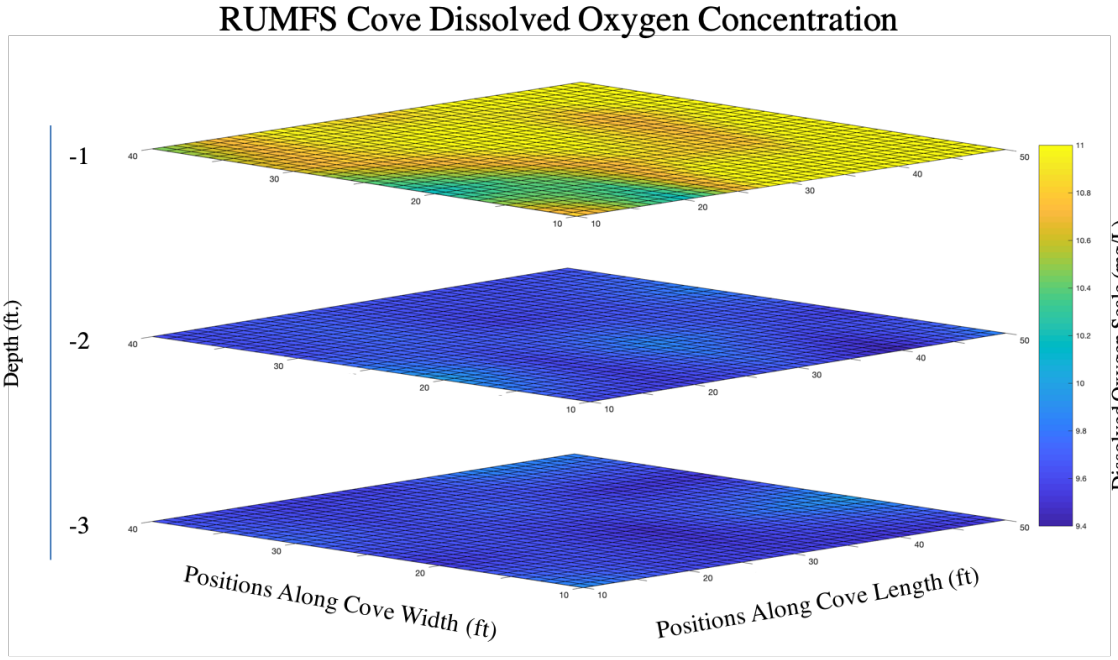

Figure 4.31: Three-dimensional construct demonstrating dissolved oxygen trends at three different depths.

left z-axis corresponds to varying depths from -1 to -3 feet while the right z-axis consists of a dissolved oxygen color bar scale in mg/L. Both horizontal axes correspond to the length and width of the test area at the RUMFS cove. As can be interpreted from the plot, the dissolved oxygen content is high at the -1 foot marker and relatively constant between -2 and -3 foot sampling regimes. Once again, this trend may be explained by the estuary and tidal currents present in the cove.

During high tide, saltwater makes its way into the cove and settles more toward the

bottom of the pool. In this stratified state, fresher water will surface, causing a relatively thin layer of highly oxygenated water. Another reason for increased oxygen contents at the surface is that of wind and water interactions. In windy conditions, oxygen is forced into the upper water surface thereby enriching it with dissolved oxygen. Clearly, the combination of wind/water interaction and increased freshwater oxygen levels is reflected in Figure 4.31 at a depth of -1 foot. As one descends below the first foot of water, the oxygen content decreases and shifts very little between -2 and -3 feet. In addition to naturally lower oxygen concentrations, the saltwater entering the cove drifts toward the inlets bottom. However, a secondary cause of decreased oxygen content is that of increasing depth. As discussed beforehand, a key factor influencing dissolved oxygen concentrations is that of increasing depth. With increased pressure, the dissolved oxygen surfaces and leaves deeper depths with minimal oxygen.

Figure 4.32 offers a two dimensional view of the three depths measurements side by side. As with the conductivity plot, the primary y-axis corresponds to sample area width,

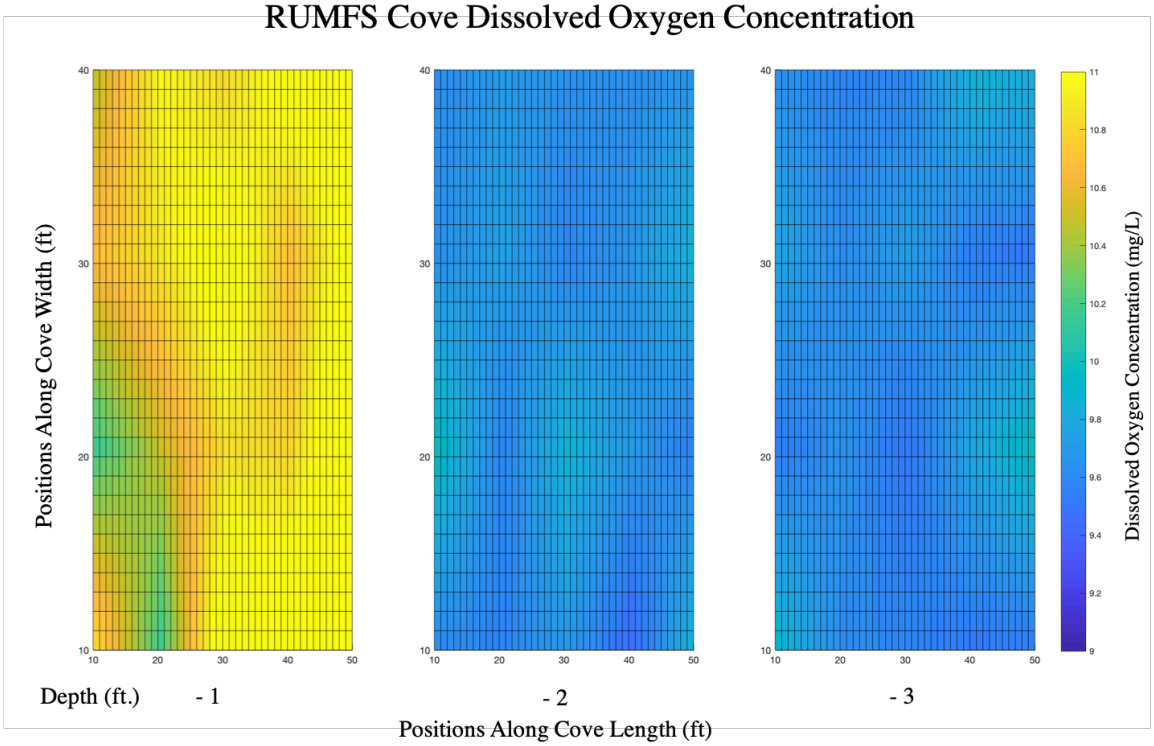

Figure 4.32: Side by side conductivity comparisons at -1, -2, and -3 feet.

the primary x-axis corresponds to sample area length, the secondary y-axis corresponds to dissolved oxygen levels, and the secondary x-axis corresponds to depth measurement locals.

Finally, to realize the actual quantitative dissolved oxygen results, Figure 4.33 offers a scatter plot of the compiled measurements. As previously related, the three data point colors

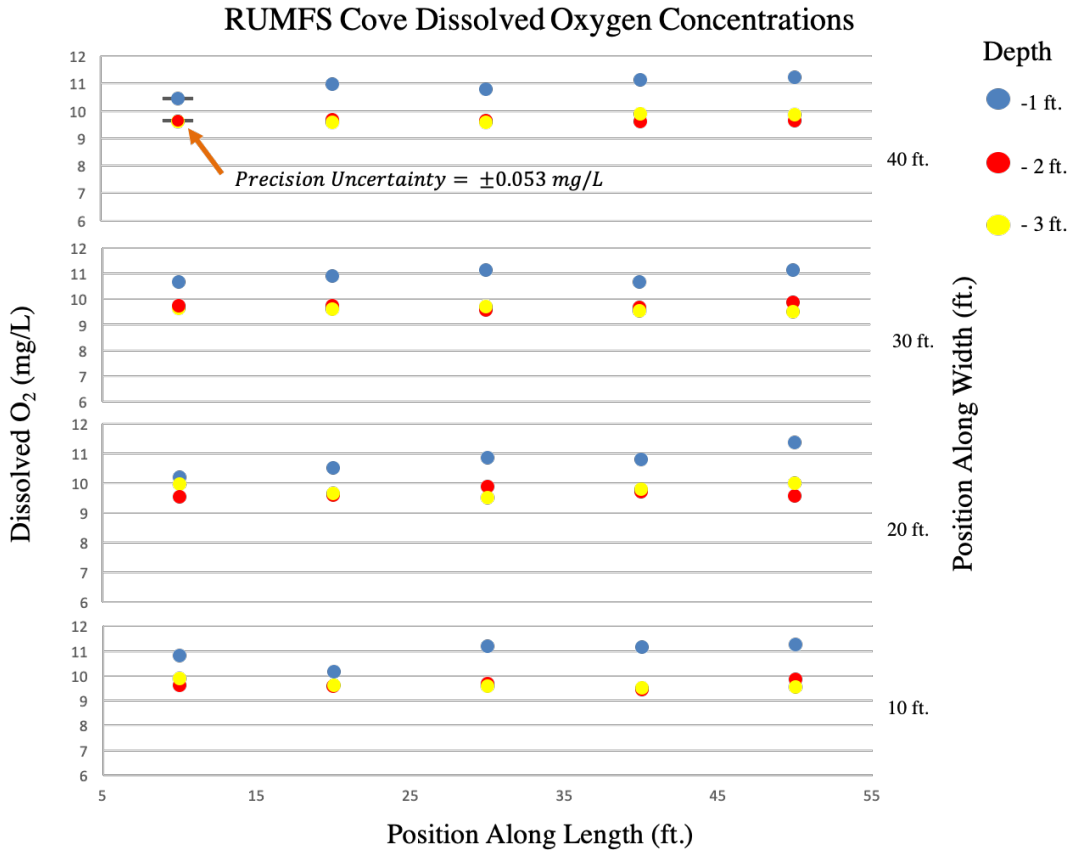

Figure 4.33: Scatter plot depicting quantitative conductivity measurements at multiple depths with precision uncertainty.

correspond to samples taken at 1, 2, and 3 feet sub-surface. The primary y-axis denotes the oxygen concentrations sampled in mg/L while the secondary y-axis and x-axis delineate the width and length of the test area in feet respectively. As can be traced throughout the plot, the 1 foot subsurface samples consistently posses increased dissolved oxygen contents when compared to -2 and -3 foot samples.

To quantify the the uncertainty of the data presented, calculations were performed to determine the precision uncertainty spread for a 95% confidence interval. As depicted in

Figure 4.33, the upper left data points contain error bars denoting a final precision uncertainty interval of only +/- 0.05 mg/L. Once again, with such a small precision interval, the above related reasons for the dissolved oxygen measurements are supported.

While both the conductivity and dissolved oxygen data presented demonstrated high precision, the accuracy of the measurements was not addressed. When performing these measurements at the RUMFS, various measurements were collected using a biologists high end conductivity/dissolved oxygen probe. Using these measurements as a standard, the data collected on with the NV7 was compared and the accuracy evaluated. While closely resembling the measurements of the standard, the results of the calculations are included in the appendix section of this thesis and were integrated into the thesis presentation.

With the culmination of the tests displaying the performance of the NV7 in various outdoor regions as well as in water data acquisition experiments, it was deemed a formidable method in which to conduct water monitoring missions. Subsequent tests demonstrated the NV7's ability to gather data over greater areas of interest. As reflected in Fig4.34,

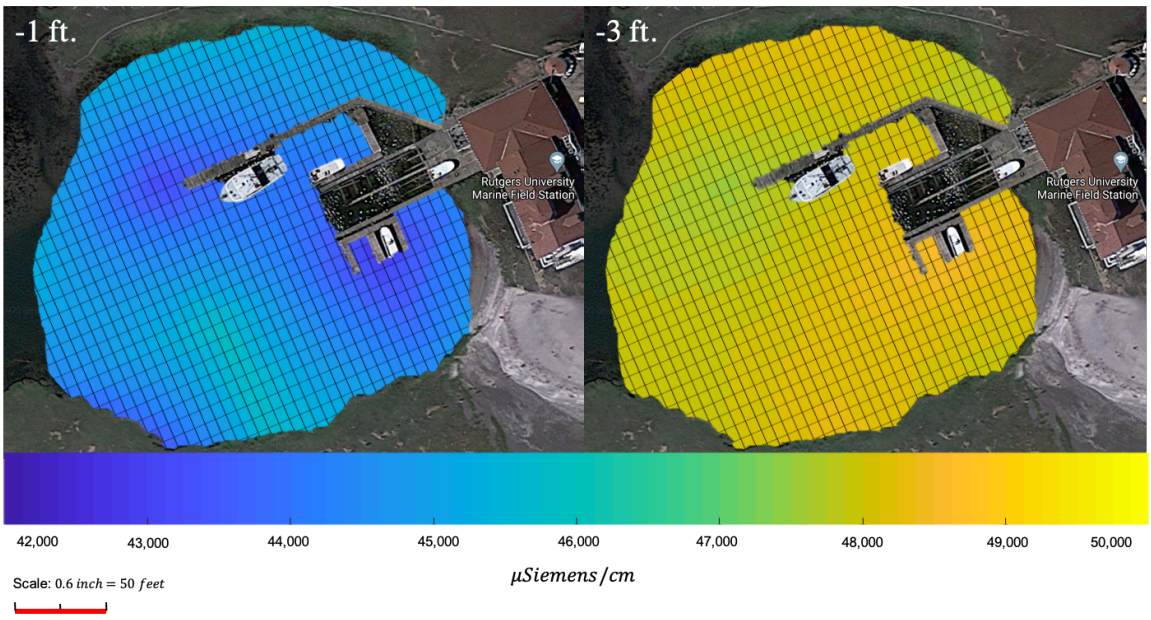

Figure 4.34: Full RUMFS Cove conductivity mapping using the NV7 platform. Just one example of the numerous applications of such a system.

the NV7 platform was used to map the entire RUMFS cove. Such a demonstration is an example of the many uses of the system. Ongoing research has been performed in

which the NV7 has conducted collaborative water monitoring missions with a Blue Robotics ROV. Future experiments are planned to enhance and expedite methods of acquiring data. With the progression of continued testing, the intent of the final goal would be to develop a completely autonomous platform consisting of multiple heterogeneous vehicles for the purpose of collecting salient hydro-data in a safe and streamlined manner. While much still needs to be done, this project has set the groundwork and displayed both the potential and feasibility for such a mission.

Chapter 5

Conclusions

Although the idea and creation of the Naviatior multi-rotor existed before the design of the NV7, it was advantageous to tailor a vehicle to the requirements of this project. Improving on past experiences, the NV7 was engineered to minimize cost, fabrication time and maintenance while designed specifically for aiding in water quality monitoring missions.

In the beginning of this work, efforts were made to offer a comprehensive view of the development of multi-rotors and their applications. Further discussions related the current methods in which water monitoring is performed. Pointing to the potential dangers and shortcomings inherent to the current methods, a solution was proposed in which a fully amphibious multi-rotor would replace humans for certain tasks. In subsequent sections, the inspiration for and development of the Naviator multi-rotor was related. Acting upon proposal, the project continued with the customization of a Naviator for the purpose of water monitoring. With an extensive overview of the design of a multi-rotor for said missions, the culminating product was the development of the Naviator Version 7.

Finally, with the development of the NV7, it was advantageous to demonstrate its performance as a Naviator and its viability as a remote platform for hydro data acquisition. To constitute credibility, extensive testing was conducted to evaluate the behavior of the multi-rotor in both controlled settings as well as harsh outdoor environments. Once the platform garnered credibility as a Naviator, subsequent testing was performed to demonstrate its capabilities in acquiring water data. Consequent tests consisted in comparing manually acquired data to that obtained using the NV7 system. Once it was demonstrated that the data sets corroborated, the NV7 was deemed viable for continued hydro data acquisition missions.

Although not included in this work, continued experiments are being conducted to optimize and streamline hydro missions using the NV7 platform. With a vision to automate the process of water monitoring, continued and future experiments aim to demonstrate the potential and feasibility of such a mission.

References

[1] Wang, Qiang. "The Current Research Status and Prospect of Multi-rotor UAV." Journal of Mechanical and Civil Engineering 14.4 (2017): 31-35.

[2] Giones, Ferran, and Alexander Brem. "From toys to tools: The co-evolution of technological and entrepreneurial developments in the drone industry." Business Horizons 60.6 (2017): 875-884.

[3] Johnson-Laird, Philip N. "Flying bicycles: How the Wright brothers invented the airplane." Mind and Society 4.1 (2005): 27-48.

[4] Nikola, Tesla. "Method of aerial transportation." U.S. Patent No. 1,655,113. 3 Jan. 1928.

[5] Soni, Parth V. Characterization and optimization of UAV power system for aerial and submersible multi-medium multirotor vehicle. Diss. Rutgers University-Graduate School-New Brunswick, 2016.

[6] C. Jefford, The RAF Harrier Story, London: Royal Air Force Historical Society, 2006.

[7] Bramlette, Richard B., and Ronald M. Barrett-Gonzalez. "Design and Flight Testing of a Convertible Quadcopter for Maximum Flight Speed." 55th AIAA Aerospace Sciences Meeting. 2017.

[8] “Connecting and nbsp;Everything for Arducopter.” Arduino Based Arducopter UAV, the Open Source Multi-Rotor, www.arducopter.co.uk/all-arducopter-guides/2connectingeverything-for-arducopter.

[9] Maisel, Martin D., Demo J. Giulianetti, and Daniel C. Dugan. "The history of the XV-15 tilt rotor research aircraft: from concept to flight." (2000).

[10] A. Gibiansky, "Quadcopter Dynamics, Simulation, and Control,"2010. [Online]. Available: `https:www.researchgate.net/post/Does_anyone_know_about_the_first_order_function_of_the_brushless_motor_of_quadrotor#view=560c1e485f7f7136b78b45fc`

[11] a. C. A. B. Kunzmann Juergen, "Investigations in the control of a four-rotor aerial robot," in Proceedings of the 2nd IASTED International Conference on Robotics (ROBO 2011),Pittsburgh, 2011.

[12] Ebeid, Emad, Martin Skriver, and Jie Jin. "A survey on open-source flight control platforms of unmanned aerial vehicle." 2017 Euromicro Conference on Digital System Design (DSD). IEEE, 2017.

[13] F. Pasolini, "MEMS Accelerometers, Gyroscopes, and Geomagnetic Sensors - Propelling Disruptive Consumer Applications," Digi-Key, 2011. [Online]. Available: [Accessed 2019]

[14] C. Mathas, "Sensor Fusion: The Basics," Digi-Key, 2012. [Online]. Available: http://www.digikey.com/en/articles/techzone/2012/apr/sensor-fusion-the-basics.[Accessed 2016].

[15] Bilgen , Onur, and Thomas Alberts. “Multi-Rotor Basics.” Drone Fundamentals. Mechanical and Aerospace Engineering, 2019, Rutgers University, Rutgers University.

[16] University of Waterloo Aerial Robotics Group. “PID Loops.” PID Loops - WARG Docs, www.docs.uwarg.com/picpilot/pid-loops/.

[17] T. G. Wilson and P. H. Trickey. “D-C machine with solid-state commutation”. In: IEEE 81.11 (1962), pp. 879–884.

[18] Green, Clayton R., and Robert A. McDonald. "Modeling and Test of the Efficiency of Electronic Speed Controllers for Brushless DC Motors." 15th AIAA Aviation Technology, Integration, and Operations Conference. 2015.

[19] srl, JAES. “Jaes Srl - Japan American European Solutions - Home Page.” Jaes Srl - Japan American European Solutions - Home Page, jaescompany.com/.

[20] Marques, F., Lourenço, A., Mendonça, R., Pinto, E., Rodrigues, P., Santana, P., & Barata, J. (2015, May). A critical survey on marsupial robotic teams for environmental monitoring of water bodies. In OCEANS 2015-Genova (pp. 1-6). IEEE.

[21] E. Pinto, F. Marques, R. Mendonc¸a, A. Lourenc¸o, P. Santana, and J. Barata, “An autonomous surface-aerial marsupial robotic team for riverine environmental monitoring: Benefiting from coordinated aerial, underwater, and surface level perception,” in Proc. of the IEEE International Conference on Robotics and Biomimetics (ROBIO). IEEE, 2014.

[22] Rodrigues, P., Marques, F., Pinto, E., Pombeiro, R., Lourenço, A., Mendonça, R., ... & Barata, J. (2015, October). An open-source watertight unmanned aerial vehicle for water quality monitoring. In OCEANS 2015-MTS/IEEE Washington (pp. 1-6). IEEE.

[23] Rival, D., Prangemeier, T. and Cameron Tropea. "The influence of airfoil kinematics on the formation of leading-edge vortices in bio-inspired flight." Animal Locomotion. Springer, Berlin, Heidelberg, 2010. 261-271.

[24] Maia, M. M., Soni, P., and Diez, F. J. (2015). Demonstration of an aerial and submersible vehicle capable of flight and underwater navigation with seamless air-water transition. arXiv preprint arXiv:1507.01932.

[25] “The-Naviator.” The Naviator, thenaviator.com/the-naviator.

[26] Maia, M. M., Mercado, D. A., and Diez, F. J. (2017, September). Design and implementation of multirotor aerial-underwater vehicles with experimental results. In 2017 IEEE/RSJ International Conference on Intelligent Robots and Systems (IROS) (pp. 961-966). IEEE.

[27] “KDE3510XF-715 Brushless Motor for Electric Multi-Rotor (SUAS) Series.” KDE Direct, www.kdedirect.com/products/kde3510xf-715.

[28] Holzsager, J. E. (2017). The effects of coaxial propellers for the propulsion of multirotor systems (Doctoral dissertation, Rutgers University-School of Graduate Studies).

[29] Pedro Sanchez-Cuevas, Guillermo Heredia, and Anibal Ollero, "Characterization of the Aerodynamic Ground Effect and Its Influence in Multirotor Control," International Journal of Aerospace Engineering, vol. 2017, Article ID 1823056, 17 pages, 2017. https://doi.org/10.1155/2017/1823056.

[30] Fondriest Environmental, Inc. "Conductivity, Salinity and Total Dissolved Solids." Fundamentals of Environmental Measurements. 3 Mar 2014. Web. < https://www.fondriest.com/environmental-measurements/parameters/water-quality/conductivity-salinity-tds/ >.

[31] Fondriest Environmental, Inc. "Measuring Turbidity, TSS, and Water Clarity." Fundamentals of Environmental Measurements. 5 Sep. 2014. Web. < https://www.fondriest.com/environmental-measurements/measurements/measuring-water-quality/turbidity-sensors-meters-and-methods/>.

[32] Turbidity Meter and Turbidity Sensor for Measurement, Testing and Analysis. Turbidity Testing,Water Meter,Digital,Water,Monitoring,Instrumentation,Sensors,Water,Quality,Management, Turbidimeter,Nephelometer,Nephelometric Turbidity Unit,Water Quality Testing,Probe,Turbidity,Water Sensor,Monitoring, www.globalw.com/products/turbidity.html.

[33] Fondriest Environmental, Inc. "Dissolved Oxygen." Fundamentals of Environmental Measurements. 19 Nov. 2013. Web. < https://www.fondriest.com/environmental-measurements/parameters/water-quality/dissolved-oxygen/ >.

[34] Fondriest Environmental, Inc. "Measuring Dissolved Oxygen." Fundamentals of Environmental Measurements. 7 Jan. 2014. `https://www.fondriest.com/environmental-measurements/measurements/measuring-water-quality/dissolved-oxygen-sensors-and-methods/.`

[35] "Aquatics." Recreation, recreation.rutgers.edu/facilities-5/accommodationsinclusions/adaptive-aquatics/.

[36] US Department of Commerce, and National Oceanic and Atmospheric Administration. "Estuaries." NOAA's National Ocean Service Education, 19 Dec. 2004, oceanservice.noaa.gov/education/kits/estuaries/estuaries01_whatis.html.

Chapter 6

Appendices

6.1 Appendix A - Thesis Overview

RUTGERS
THE STATE UNIVERSITY
OF NEW JERSEY

VIABILITY AND PERFORMANCE OF A MULTI-MEDIUM UNMANNED AERIAL VEHICLE DESIGNED FOR HYDRO DATA ACQUISITION

Johnny Serafini

Master of Science Candidate
May 2020

RUTGERS

Introduction – Water Quality Monitoring

Water quality management seeks to pursue processes that will enhance the chemical, physical, biological and radiological status of water bodies.

- Current methods are typically
  - Time consuming
  - Manual labor intensive
  - Expensive
  - Random

2

RUTGERS

Introduction – Relevant Related Work

Marques et al. have implemented the use of a marsupial robotic team consisting of an aerial and surface vehicle [21].

Aerial vehicle optimized for

- High altitude surveillance
- Rapid and large range sampling

Surface vehicle optimized for

- Endurance
- Close range sampling

3

RUTGERS

Introduction – Relevant Related Work

Rodriguez et al. have implemented a waterproof floating multirotor for water body monitoring.

Floating surface vehicle

- Reduces manual input
- Affordable alternative to expensive equipment
- Allows sampling in precarious locations

4

RUTGERS

Introduction – Objective

To design, validate and implement a formidable, easy to use platform for the acquisition of water data.

Multi-medium UAV

- Capable of Aerial data acquisition
- Capable of Surface navigation and data acquisition
- Capable of subsurface navigation and hydro data acquisition

RUTGERS

Introduction – Objective

With such a platform, salient hydro data could be quickly sampled over a test area at multiple depths.

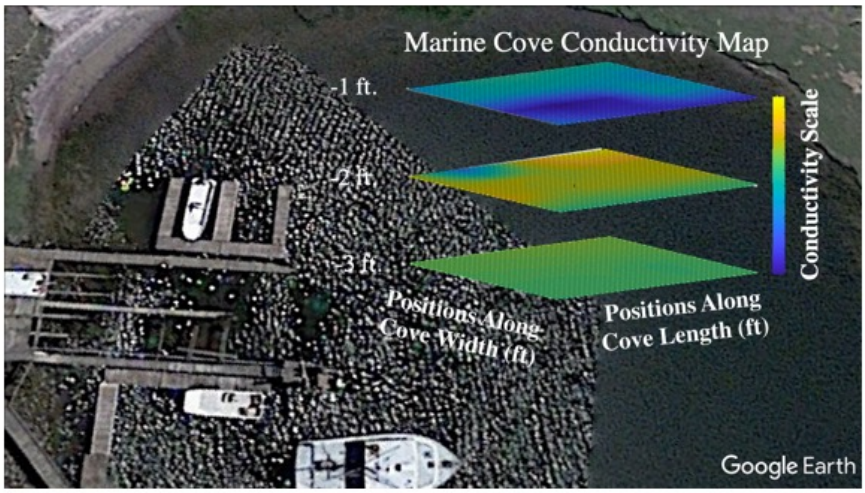

6

RUTGERS

Contents

- Naviator Version 7 Design
  - Power System
  - Performance
- Hardware Setup and Experimental Procedures
  - Scientific Sensors
  - Experimental Procedure
- Results
  - Conductivity
  - Dissolved Oxygen
- Conclusions
  - Accomplishments
  - Improvements

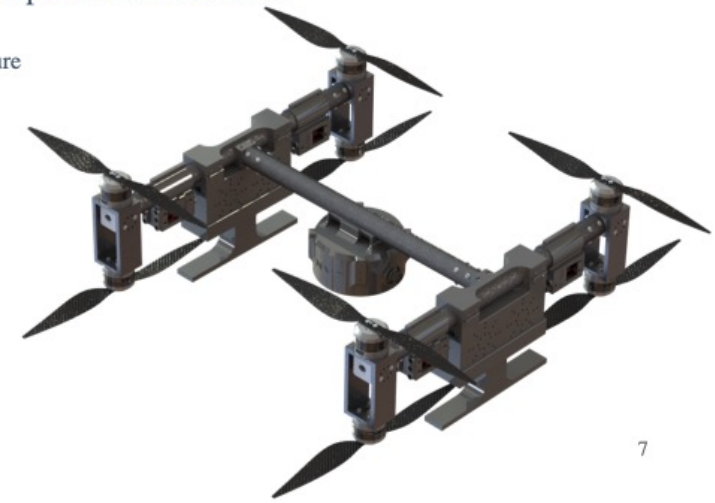

7

RUTGERS

Naviator V7 Design

Building upon the design concepts of the previous Naviator versions, the NV7 was tailored to the specific needs of the project.

Previous Versions:

- Expensive construction
- Complex design
- Non-replaceable battery

Naviator Version 7:

- Inexpensive construction
- Simple, repairable design
- Replaceable battery system

NV5

NV6

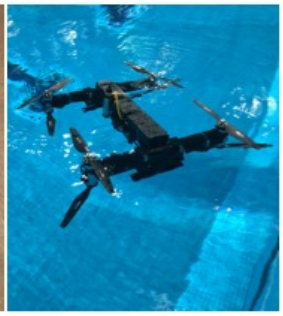

NV7

8

RUTGERS

Naviator V7 Design

The goal of the NV7 multi-rotor was to act as a formidable, easy to use platform for the acquisition of water data.

To reliably perform the NV7 design considered the following characteristics:

- Durable, lightweight frame (A)
- Modular components (B)
- Redundant safety measures (C)
- Inexpensive construction
- Simple battery replacement (D)
- Large payload capacity

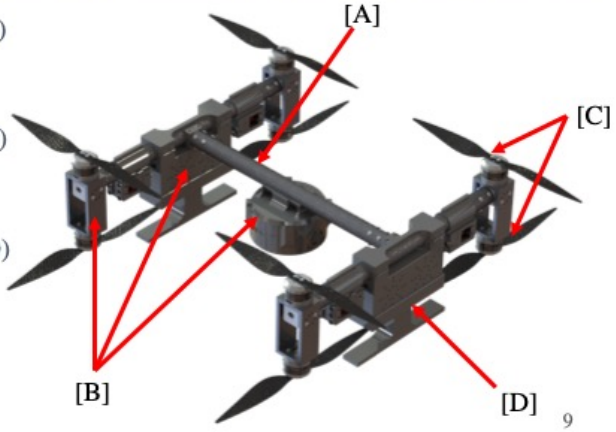

9

RUTGERS

Naviator V7 Power System Design

Crucial to the proper functionality of a multi-rotor is an adequate power system. A typical multi-rotor power system is composed of an energy source, ESCs and motors/propellers.

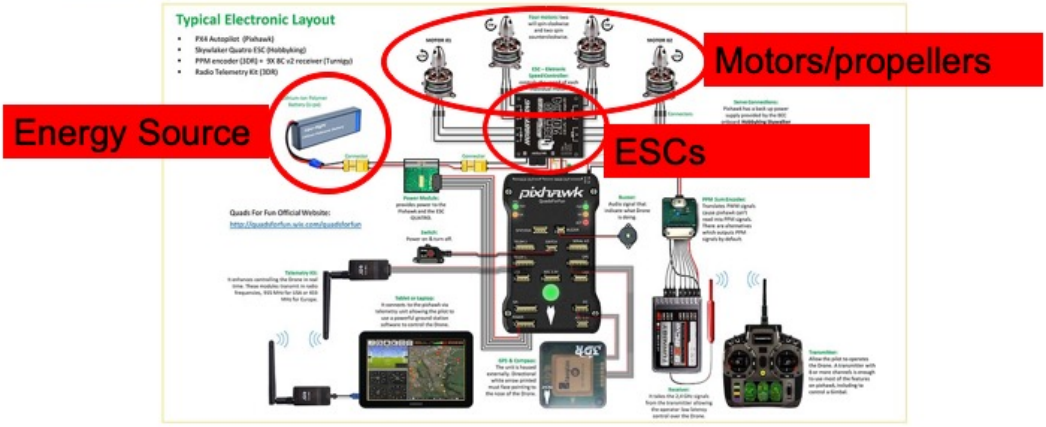

Intrinsically linked, each of these components must be chosen to properly complement each other for the proper optimization of multi-rotor control and performance.

RUTGERS

NV7 Power System Design: Endurance/Capacity

Vehicle endurance is a crucial characteristic for multi-rotor performance. Although endurance is affected by many parameters, the greatest factor is that of weight.

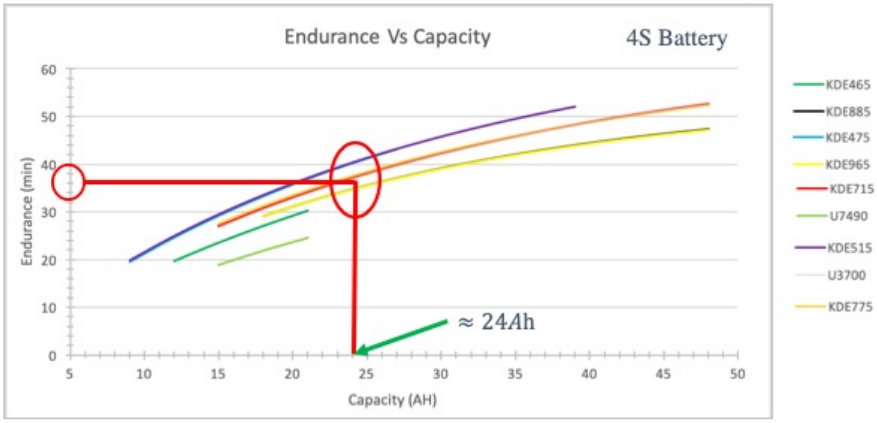

While increasing battery capacity increases weight, it also increases endurance. However, as one continues to increase capacity, endurance begins to wane. One must decide which capacity is sufficient for a given task.

RUTGERS

NV7 Power System Design: TTWR/Capacity

Thrust to weight ratio (TTWR) of a multirotor is the comparison of the full propulsion force to the vehicle weight. Increased TTWR corresponds to increased vehicle agility.

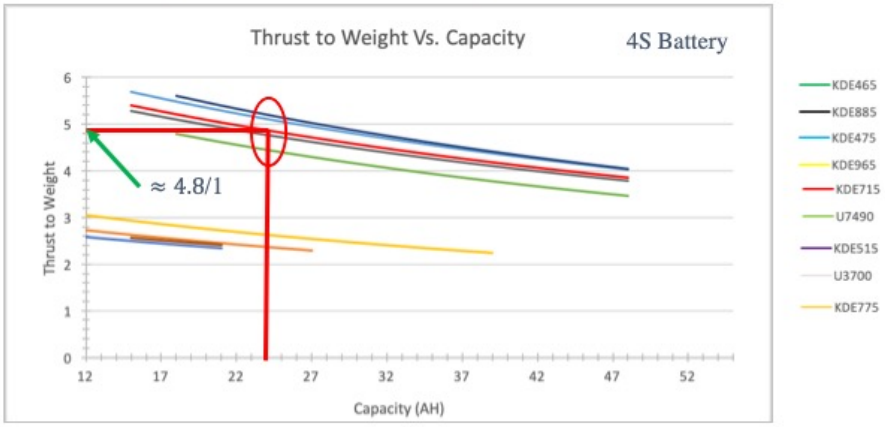

Generally regarded as an acceptable benchmark, a vehicle with a 2:1 TTWR is sufficient for stable operation. It was crucial for the NV7 to have a greater TTWR due to increased payload weights.

RUTGERS

NV7 Power System: Endurance & TTWR/Throttle

Method by which the optimal motor type was selected for the NV7. Hovering conditions with payload.

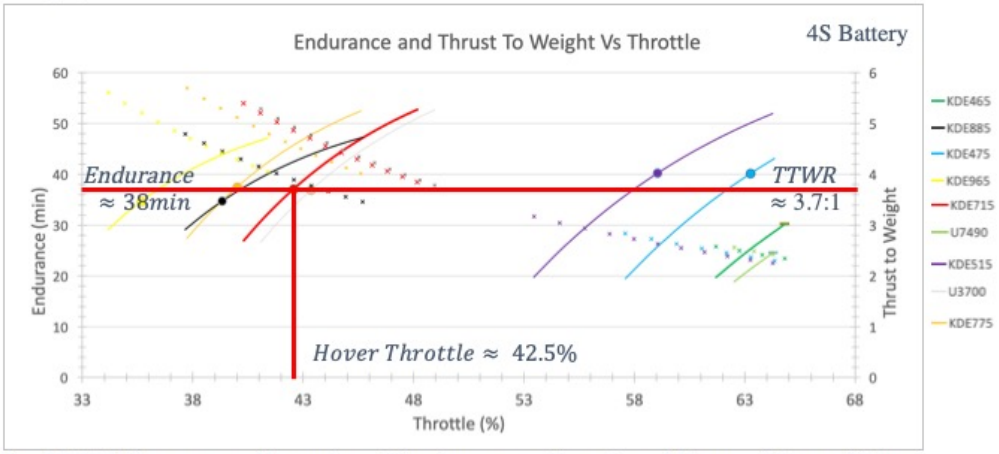

The KDE715 motor configuration offered greatest diversity while providing sufficient endurance, vehicle control and efficiency. Solid lines correspond to endurance. The scattered x's correspond to thrust to weight ratio. Solid circles correspond to 24Ah battery configuration.

RUTGERS

NV7 Atlas Scientific Sensor Specifications

The two sensors utilized for the following experiments were chosen for their lightweight construction and software compatibility.

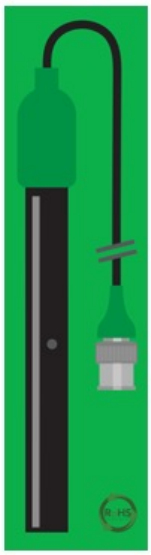

Conductivity:

- Units----$\mu Siemens$
- Range ----10uS/cm – 1S/cm
- Response---- 90%/1sec
- Max Press.---- 200psi (461ft)
- Temp. Rng.---- 1-110 ℃
- Weight ---- 51g

Dissolved Oxygen:

- Units----mg/L
- Range ----0 – 100 ml/L
- Response---- 0.03mg/L/sec
- Max Press.---- 500psi
- Temp. Rng.---- 1-50 ℃
- Weight ---- 52g

15

RUTGERS

NV7 Product Performance

The following plots demonstrate the performance of the water quality sensors both by hand held means and attached to the NV7.

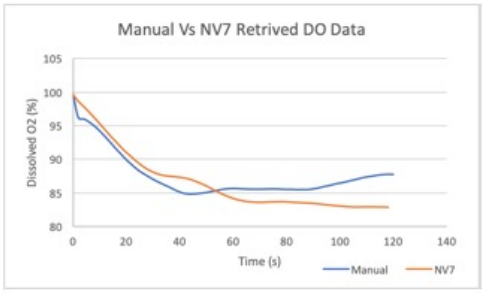

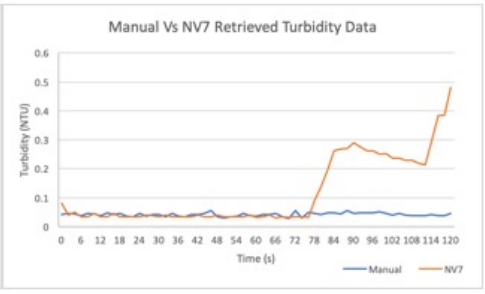

With repeated testing and as these plots demonstrate, both data retrieval methods correlate closely. The diverging sections may be accounted for by means of avoidable errors.

16

RUTGERS

Rutgers University Marine Field Station Test

Outdoor marine testing was conducted in the Jacques Cousteau Estuarine Research Reserve to demonstrate the NV7's capabilities of retrieving salient data.

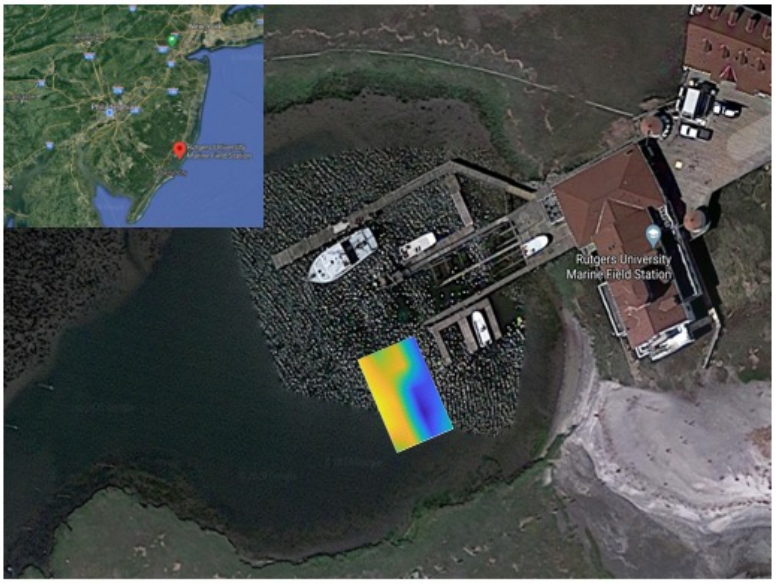

18

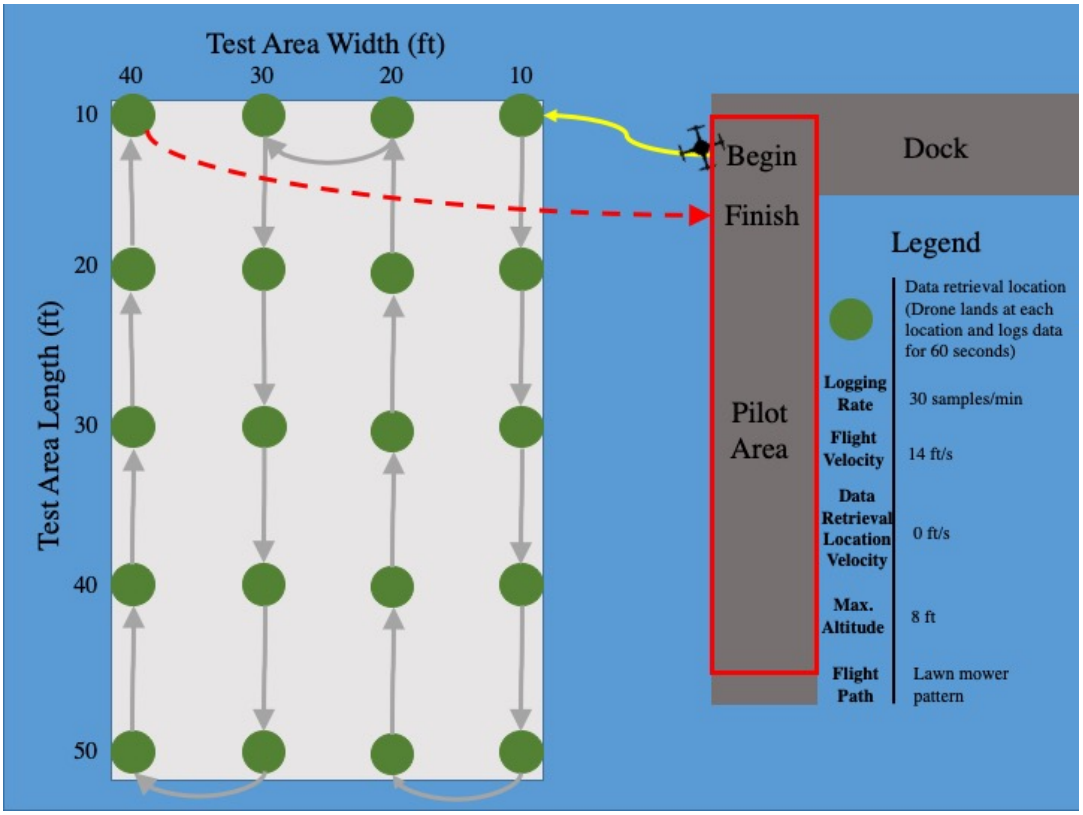

RUTGERS

Rutgers University Marine Field Station Test

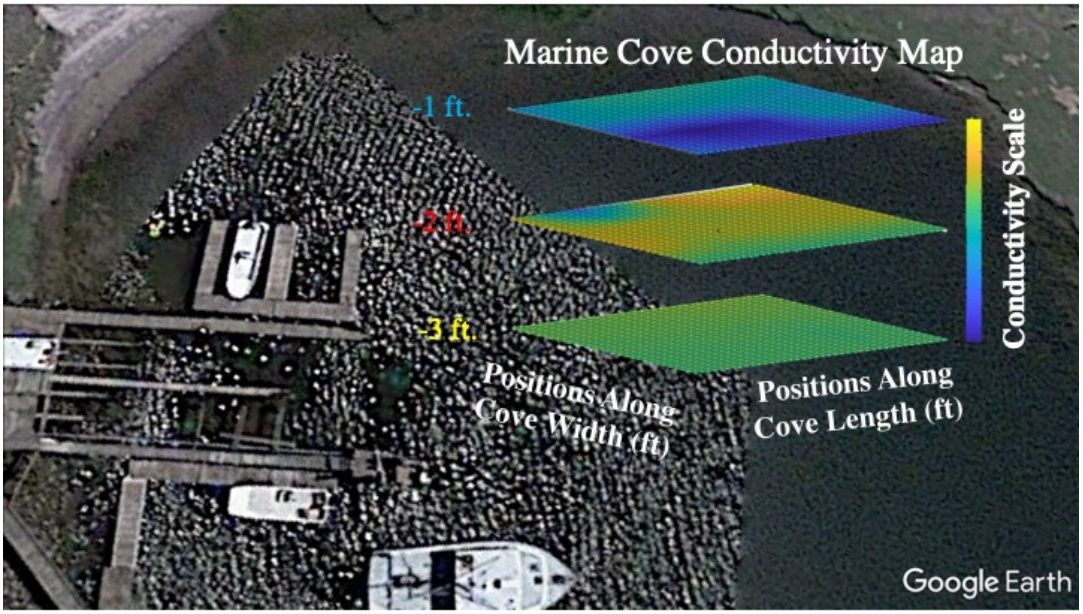

RUTGERS

RUMFS Cove Conductivity

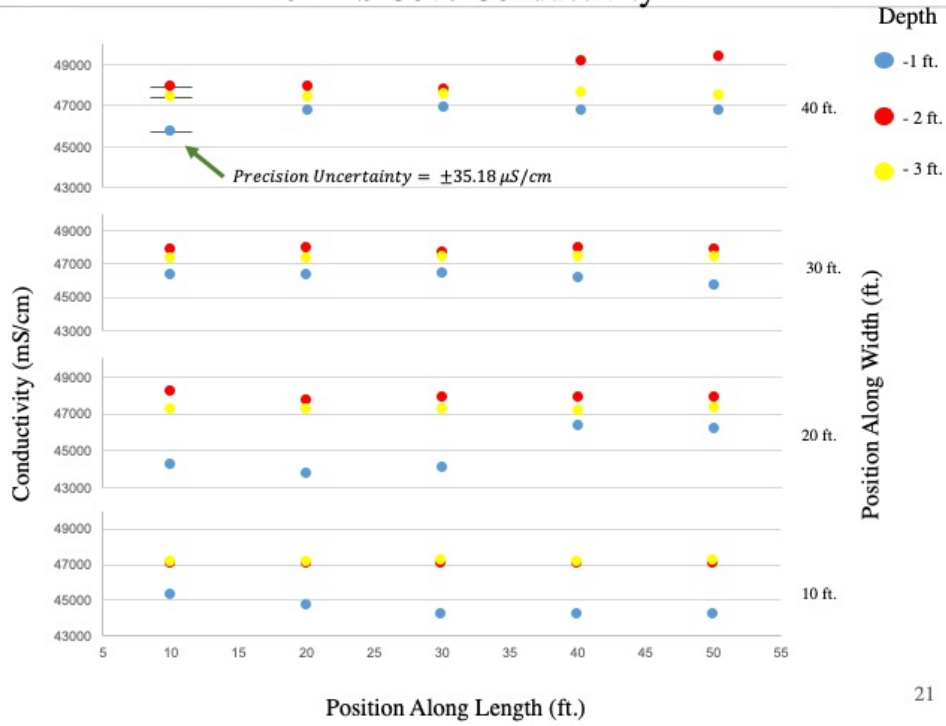

RUTGERS

RUMFS Cove Conductivity

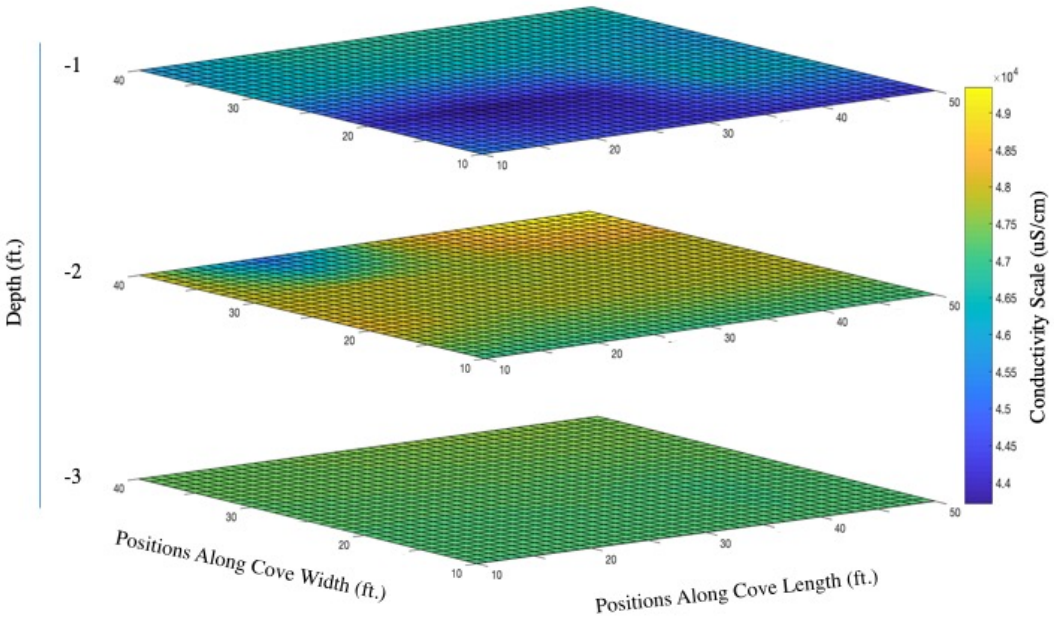

RUTGERS

RUMFS Cove Conductivity

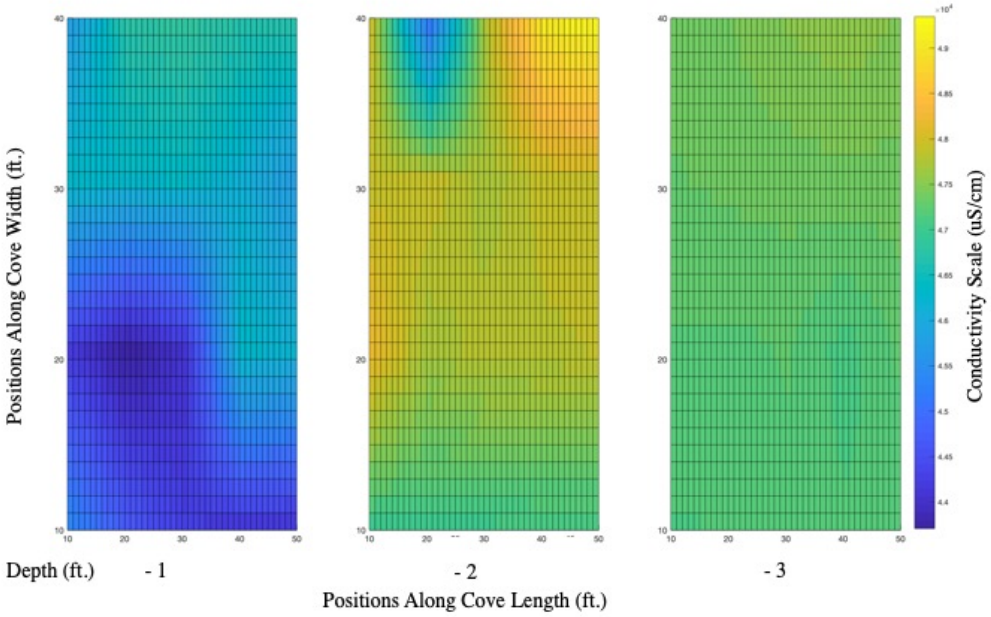

RUTGERS

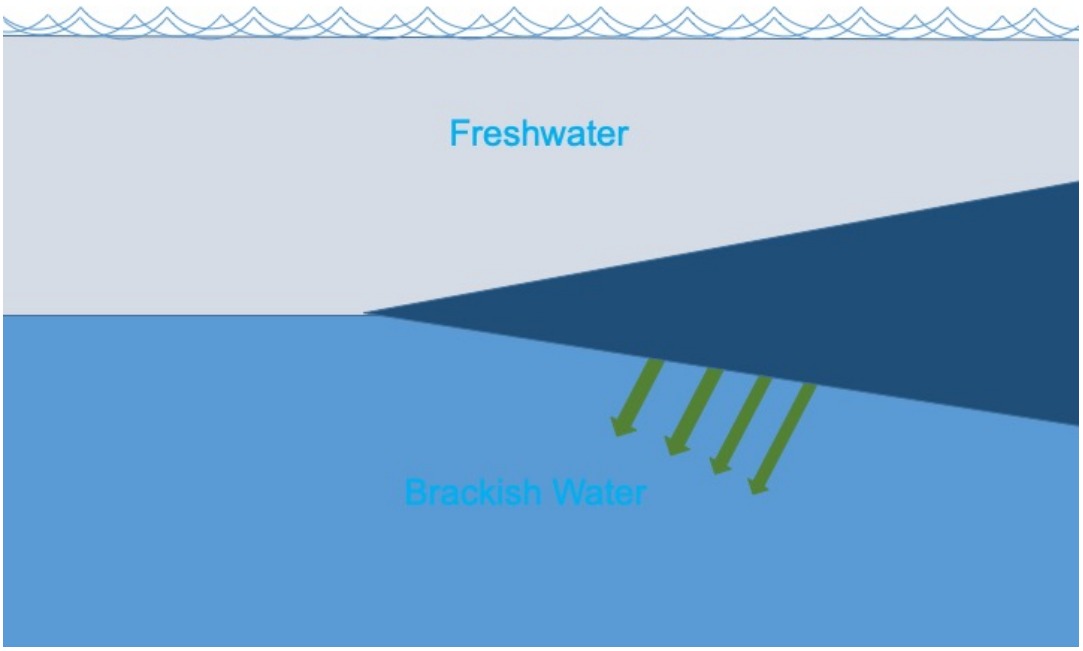

RUTGERS

RUMFS Cove Dissolved Oxygen Concentrations

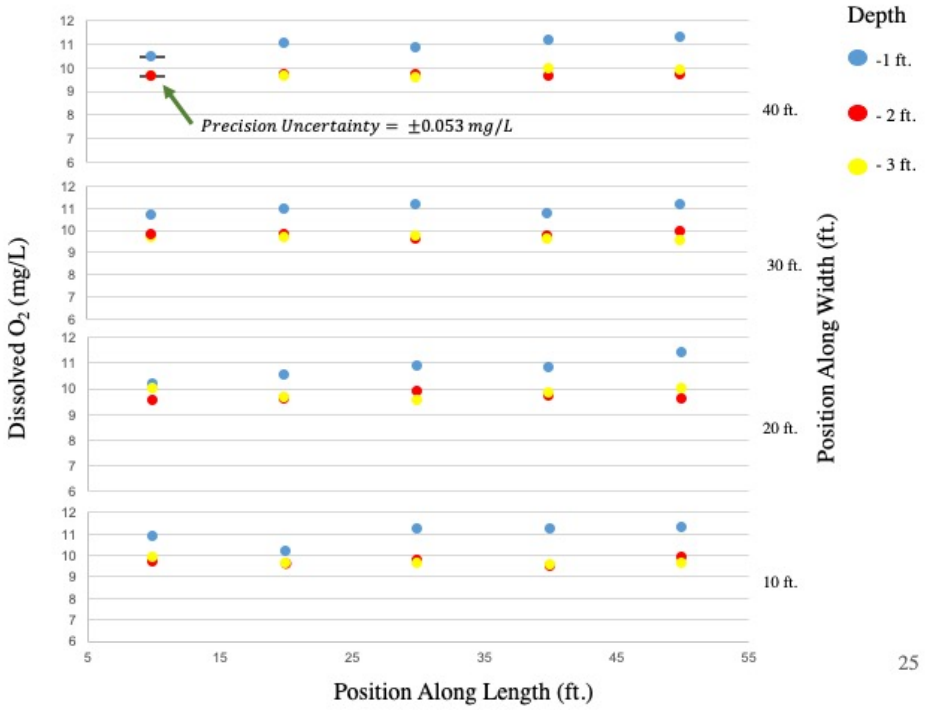

25

RUTGERS

RUMFS Cove Dissolved Oxygen Concentration

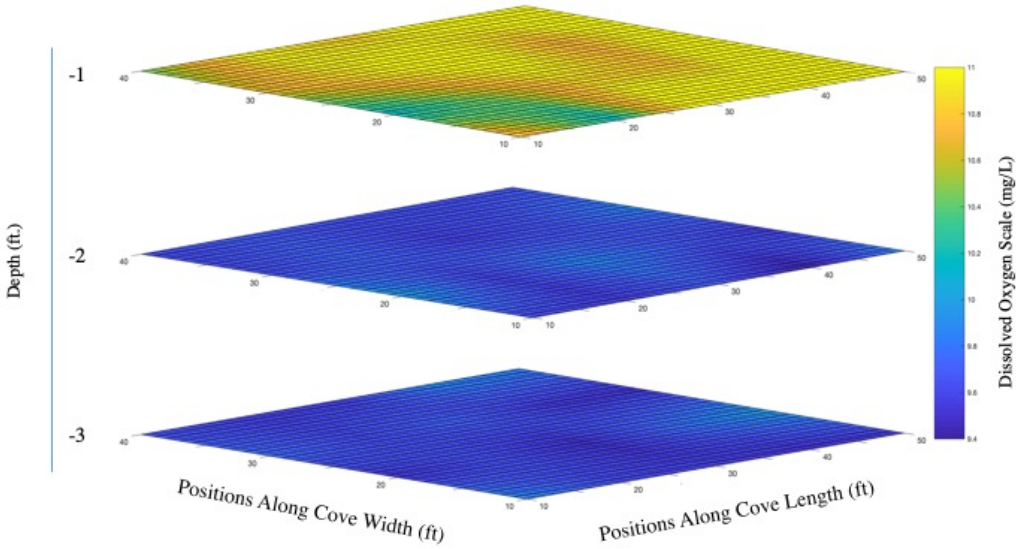

26

RUTGERS

RUMFS Cove Dissolved Oxygen Concentration

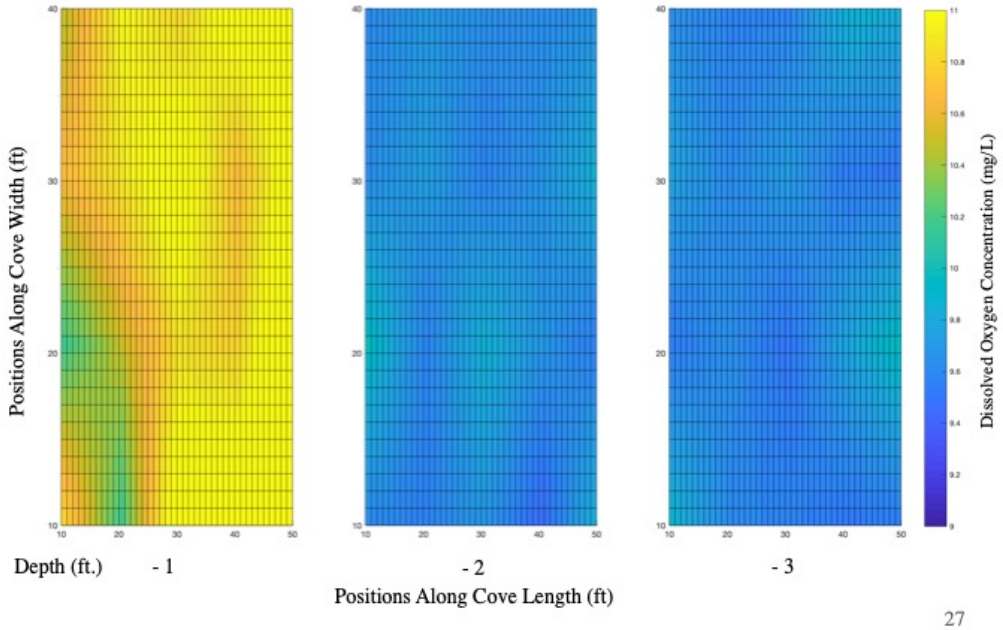

27

RUTGERS

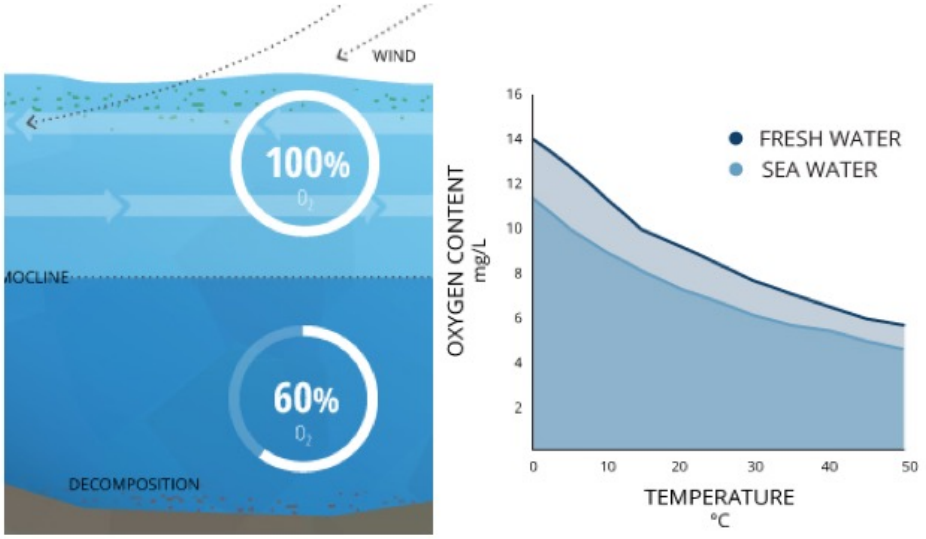

28

RUTGERS

Rutgers University Marine Field Station Test

- Full RUMFS cove conductivity mapping in the Jacques Cousteau Estuarine Research Reserve using the remote NV7 Platform.

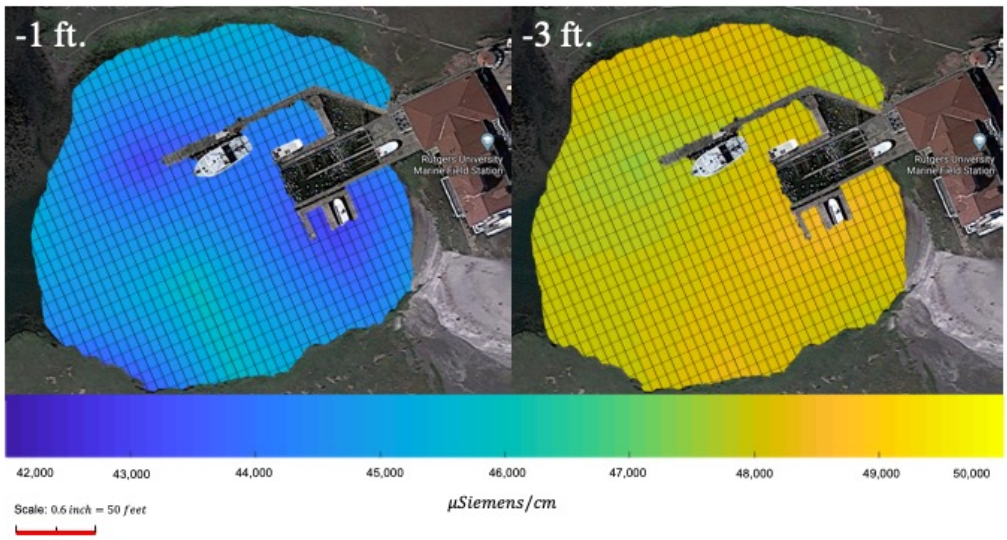

RUTGERS

Conclusions

Development and implementation of an unmanned, fully amphibious multi-rotor for the acquisition of hydro data.

- Accomplishments
  - Designed, constructed, tested, implemented a fully functional Naviator
  - Validated a method of using a multi-rotor for hydro data acquisition
  - Demonstrated capabilities and uses of a remote system for water quality monitoring
- Improvements
  - Autonomy
  - Sense and avoid systems
  - Improve modularity

Thank you! 30

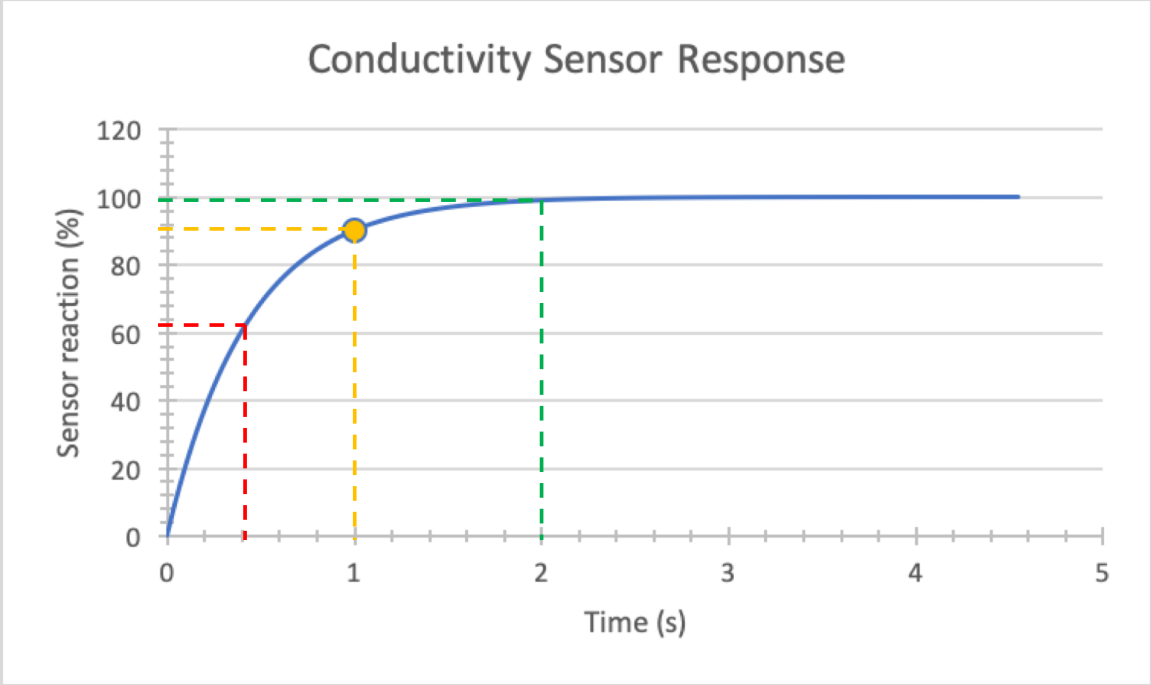

Figure 6.1: Atlas Scientific conductivity probe reaction time.